7-24-2012

Structural, Magnetic Properties and Mssbauer Analysis of R2Fe17-xTMx (R: Dy, Er & Gd, TM: Nb & Cr) Compounds.

Binod Kumar Rai

STRUCTURAL, MAGNETIC PROPERTIES AND MÖSSBAUER ANALYSIS OF $R_2FE_{17-X}TM_X$ (R: Dy, Er & Gd, TM: Nb & Cr) COMPOUNDS

by

Binod Kumar Rai

A Thesis

Submitted in Partial Fulfillment of the

Requirements for the Degree of

Master of Science

Major: Physics

The University of Memphis

August 2012

TO MY PARENTS

ABSTRACT

Rai, Binod Kumar. M.S. The University of Memphis. August/2012. Structural, Magnetic Properties and Mössbauer Analysis of $R_2Fe_{17-x}TM_x$ alloys. Major Professor: Sanjay R Mishra, PhD.

Binary rare-earth (R)-iron inter-metallic compounds with Th_2Ni_{17} and Th_2Zn_{17} structure have been extensively studied for their potential application as permanent magnets. The main drawbacks of these materials are low Curie temperature (T_c) and magnetic anisotropies. In the present study, substitution of Fe atom by Nb or Cr atom shows enhancement in the magnetic properties of R_2Fe_{17} compounds.

On the first part of the thesis, it presents effects of substituting iron atoms in R_2Fe_{17} (R: Dy and Er) with bigger non-magnetic Nb atoms and smaller magnetic Cr atoms with changes in the structural and magnetic properties of the $R_2Fe_{17-x}Nb$ (or Cr)$_x$ ($0 \leq x \leq 1.5$ for Nb and $0 \leq x \leq 3.0$ for Cr) compounds. The maximum T_c was observed at $x = 1$.

Other part of the thesis, ball milling on $Er_2Fe_{16}Nb_1$, $Dy_2Fe_{16}Nb_1$ and $Gd_2Fe_{16}Nb_1$ compounds shows enhancement in the magnetic properties and T_c due to exchange spring behavior.

ACKNOWLEDGEMENTS

It is my genuine pleasure to thank my thesis supervisor, Professor Sanjay R Mishra, for his guidance, support and constant encouragement throughout my thesis work. He taught me many novel ideas until I finished my work. I would like to thank again my supervisor and NSF for giving me opportunities to present my thesis work in many national and international conferences. I also would like to thank the physics department, IISO, graduate school for part of travel support and help. This project would not have been possible without the support of many other people. I would like to acknowledge my thesis committee members, Professor Muhammad Shah Jahan and Assistant Professor Lam Yu, who offered suggestions and support. Thanks to Prof. Kartik Ghosh and Mrs Soma Khanra who helped me to get low the temperature magnetic measurement.

I greatly appreciate the help of my friends from the University of Memphis who endured this long process with me, always offering support and love. Especial thanks to Sudhir Upreti for his generous support during the writing.

Finally, I owe a lot of thanks to my wife, Gyanu, for her support throughout all these years of my studying at the University of Memphis.

TABLE OF CONTENTS

List of Tables

List of Figures

1. Introduction

Permanent Magnets and their Classifications

Ferromagnetic material is a type of magnetic material that is highly attracted to magnets and can become permanently magnetized. Examples of ferromagnetic materials are iron, cobalt, nickel etc. Ferromagnetic materials are classified as soft ferromagnetic material and hard ferromagnetic material. Soft ferromagnetic materials are type of magnetic materials which have low coercivity (H_c) and can be easily magnetized or demagnetized by the influence of external magnetic field. But it has high saturation induction (B_s) and high saturation magnetization (M_s). With these properties, it can achieve high permeability (μ) which increases magnetic flux density. Hence soft ferromagnetic materials have been used in the devices in which low magnetic loss, low electric loss, high electrical resistivity are needed. For examples, it has been used in transformer, magnetic shielding, sensitive relays, fluxgate magnetometers etc. Hard ferromagnetic materials have high H_c, indicates resistance of these materials to becoming demagnetized. Having high induction remanence (B_r) and high M_s means that they have high energy product $(BH)_{max}$ which measures the storage and usable magnetic flux density. Hard magnetic materials are also called permanent magnetic materials. Permanent magnetic materials are widely used in the variety of the fields like electrochemical machines and devices, acoustic Transducers, mechanical force and torque applications, microwave/MM-Wave Devices, electron ion beam control, sensors, electric signal transducers, medical, electronics and bioengineering devices etc. [1]. Transportation alternatives such as electric cars, electricity generating technologies such as wind turbines, communications' technologies, such as iPhones, and even medical

equipment such as x-ray machines and MRI machines all require permanent magnet [2]. Research is still focused on trying to reduce the size of permanent magnets which makes them more efficient. In Fig. 1.1 shows that recent developed magnet (Nd-Fe-B) is very small in size compared to older magnet (Steel), but they are equal in efficiency and performance. Thus it gives the idea that how research has evolved towards better permanent magnet reducing the size of magnets. These magnets will, in turn, open new opportunities for novel designs.

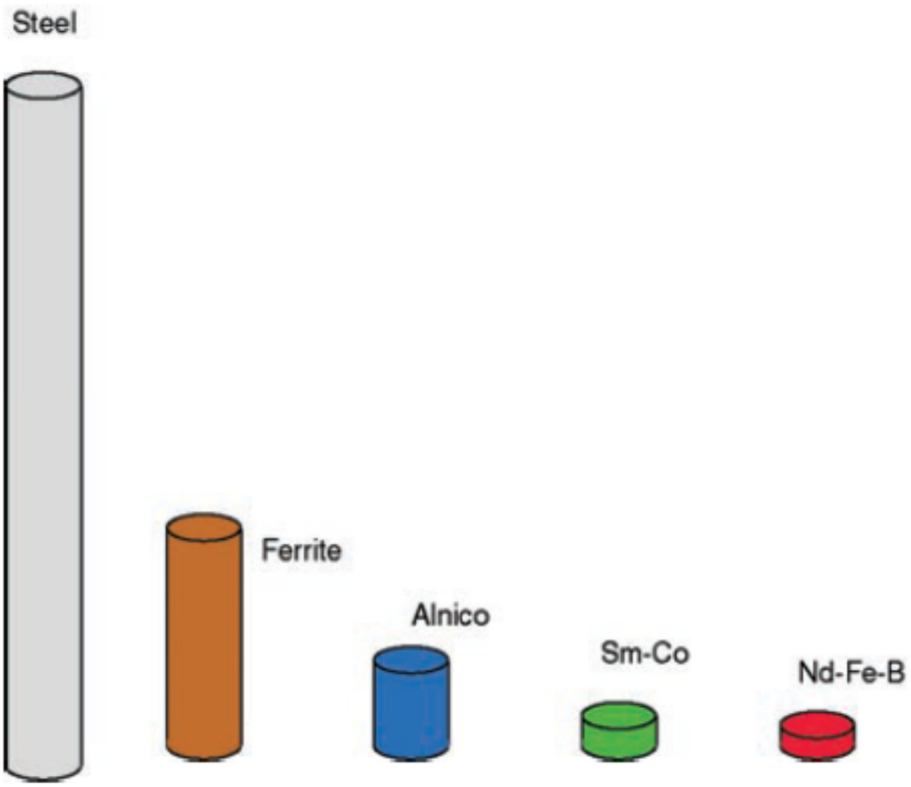

Figure 1.1: The reduction in the size of the permanent magnet over the year [3], each piece of the magnet stores same amount of the energy.

As per Magnetic Material Processing Association (MMPA), permanent magnets are classified in three groups; (i) Alnico magnet, (ii) Ceramic magnet, and (iii) Rare - Earth magnet.

Alnico Magnet

After naturally occurring loadstone (permanent magnet) and some steel alloy, Alnico (1930's) alloys discovered with basic constituent of aluminum, nickel, cobalt, copper, iron and titanium. Addition of silicon, zirconium, and niobium enhance heat treatment response in the Alnico alloy. Commercially available Alnico magnet has energy products around 9-10 MGOe. It has been using in all aspects of permanent magnet applications but especially using in many electrical uses [1].

Ceramic (Ferrite) Magnet

The general formula $MFe_{12}O_{19}$ describes the chemical composition of ferrite (ceramic) permanent magnets where M generally denotes Sr, Ba, & Pb. Hard magnetic ferrite has been available in 1950's with low material and processing costs as well as high coercivity. Commercially available hard ferrite magnet has energy product ~ 4.5 MGOe. It has been proved particularly suitable for light weight electric motor design, especially for DC motors [1].

Rare Earth (R) Magnet

Rare earth magnet or alloy made from rare earth (R) and 3d-transition metals (TM: Mn, Fe, Co, and Ni). As the electronic nature of the rare earth elements [4], 4f electrons are unpaired inner orbit electrons compared to 5d (nearly empty i. e. one electron or none) and 6s (completely full) orbit electrons. This unpaired 4f electrons are responsible for magnetic behavior of the rare earth elements. The magnetic moment is

based on the net angular momentum J, which is effect of total spin angular momenta S and orbital angular momenta L of the unpaired 4f electrons. This 4f shell is less than half full for lighter rare earth (like Pr) gives $|J| = (|L|-|S|)$ and more than half full for heavier rare earth (like Er) gives $|J| = (|L|+|S|)$. In general, the spins of R atoms are coupled antiparallel to the spins on the TM atoms. For lighter R, the 4f spin and orbital moments are opposed to one another, so J couple ferromagnetically to the TM moments. But for heavier rare earth, L and S are parallel to each other, so J couple antiparllel to TM moments, consequently results ferrimagnetic behavior for heavy rare earth compounds. Generally, rare earths have strong magnetic anisotropy which arises from partially filled 4f electron shell of Rare earth and TM has large magnetization. Hence, rare earth magnet is known as strongest permanent magnet than ferrite and alnico magnet.

Rare earth elements are using from many civilian to military technologies. They have become essential ingredient in applications such as face-centered catalysts for efficient oil production, florescent light bulbs, hybrid electric vehicles, nickel metal hydride batteries, computer hard drives, glass additives, polishing powders, direct-drive high power wind generators, speakers, nuclear fuels, radar, most weapons systems, and over a thousand other uses [5]. Fig. 1.2 shows that rare earth elements are relatively abundant as compared to other elements. It is name as rare earth in the sense of difficulty in the processing and mining these elements.

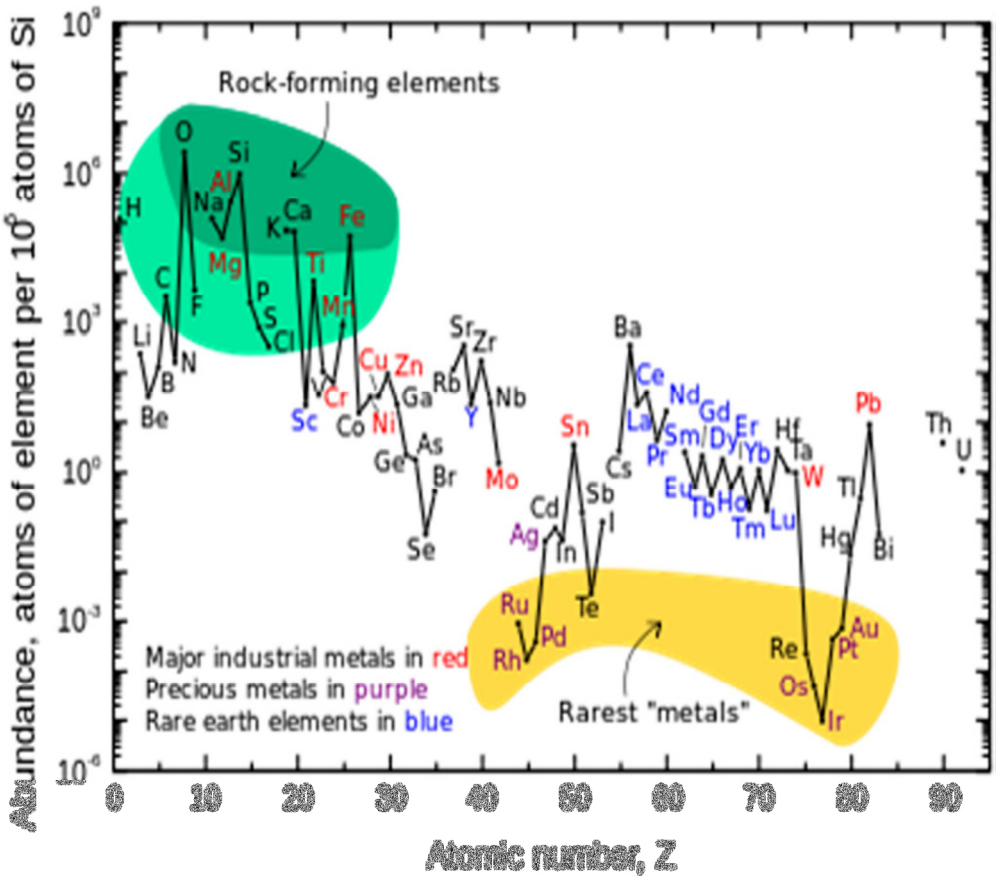

Figure 1.2: Relative abundance of elements worldwide [5].

Dysprosium is the rarest most expensive rare earth elements (Fig. 1.3) among all. It is because of large demands of it's in the permanent magnet applications and extensive use in neodymium iron boron magnet (R-Fe-B, best permanent magnet) as substituent which enhances the high temperature application of R-Fe-B magnet.

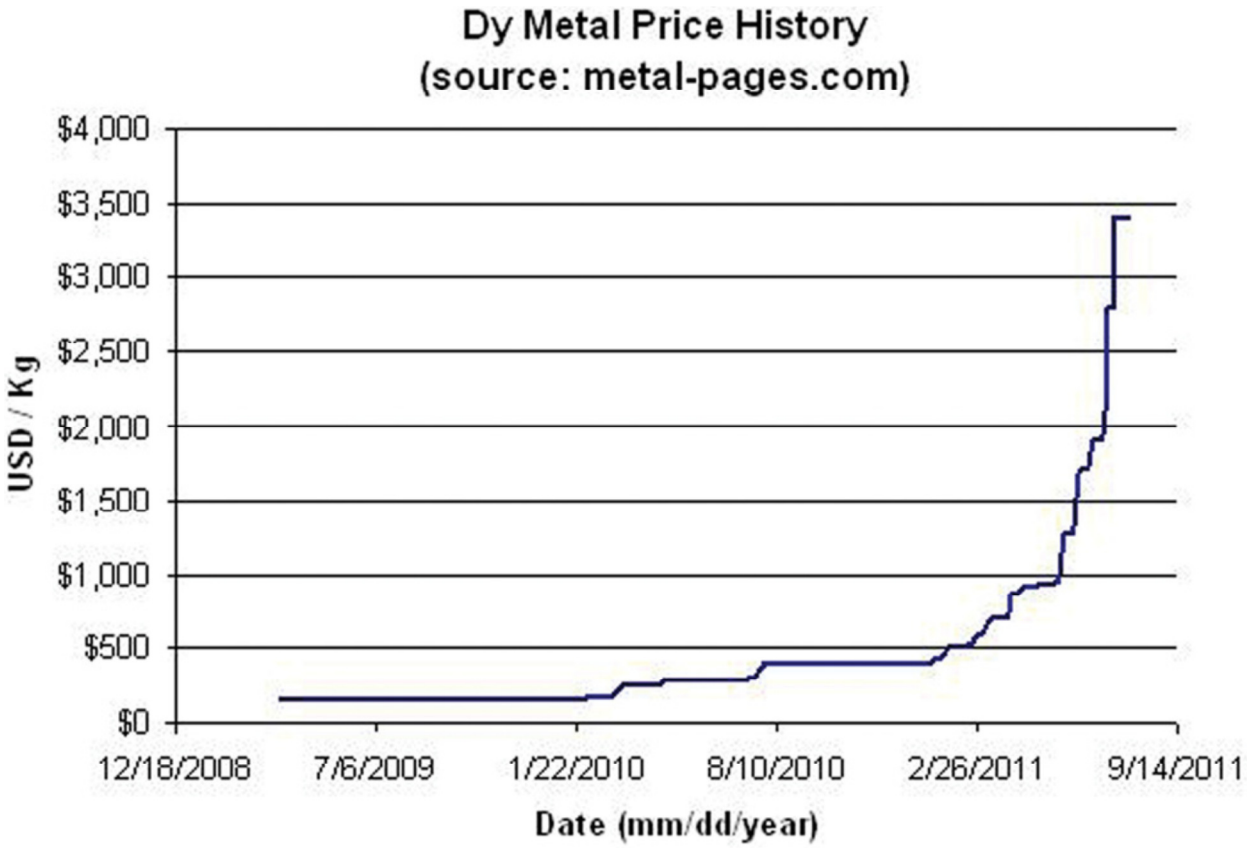

Figure 1.3: Dysprosium price history 2009 to 2011.

Most of the rare earth elements especially atomic numbers from 59-70, are ferromagnetic with high magnetic anisotropy, used for rare earth magnet. The rare earth magnets are further classified into three categories (a) RCo_5, (b) R_2TM_{17} (TM: transition metals like Fe, Co, Ni etc) and (3) $R_2TM_{14}B$ alloy. Each is greatly superior to previously known permanent magnets. The detail of rare earth magnet is given in the chapter "the trend in the permanent magnet improvement".

Hysteresis Loops and Magnetic properties

Ferromagnetic or permanent magnetic materials exhibit parallel alignment of moments that result in large net magnetization even in the absence of magnetic field. Spontaneous magnetization is the net magnetization that exists inside a uniformly

magnetized microscopic volume in zero applied magnetic fields. The magnitude of this magnetization at absolute zero is independent of the spin magnetic moments of electrons. On the other hand, saturation magnetization is the maximum induced magnetic moment that can be obtained in an external magnetic field. Beyond this field, magnetization of the material saturates. Though magnetization is independent of particle size, it depends on the temperature. Due to randomizing effects saturation magnetization becomes zero at a particular temperature called T_c [4]. T_c is critical temperature above which the long range alignment of the atomic dipoles due to exchange energy is totally destroyed and the material gets demagnetized. Therefore, it is desirable to have a higher T_c for the permanent magnetic materials.

When a magnetic field **H** is applied to ferromagnetic materials it develops a flux density B due to spin orientation of magnetic domains. The relation between induced **B** and applied **H** can be represented by the following equation:

$$\mathbf{B} = \mu_0(\mathbf{H} + \mathbf{M}) = \mu_0\mathbf{H} + \mathbf{J} \qquad \text{(SI)}$$

Where **M** is the magnetization, **J** is the polarization and μ_0 is the permeability of free space equal to $4\pi \times 10^{-7}$(Tm/A). The loop or graph between induced **B** (or **M**) and applied **H,** as shown below in the Fig. 1, called hysteresis loop.

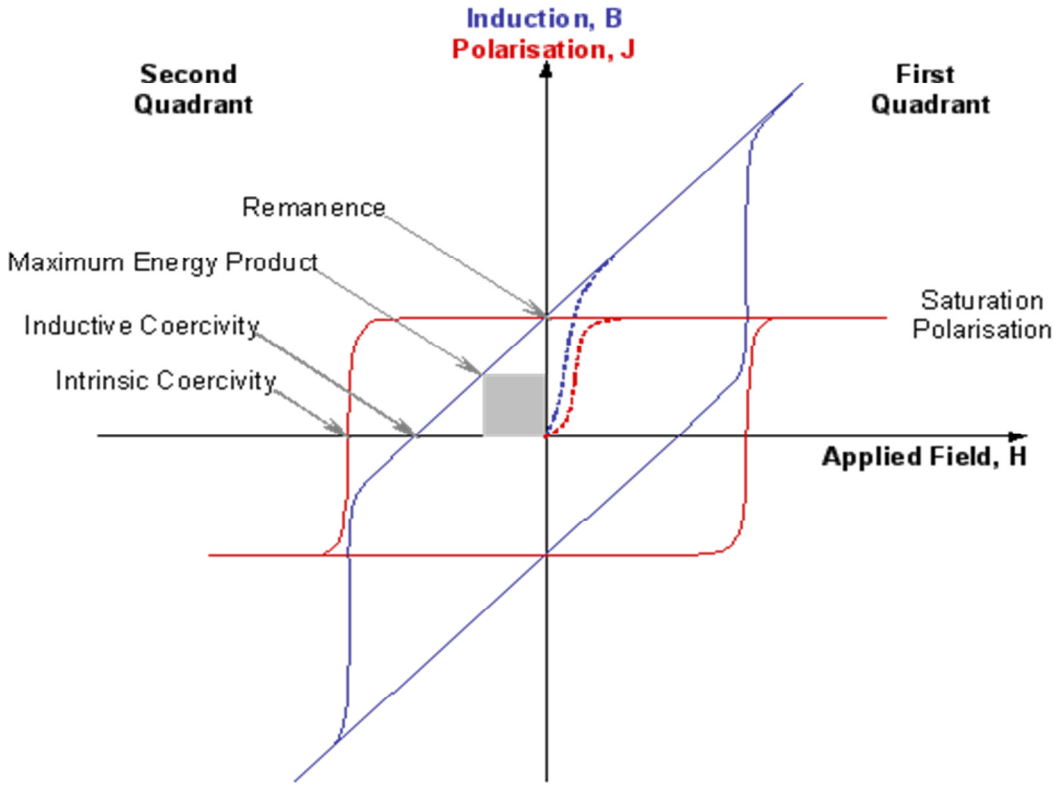

Figure 1.4: Hysteresis loop of ferromagnetic materials.

Generally, magnetic materials have two following properties; (i) Intrinsic magnetic properties and (ii) Extrinsic magnetic properties. Saturation magnetization (M_s), Curie temperature (T_c) and Magnetocrystalline anisotropy (M_A) are intrinsic properties of magnetic materials. These properties can understand or evaluate by magnetic moments and interactions in the atomic scale. On the other hand, remanence (M_r), coercivity (H_c) and maximum energy product $(BH)_{max}$ which arise from the actual microstructure are extrinsic properties of the magnet. The remanence (M_r) is defined as the magnetization or polarisation where the applied field is zero. X-axis value corresponding to zero magnetization or polarization in M-H curve (red loop or outer square loop in Fig. 1.4) and B-H curve (blue loop or inner rectangular loop in Fig. 1.4) are termed as intrinsic

coercivity (H_{ic}) and coercivity (H_c) respectively. The theoretical maximum energy product, the largest value, is an intrinsic quantity defined by

$$(BH)_{max} = \frac{1}{4}\mu_0 M_s^2 \qquad (1)$$

where M_s is the saturation magnetization. This can be achieved only if the magnet retains M_s in a reverse field at least as large as $\frac{1}{2}\mu_0 M_s$.

As the equation, the theoretical $(BH)_{max}$ is determined solely by the saturation magnetization, it can only be realized with enough coercivity. The highest possible coercivity for a particular material is confined by its anisotropy field (H_a). The anisotropy field is defined as necessary field to deflect the magnetic moment in a single crystal from the easy to the hard direction. The easy and hard directions arise from the interaction of the spin magnetic moment with the crystal lattice (spin-orbit coupling).

Trend in the permanent magnet improvement

In the history, Loadstone was reported as first permanent magnet. It is mainly composed of the ore magnetite (Fe_3O_4). Although, magnetite has high ordering temperature (T_c) and large M_A, it has fairly low magnetic moment. In the search of high magnetization materials, the first artificial permanent magnet of different steels discovered at the end of last century and beginning of this century. These materials were based on iron. As the equation (1), the theoretical maximum energy product, $BH_{max} = \frac{1}{4}\mu_0 M_s^2 \approx 115$ MGOe where $4\pi M_s = B_r = 21.5$ kG for iron. This gigantic value can only be realized with enough coercivity or anisotropy field. But for iron anisotropy field H_A is 500 Oe which hinders to achieve the theoretical energy product. Since then the larger

magnetic anisotropy or high coercivity magnetic material became main consideration in the search of new class permanent magnetic materials. In 1932, the alnico magnets were developed [6] with coercivity ~ 2 kOe. This kind of materials had reported about 13 MGOe energy product [7]. The achieved coercivity is still low because it comprises from shape anisotropy. Shape anisotropy is the preferential alignment of atomic moments in a given direction due to the shape of the magnetic particle. Coercivity contributed from M_A has higher value than coericivity attributed from shape anisotropy. The hexagonal ferrite is the first group of the ferrite whose coercivities is attributed due to M_A. The hard ferrite based on the hexagonal oxide $SrAl_4Fe_8O_{19}$ has reported substantially large coercivity (18 kOe) [8]. However, this kind of material has very low remnant flux density (B_r). This low B_r abruptly decreases $(BH)_{max}$ of the permanent magnet.

To account for all above limitations, since 1966 a new class of permanent magnet materials developed, called ferromagnetic intermetallic compounds. It is compounds of 3d-transition iron or cobalt metals with the rare-earth (R) elements. It is also called rare-earth permanent magnet (RPM). Here transition metals contribute for high magnetization and rare-earth element capable for imposing required high uniaxial crystal anisotropy in these compounds. Consequently, RPM stands out with magnetic properties 100 times better than those magnets known before 1930. Such outstanding properties of RPM, it has been using broadly in many modern technology (like hybrid electric car, wind turbine, MRI, motors) and is also displacing more conventional magnet type in many cases.

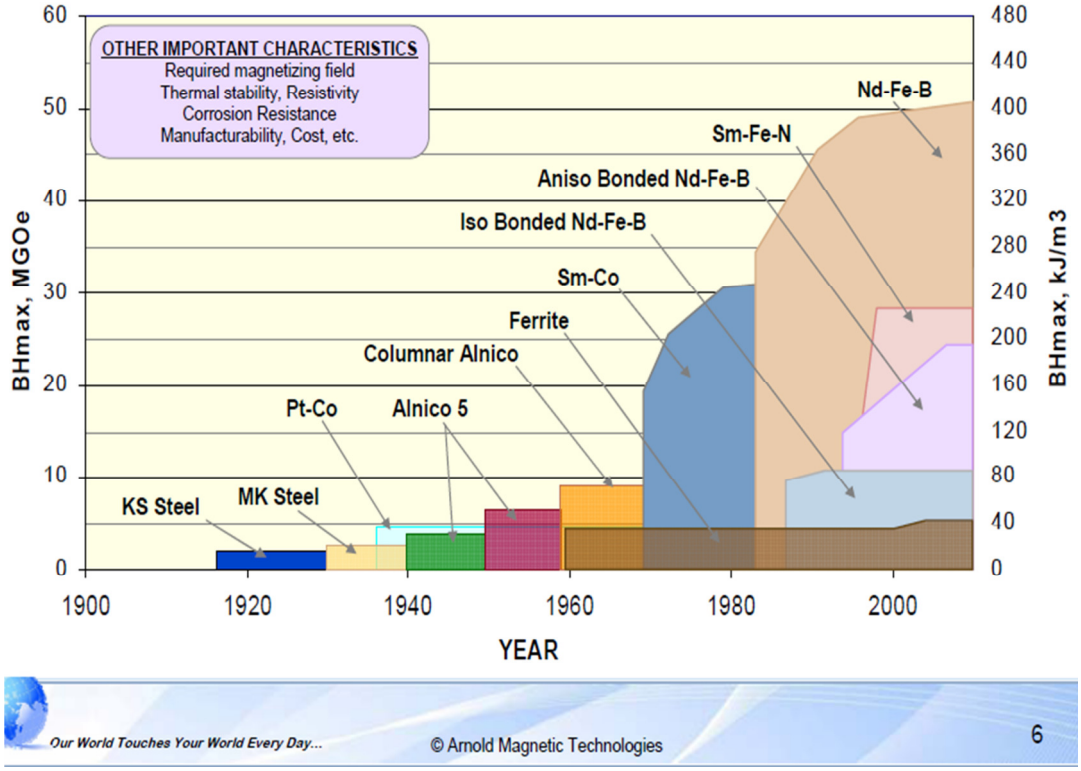

Figure 1.5: Improvement on the strength of magnet over the years.

Most of the rare earth elements which are ferromagnetic with high magnetic anisotropy value but low T_c (around room temperature). Improvement in the T_c of these rare earth elements has been observed in its many intermetallic compounds with transition metals such as Fe, Co, Ni etc. These alloys nowadays also known as permanent magnetic materials dates from 1966, When K. J. Strnat and G. Hoffer of the U.S. Air Force Materials Laboratory reported that YCo_5 has an anisotropy constant of 5.5 x 10^7 ergs/cm^3 or 5.5 x 10^6 J/m^3 [9]. Since then, different combination of rare earth/transition metal compounds have been studied in order to understand their crystal structures, M_s, M_A, T_c etc. To have better permanent magnet material, materials should have high and positive uniaxial anisotropy, easy axis of magnetization rather than easy

plane, fairly high T_c (well above room temperature) and high M_s. Low cost, good mechanical properties, good resistance to corrosion are also desirable.

Modern strongest permanent magnets are intermetallic compounds of a rare-earth (R) and transition metals like iron and cobalt. R element provides high M_A whereas the TM provides high magnetic moment and high ordering temperature. When the rare-earth 4f magnetic sublattice is magnetically coupled to transition metal (Fe or Co) 3d magnetic sublattice, gives unique properties on the compounds so it is strongest. This coupling is attributed from 4f-3d exchange interaction in intermetallic compounds. It was reported that 5d electrons of R component plays important role in the R-TM coupling or enhancement of 3d-5d hybridization increases $|J_{RTM}|$. $|J_{RTM}|$ depends on various factors like the transition metal concentration, the nature of the rare earth component, nature of the 3d component, and the interstitial atoms [10]. According to Liu et al [10], $|J_{RTM}|$ decreases as the transition metal concentration increases or increasing atomic number of R component or nature of the 3d component (TM = Fe, Co, Ni in the sequence) or adding interstitial atoms in the rare-earth transition metal alloys. The reasons for decrease $|J_{RTM}|$ values because in all of these cases 3d-5d hybridization decreases with these parameters. Improving 3d-5d hybridization, it increases the R-TM coupling. The research on R and TM compounds began in 1970's, as a result of the intensive research on the new permanent magnets composed of R and 3d TM, the first compounds being studied were the RTM_2 laves phases (R: Er, Tb, Ho, Y and TM: Fe, Co, Ni) [11]. The RT_2 compounds are ferromagnetic (with nonmagnetic or light R elements) or ferrimagnetic (with heavy R elements). The easy axes of RTM_2 phases are [111] or [100] directions. Besides lave

phases, R elements and TM can form kinds of intermetallics compounds like RCo_2, R_3Co, RCo_3, RCo_5, R_2Co_7, R_2Co_{17}, R_2Fe_{17} phases.

Most extensively studied useful permanent magnet materials are $SmCo_5$, Sm_2Fe_{17} and $Nd_2Fe_{14}B$, each is greatly superior than previously known permanent magnets. $SmCo_5$ alloy has a hexagonal crystal structure with the easy axis along the c-axis of the unit cell, and high anisotropy constant 7.7 x 10^7 ergs/cm^3 or 7.7 x 10^6 J/m^3 (5.5 x 10^7 ergs/cm^3 for YCo_5). The high coercive field required to magnetize initially Sm_2Fe_{17} alloy, effect called domain wall pinning whereas $SmCo_5$ alloy can be magnetized initially by a field much smaller than their intrinsic coercive field, H_{ci}, called domain nucleation. Continuous efforts to find better and cheaper permanent magnet materials introduce $Nd_2Fe_{14}B$ permanent magnet which has tetragonal crystal with strong uniaxial anisotropy and a T_c slightly above 300 K. $Nd_2Fe_{14}B$ is cheaper because Fe is cheaper than Co and Nd is cheaper than Sm, and also $Nd_2Fe_{14}B$ contains relatively little rare earth. The main disadvantage of Sm-Co permanent magnet is extremely expensive whereas the main disadvantages of NdFeB are relatively low T_c ~ 300 K, and severe corrosion in moist atmospheres.

R_2Fe_{17} compound

The R_2Fe_{17} compound is the most iron-rich phase in the binary R-Fe alloy system and consequently has the highest magnetization. This intermetallics with rare earths lighter than Gd crystallize in the rhombohedral structure (space group $R\bar{3}$ m) with 3 molecules in the unit cell. On the other hand, R heavier than Tb crystallize in the hexagonal structure (space group P 6_3/mmc) which have 2 molecules in the unit cell. There are four iron sites in the unit cells of rhombohedral and hexagonal structures. R

atoms occupy one site in the rhombohedral structure, whereas, two crystallographically inequivalent sites occupy (2b and 2d as shown in Fig. 1.6.a) in the hexagonal structure [12].

The crystal structures of R_2Fe_{17} are strongly related to the $CaCu_5$ type. The R_2Fe_{17} can be generated from the $CaCu_5$ structural units by replacement of one R atom with two 3d atoms ($3RFe_5$-R+2Fe = R_2Fe_{17}). The structural block of R_2Fe_{17} has about the same dimension along c axis as that of the 1:5 lattice, whereas the unit cell should have 3 times larger area in the basal plane than in the 1:5 lattice. As a result, the lattice is almost doubled. The double layer stacking of these structural blocks corresponds to the hexagonal structure modification, i.e. the Th_2Ni_{17} type (P63/mmc) and the unit cell contains two formula units (Figure 6.a). This structure is observed for the heavy R and Y. In the case of light R, a three-layer stacking leads to the rhombohedra structure modification, i.e. to the Th_2Zn_{17} type (R-3m) and each unit cell contains three formula units (Fig. 1.6.b). In the R_2Fe_{17} compounds, four crystallographically non-equivalent iron sites are present. According to Wyckoff's notation they are indicated by *c*(*f*), *d*(*g*), *h*(*j*), and *f*(*k*) where the symbols written in the brackets for hexagonal structure and others for rhombohedral [13].

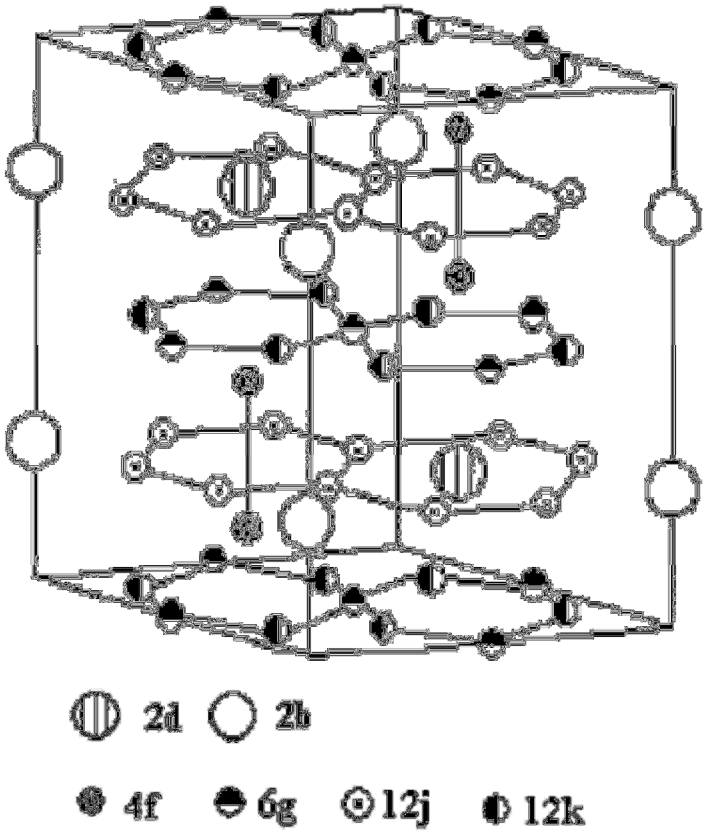

Figure 1.6a: Hexagonal Th_2N_{i17} structure

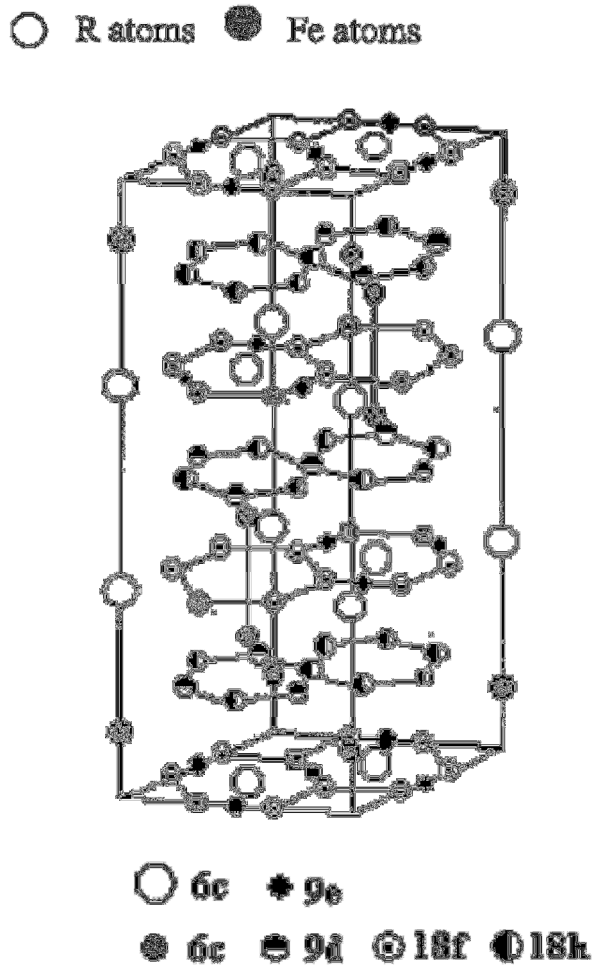

Figure 1.6b: Rhombohedral Th_2Zn_{17} structure.

The R_2Fe_{17} compound is the most iron-rich phase in the binary R-Fe alloy system and consequently has the highest magnetization. Unfortunately its T_c is typically low (around RT) and its easy magnetization direction lies in the basal plane of the hexagonal unit cell which is unfavorable for permanent magnets. In R-TM intermetallic compounds, two types (one for R and another for TM) of magnetic moment exist. It gives three types of spin pairs in R-TM compound that comprises three different exchange interactions, J, viz. TM-TM, R-TM and R-R interactions which are responsible for magnetic ordering

and hence set up T_c. When the TM atoms like Co carry well stabilized magnetic moment, the TM-TM interactions dominates. In these R-TM intermetallic compounds, T_c is mainly determined by the TM-magnetic sublattice. For example, in $SmCo_5$ compound, Co-Co interactions are strongly ferromagnetic giving rise to T_c ~ 1000 K as in pure Co (T_c ~ 1393 K) [14]. But Fe magnetism is completely different than Co, it is strongly dependent on Fe-Fe distances. Since it strongly depends on Fe-Fe distance, it might have negative exchange interaction if Fe-Fe distance is shorter than pure Fe. Hence it lowers T_c of the $R_2Fe_{17} \approx 300$ K (see table 1) as compared to T_c of pure Fe ≈ 1043 K. The drop in T_c is because of reduction in 3d-3d interaction in Fe-rich compounds, R_2Fe_{17}. Despite TM-TM strong interaction, there is R-R interaction which is very weak and indirect since it proceeds via 4f-5d-5d-4f mechanism [14]. The effectiveness of R-R interaction further dilute as R substituted by TM compounds. Besides very strong TM-TM interaction and very weak R-R interaction, intermediate R-TM interaction exists in the R-TM intermetallic compounds. As discussed above about rare earths, besides the partially filled 4f electron shell, it also has nearly empty 5d electron shell which plays a crucial role in the interaction via 4f-5d-3d mechanism. This mechanism was first observed by Campbell [15]. The strong direct exchange interaction between nearly empty 5d (R) and nearly filled 3d (TM) transmitted via 4f levels via the intra-atomic 4f-5d exchange. This causes ferro or ferri-magnetic alignment of R-TM intermetallic compounds depending upon light or heavy rare earth respectively.

Exchange-Spring Magnets

It was proposed in 1991 by E. Kneller and R. Hawig [16] that if the soft magnetic (high magnetization and low coercivity like Fe ,Co, FeNi, FeCo etc) layers are thin enough around the fine particles of permanent magnet (high Coercivity). It hinders the formation of domain walls, this composite end up with high coercivity and high magnetization that results high energy product. The higher energy product better the permanent magnet is. This kind of magnet is called exchange-spring magnet [17]. Exchange-spring magnets have been prepared by rapid-quenching, subsequent ball milling and alloying.

Ball Milling

A ball mill, is an instrument, can be used for grinding and mixing various materials. The resulting product would be extremely fine powder and nano-materials with metastable structure. High energy ball milling was first developed in the late 1960's by Benjamin and coworkers [18] to produce complex oxide dispersion strengthened alloys for high temperature structural applications.

The potential of high energy ball milling method in material processing has been explored extensively after discovery of amorphous alloys could be made by mechanical alloying [19]. Besides the uniform dispersions of oxide particles and amorphization, many other effects have been presented for examples grain refinement [20], crystallization of amorphous alloys [21-23], disordering [24,25], nanocomposite mixing [26, 27], extended solubility [28].

A high Energy ball milling apparatus consist of a cylindrical, called vial, placed in rotating or vibrating frame. Ball milling operates by moving hardened balls energetically

inside a rotating or vibrating container. As the hardened balls move energetically, the collisions occur between balls or ball and wall transfer the mechanical energy to the powder material trapped in between. Per conservation of energy, part of transferred energy caused crystalline defects and atomic disorder whereas the rest energy dissipated as heat. It causes the HEBM hot at the end of the milling.

As the powder materials come in between balls or ball and wall, the deformation, fracture and coalescence occurs in the atomic level. The crystalline alloys after ball milling have a lot of defects like new surfaces, dislocations, vacancies, grain boundaries, chemical disorder, staking fault. These different forms of defects contribute raising free energy in the crystalline alloys. Once the free energy which is stored in the alloys exceeds the amorphous state, the amorphization of the alloys occur. The presence of defects and microstructural refinement in the alloys enhance the diffusivity and hence leads to grain refinement of the alloys. In addition, annealing the mechanical alloy at elevated temperature is necessary if the formation of intermetallics is desired [29]. Ball milling is the process of alloying of different powders. However, in the past, the ball milling of a single phase powder has also shown interesting results like [30-33].

2. Literature Review

Generally, R-TM permanent magnets have high H_A, M_s, and T_c. Typical, R_2Fe_{17} compounds found very low T_c and magnetic anisotropies. Fig. 2.1 shows change in T_c for different R based permanent magnet. It is seen that R_2Fe_{17} have lowest T_c, in comparision of other R-TM phases. Thus there is a considerable challenge in improving T_c of R_2Fe_{17}. Various efforts have been made to improve both T_c and H_A of R_2Fe_{17} compounds based on substitution of metals, non-metals, and interstitial atoms.

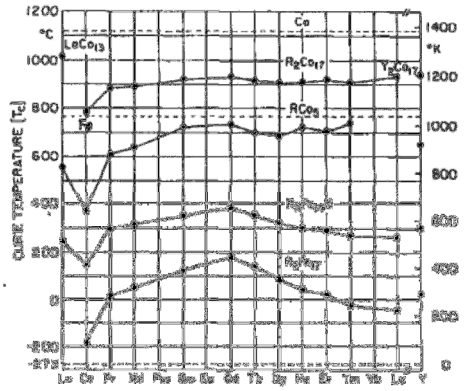

Figure 2.1: Curie temperature for different series of R-TM intermetallic compounds [34].

Previous research work had reported that significant improvement in the T_c of R_2Fe_{17} with the substitution of smaller or bigger atoms for Fe atoms, see Table 1 [35-42] or by introducing carbides and nitrides into it. The R carbides ($R_2Fe_{17}C_x$) and nitrides ($R_2Fe_{17}N_x$) are interstitial solutions in R_2Fe_{17} [43-45]. In 1991, J. M. D. Coey and H. Sun [43] reported that nitrogen can be added to Sm_2Co_{17}, causing an expansion of the lattice, an improvement in magnetization, anisotropy and T_c. These are important factors to be better permanent magnet. However, these nitride and carbide materials are not stable at conventional sintering temperatures. Some examples of stable nitride and carbide magnets are $Sm_2Fe_{17}N_3$, $Er_2Fe_{17}C_1$. The improvement in the magnetic properties is arising from the decrease of negative exchange-interaction due to distortion of the unit cell volume caused by substitution or addition. The Table 1 shows substituting smaller (Cr or Mn) or bigger magnetic (Co or Ni) or non-magnetic elements (Al, Ga, Si) for iron-

Table 1: Curie temperature, T_c, of various R_2Fe_{17} and its substituted alloy.

R_2Fe_{17} compounds	T_c (K)	R_2Fe_{17} compounds	T_c (K)
Ce_2Fe_{17}	238	$Ce_2Fe_{14}Al_3$	384
Pr_2Fe_{17}	298	$Pr_2Fe_{16}Mn$	308
Nd_2Fe_{17}	330	$Nd_2Fe_{13.5}Al_{3.5}$	470
Dy_2Fe_{17}	370	$Dy_2Fe_{14}Ga_3$	557
Ho_2Fe_{17}	330	$Ho_2Fe_{14}Ga_3$	560
Er_2Fe_{17}	305	$Er_2Fe_{14}Si_3$	498
Tm_2Fe_{17}	288	$Tm_2Fe_{16}Cr$	440
Lu_2Fe_{17}	275	$Lu_2Fe_{13.5}Si_{3.5}$	480

atoms in R_2Fe_{17} or introducing interstitial atoms (N,C) into R_2Fe_{17} intermetallic, can improve T_c. It is known that heavy rare earth provides high M_A in the compounds.

Fidler et al. reported that substitution of refractory elements such as (Ti, Zr, V, Mo, Nb, W) can bring in grain refinement and hence enhance magnetic properties of R_2Fe_{17} intermetallic. Furthermore, it has reported that presence of partial amorphous phase may strongly influence the effect of grain size on the transformation [46, 47], consequently improve the magnetic properties of the intermetallics.

Rational

The structural properties of R_2Fe_{17} compounds have been extensively investigated. Furthermore, its interstitial solid solutions based on carbon [48, 49], nitrogen [45] and substitutional solid solutions [35, 36, 37] also studied. However, the substitution of bigger metalloid like Nb atom on Fe atom is limited. By substitution Fe atom in R_2Fe_{17} compounds, either it brings contraction (substituting smaller atom like Al) or expansion (substituting bigger atom like Ga) in the unit cell volume of the parent compound or sometime change in crystal structure. These kinds of changes are interesting from crystallographic point of view. Furthermore, it is interesting to know whether the substituted atoms replace Fe atoms at random or occupy only specific Fe sites. In this thesis, attention is paid to substitution of non-magnetic Nb atom and weak magnetic Cr atom in place of strong magnetic Fe atom. Then study their influence on the crystallographic behavior and the magnetic properties of these compounds.

Based on the literature review we propose to study heavier rare-earth based R_2Fe_{17} intermetallics. The reasons for choosing havier R in these studies are (i) R has high M_A which enhances coercivity, H_c. (ii) heavier R has higher Bohr Magneton number

(Dy = 10.63 and Er = 9.59 μ_B ref. [4]) which brings enhancement in magnetization of the alloys. (iii) Heavier the rare earth have smaller the atomic sizes and higher mixing enthalpies with Fe, consequently larger the solubility of heavier rare earth elements in α-Fe [46]. Furthermore, substitution of Fe with Cr and Nb atoms change magnetic interaction between iron atoms. These substitutions can change the distance between iron-iron atoms which reduces negative exchange interaction between iron-iron atoms by distortion in the unit cell. This change can bring enhancement in the T_c of the alloys. (iv) To study the effect of microstructural changes on magnetic properties of these intermetallics via ball milling. As O. Mau, PhD Thesis [46], ball milling produces crystalline and amorphous phase. This can induce exchange spring behavior in material. This leads to an increase in saturation and remanence magnetization which in turn can improve energy product of the magnet.

3. Experiment

The Objectives of the Project

$R_2Fe_{17-x}TM_x$ (R: Dy, Er and TM: magnetic and non-mangetic or bigger or smaller transition metal substituent compared to Fe atom) compounds have attracted much attention for several years in the permanent magnets due to high magnetic anisotropy of the heavy R and high spontaneous M_s of the iron. Though there were a lot of studies on $R_2Fe_{17-x}TM_x$, particularly substitution of Fe atom with bigger non-magnetic atom (Nb), high energy ball milling studies, and Mössbauer studies in these intermetallics are limited.

Objectives:

1. To synthesis $R_2Fe_{17-x}Nb$ (or $Cr)_x$ (R: Dy, Er) intermetallic alloys.
2. To study the effect of Nb or Cr substitution on Fe sites and correlates structural and magnetic properties of the compounds.
3. Substitution of Nb or Cr ion for Fe is expected increment in the T_c of the compounds.
4. To do comparative studies on Dy and Er set of intermetallics.
5. To study the effect of HEBM on $R_2Fe_{16}Nb_1$ (R = Dy, Er, Gd) and correlate structural and magnetic properties of the compounds.

To pursue above objectives we synthesized following sets of samples:

(a) $Dy_2Fe_{17-x}Nb_x$ (x = 0, 0.25, 0.5, 0.75, 1.00, 1.25, 1.50)

(b) $Er_2Fe_{17-x}Nb_x$ (x = 0, 0.25, 0.5, 0.75, 1.00, 1.25, 1.50)

(c) $Dy_2Fe_{17-x}Cr_x$ (x = 0, 0.5, 1.0, 1.5, 2.0, 2.5, 3.0) & (d) $Gd_2Fe_{16}Nb$

Synthesis

The samples $R_2Fe_{17-x}Nb_x$ (R = Dy, Er, Gd; TM = Cr and Nb; x= 0.0, 0.25, 0.5, 0.75, 1.0, 1.25, 1.50) were prepared by arc melting high purity (99.99%) of Dy or Er or Gd, Fe, Nb or Cr, in stoichiometric ratio in high-purity argon atmosphere. The ingots were remelted at least four times to ensure their homogeneity. The phase and structure of samples were determined using X-ray powder diffraction (XRD) with Cu K_α radiation using Bruker D8 advance diffractometer. The magnetic properties of the samples were investigated using Superconducting Quantum Interface Device (SQUID) at 5, 77 and 300 K. The Curie temperature, T_c, was determined using Vibrating Sample magnetometer (VSM) in the field of 40 kA/m. ^{57}Fe Mössbauer spectra were collected at room temperature (RT) with a 25 mCi ^{57}Co Rh source and was calibrated at RT with an α-Fe foil using SEECO Inc. spectrometer.

Ball Milled $R_2Fe_{16}Nb$

The most important parameters that affect the final microstructure of the alloys and properties of the powder are: (1) ball milling impact energy on particles which can be control by choosing right mass proportion of sample to ball, size and density of ball, milling speed; (2) milling time; (3) milling atmosphere; (4) type of mill.

Keeping these above parameters in the consideration, arc melter synthesized $R_2Fe_{16}Nb_1$ alloys were ball milled in the following conditions: (i) The ball to powder mass ratio was maintained 10:1 for all milled alloys, (ii) each set of alloy were milled for 0min, 30 min, 60 min, and 90 min (0 min is starting alloy), (iii) Alloys were milled in the presence of 99.99% pure ethanol in order to avoid agglomeration of powder particles, and

(iv) HEBM was carried out in a stainless steel container using steel balls with powder at a speed of 1200 rpm using Arcos International ball milling device.

Sample characterization

X-ray Diffraction (XRD)

X-ray diffraction is well established and reliable method for the analysis of structures and phases. In the present study, it was used extensively for phase identification, lattice parameters determination, quantitative phase analysis, and determination of disorder in stoichiometric compounds.

X-ray diffractometer with Cu-K_α radiation (wavelength λ=1.54056 Å) was used to find the crystallinity and phase of samples. The samples were prepared by spreading nanoparticles on a zero background (Si) sample holder. Diffraction pattern was obtained at room temperature between 20 – 75^o 2θ angles. The patterns were matched with ICCD database.

Vibrating Sample Magnetometer (VSM) and Superconducting Quantum Interference Device (SQUID)

The hysteresis loops of the samples were measured by SQUID (Quantum Design) and VSM (Dexing Magnet, China) at 5, 77, and 300 K. From the loops, we obtained magnetic properties such as the saturation magnetization moment (M_s), coercive field (H_c), remenance (M_r). Furthermore, low and high temperature magnetization (M) vs temperature (T) measurements at 500 Oe (40 kA/m) were performed by VSM in order to obatin Curie temperature of the intermetallics.

Mössbauer Spectroscopy

Mössbauer spectroscopy is powerful technique to know electrical, magnetic, structural properties, and even quantitative phase analysis within samples. It uses the recoil-free resonant emission or absorption of γ-rays in a solid matrix, i. e. emission and absorption of γ-rays without loss of energy to the lattice. The isotopes with the strongest recoiless resonant absorption is ^{57}Fe . Fig. 3.1 shows emission of γ-rays and decay ^{57}Fe from a source containing the radioactive parent isotope ^{57}Co. For ^{57}Fe Mössbauer spectroscopy, the natural linewidth (Γ) of the 14.4 KeV transition is 4.6×10^{-9} eV. By capturing electron as in Fig. 3.1, ^{57}Co decays to an excited state of Mössbauer isotope ^{57}Fe. This excited state subsequently (about 10%) passes from metastable I = 3/2 state to its ground state (I = 1/2) by recoil-free emission of 14.4 KeV γ-ray used in the experiment (I is the nuclear spin).

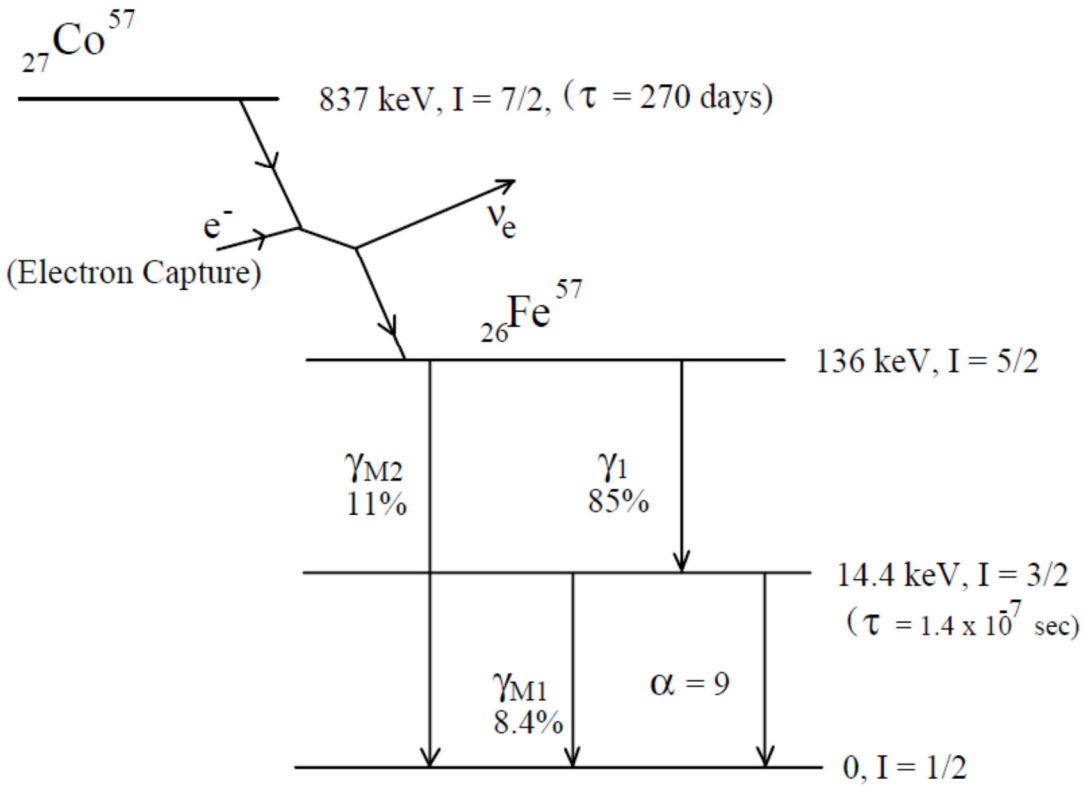

Figure 3.1: Nuclear decay scheme of ^{57}Co [http://www.webres.com]. Intensities are given in % of decay.

The observed γ-rays by recoil-free emission are shone a through a sample (absorber) containing ^{57}Fe atoms in the ground state as shown in Fig. 3.2. It shows schematic diagram of Mössbauer spectroscopy set up. It consists of a source "^{57}Co" which moves relative to the sample (absorber) and a counter to monitor the intensity of the beam after it has passed through the sample. Thus Mössbauer spectrum is a plot of the counting rate against the source velocity (mm/s), i.e., the beam energy. Mössbauer spectroscopy of sample was conducted with SECCO spectrometer using ^{57}Co γ-source in the temperature range of 77 –

300 K. The spectrometer was calibrated using α-Fe. The spectra were plotted with WMOSS software. The isomer shift (δ or IS), hyperfine field (B_{hf}) and quadrupole splitting (Δ or QS) were extracted from the fit.

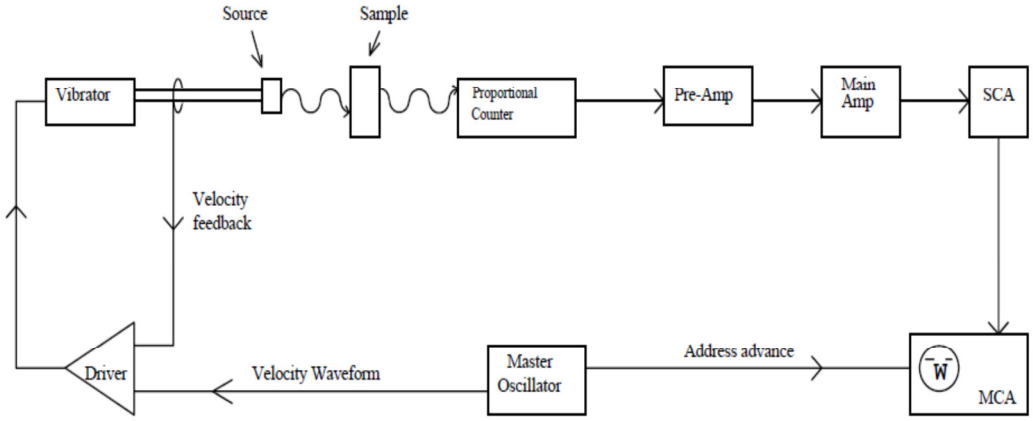

Figure 3.2: Schematic diagram of Mössbauer spectroscopy set up.

The interactions between the Mössbauer nucleus and its surrounding environment are magnetic and electrostatic in nature. This interaction called hyperfine interactions which brings modification of the energy levels in the absorbing nuclei by three main interactions: (i) isomer shift, (ii) magnetic hyperfine interaction and (iii) quadrupole interaction.

(i) **Isomer Shift (δ)**: This is shift observed in the resonance energy of the transition caused by difference in s-electron environment of absorber and source. It shifts the whole spectrum either toward the left or right from center depending on negative or positive isomer shift. It is mainly arises due to the

non-zero volume of the nucleus and the charge density due to s-electrons within it.

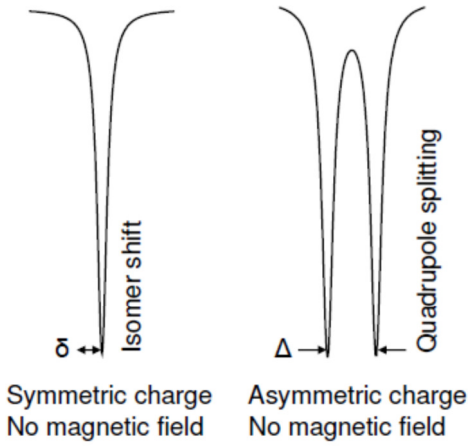

Figure 3.3: Isomer shift and Quadrupole splitting.

(ii) **Quadrupole interaction (Δ)**: The electric quadruploe moment (eQ) is a measure non-spherical nuclear charge distribution which arises with each nuclei state having an angular momentum quantum number I > 1/2. This asymmetry distribution of charges surrounding the Mössbauer nucleus results in an inhomogeneous electric field driven by the electric field gradient at the nucleus. The interaction between the electric quadrupole moment and the electric field gradient called quadrupole interaction. This interaction splits the nuclear energy levels. This is shown in Fig 3.3, giving a two line spectra or 'doublet'.

(iii) **Magnetic Hyperfine interaction:** The magnetic hyperfine interaction (Zeeman Splitting) arises from the coupling of the magnetic dipole moment μ of ^{57}Fe nucleus with applied magnetic field B at the nucleus. It results in

splitting of the nuclear ground and excited stats if they have nuclear spin I > 0 as shown in the Fig. 3.4. In Fig. 3.4, there is only six transition from I = 1/2 to I = 3/2 are allowed instead of 8 transition because it is subjected into the selection rule: $\Delta m = 0, \pm 1$, for magnetic dipole transition. It comprises sextet spectrum in the Mössbauer study which closely related to magnetic field experience by nucleus below T_c called internal hyperfine field B_{hf}. The internal hyperfine field B_{hf} at a Fe nucleus is

$$B_{hf} = (B_{contact} + B_o + B_d) + B_{app} \qquad (2)$$

where the first three terms being due to the atom's own partially filled electron shells. $B_{contact}$ is polarising the spin density at the nucleus, B_o the orbital moment on those electrons, B_d the dipolar field, and B_{app} applied ext. field.

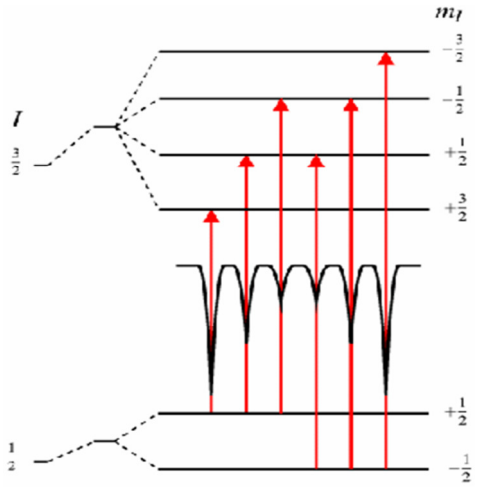

Figure 3.4: Magnetic splitting of the nuclear energy levels.

4. Results and Discussions

Structural analysis of $R_2Fe_{17-x}Nb_x$ (R: Dy and Er)

Figure 4.1 shows the XRD patterns of the $Er_2Fe_{17-x}Nb_x$ alloys with various Nb concentrations. The XRD results show that the samples have Th_2Ni_{17}-type structure (space group, P63/mmc).

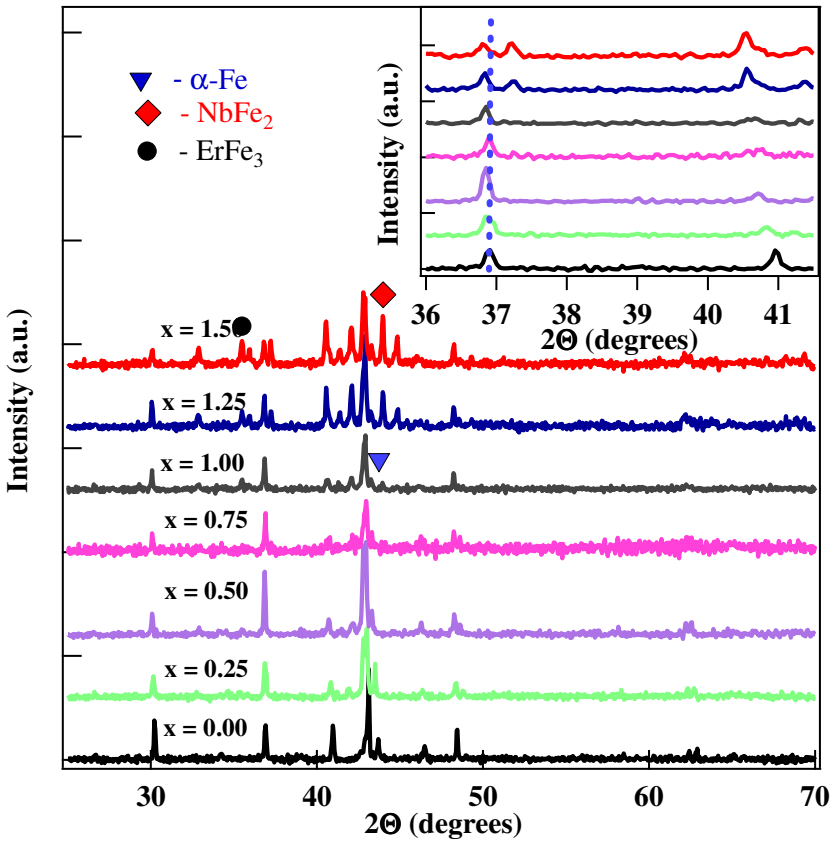

Figure 4.1: X-ray diffraction patterns of $Er_2Fe_{17-x}Nb_x$ compounds.

The samples are in single phase up to x = 1 except small amount of α-Fe [50] present at x = 1. This shows that maximum the concentration of Nb which can be doped in Er_2Fe_{17} to obtain pure phase is x = 0.75. With higher concentration of

Nb (x > 1) the XRD patterns contain some impurities of $NbFe_2$ and $ErFe_3$ phase which are undesirable because they suppress the coercivity and magnetostriction properties of the alloys [51, 52]. Furthermore, beyond x = 1, α-Fe peak disappears which is consistent with the argument that the addition of small amount of Nb or Zr suppresses the formation of free iron [53, 54].

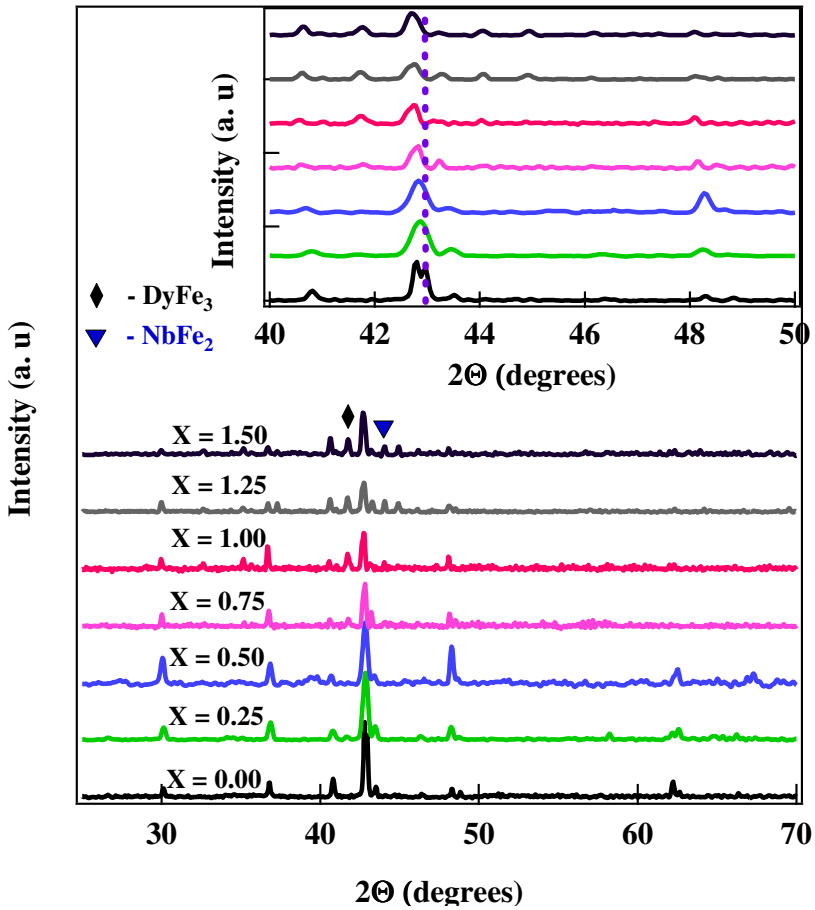

Figure 4.2: X-ray diffraction patterns of $Dy_2Fe_{17-x}Nb_x$ compounds.

But the XRD of $Dy_2Fe_{17-x}Nb_x$ alloys (see Fig. 4.2) show two impurities phases viz. $DyFe_3$ and $NbFe_2$ at x = 1. At lower and higher concentration of Nb results are the

same as $Er_2Fe_{17-x}Nb_x$ alloys. Similar impurities have been observed in the papers [52, 55, 56] with higher Nb concentrations. This result is further supported by the Rietveld analysis (see Fig. 4.3) of the XRD patterns, where the best fit of the data is obtained by taking into account these impurities. With the Nb substitution a gradual shift in the peaks to the left is observed as compared to that of pure Er_2Fe_{17}. This is due to the fact that bigger Nb atoms are substituted on Fe site which brings in lattice expansion. Rietveld Refinement fit of XRD patterns is shown in Fig. 4.3.

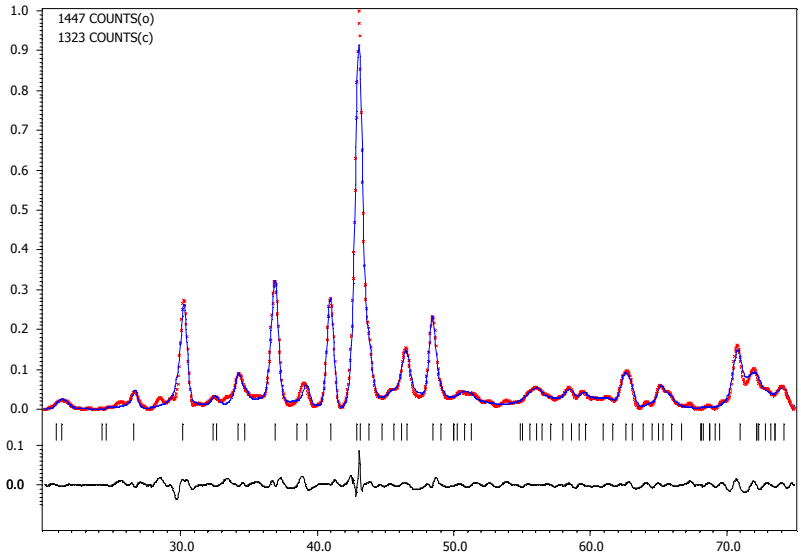

Figure 4.3a: Rietveld refined profile for Er_2Fe_{17} compound.

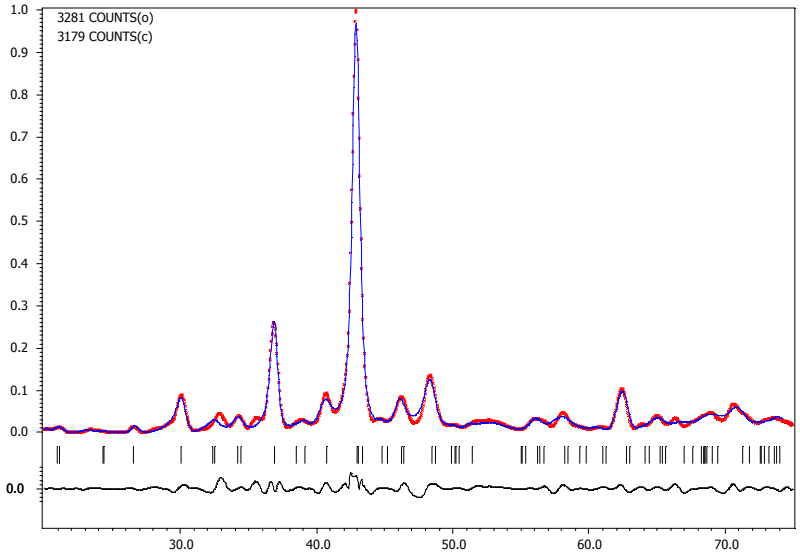

Figure 4.3b: Rietveld refined profile for $Er_2Fe_{16.5}Nb_{0.5}$ compounds.

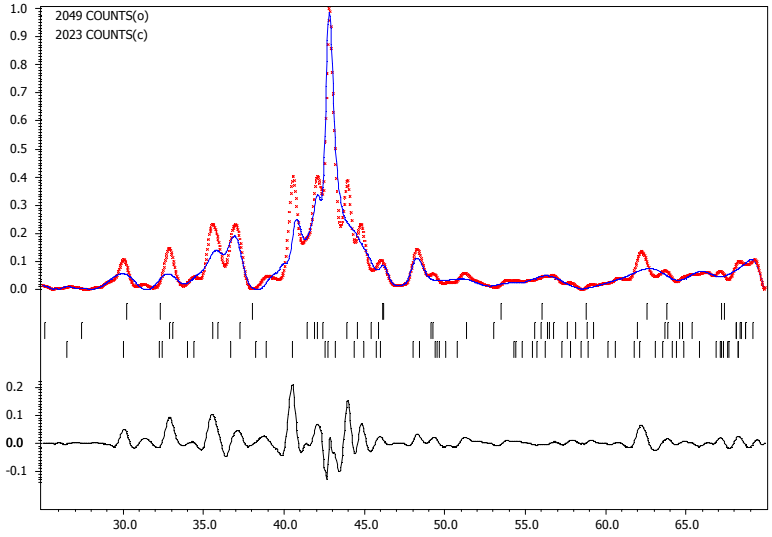

Figure 4.3c: Rietveld refined profile for $Er_2Fe_{15.75}Nb_{1.50}$ compounds.

Rietveld refinement shows that the Nb atoms preferentially occupy the 12*k* sites of Fe and small fraction of Nb also goes to 6c site (see Table 2). Figure 4.4 shows the structural parameters *a* and *c*, as a function of Nb doping *x*. The lattice constants are calculated using the following formula:

$$d_{(hkl)} = \left(\frac{4}{3} \frac{h^2 + hk + k^2}{a^2} + \frac{l^2}{c^2} \right)^{-\frac{1}{2}}, \qquad (3)$$

Where d(*hkl*) is the crystal face distance and (*hkl*) is the Miller indices. The unit-cell volume is calculated using the formula:

$$V = a^2 c \sin 60°, \qquad (4)$$

Table 2: Atomic site occupancy for $Er_2Fe_{17-x}Nb_x$

Elements	x = 0.00 s.o.f (ai)	x = 0.25 s.o.f (ai)	x = 0.50 s.o.f (ai)	x = 0.75 s.o.f (ai)	x = 1.00 s.o.f (ai)	x	y	z
Fe(4f)	0.166667	0.16520	0.16261	0.16014	0.15972	0.333	0.666	0.104
Fe(6g)	0.250000	0.24362	0.24642	0.24564	0.24431	0.500	0.000	0.000
Fe(12j)	0.500000	0.49359	0.47338	0.46222	0.45342	0.330	-0.04	0.250
Fe(12k)	0.500000	0.51184	0.49406	0.48952	0.48471	0.165	0.330	0.983
Nb1(4f)		0.00201	0.00490	0.00769	0.00941	0.333	0.666	0.104
Nb2(6g)		0.00003	0.00743	0.01132	0.01563	0.500	0.000	0.000
Nb3(12j)		0.00785	0.01461	0.01729	0.01956	0.330	-0.04	0.250
Nb4(12k)		0.00935	0.01474	0.01879	0.01961	0.165	0.330	0.983

* s.o.f. - Site-Occupancy Factors

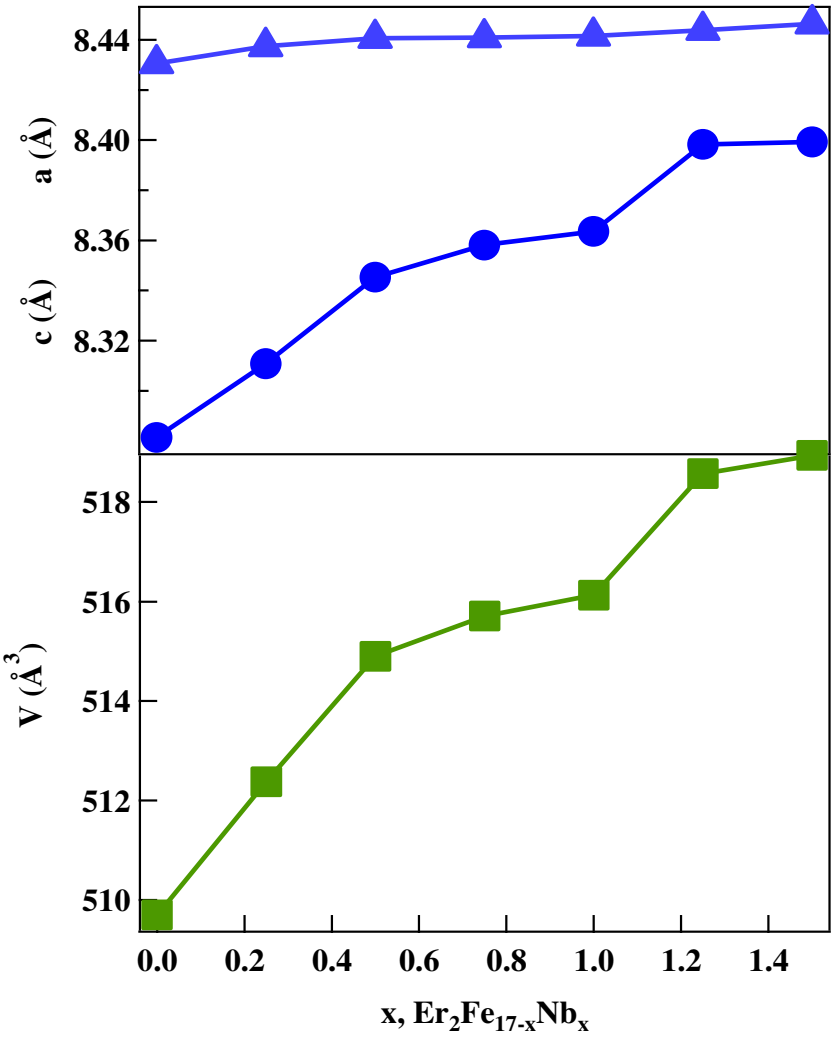

Figure 4.4a: Lattice parameters and unit cell volume of $Er_2Fe_{17-x}Nb_x$ compounds.

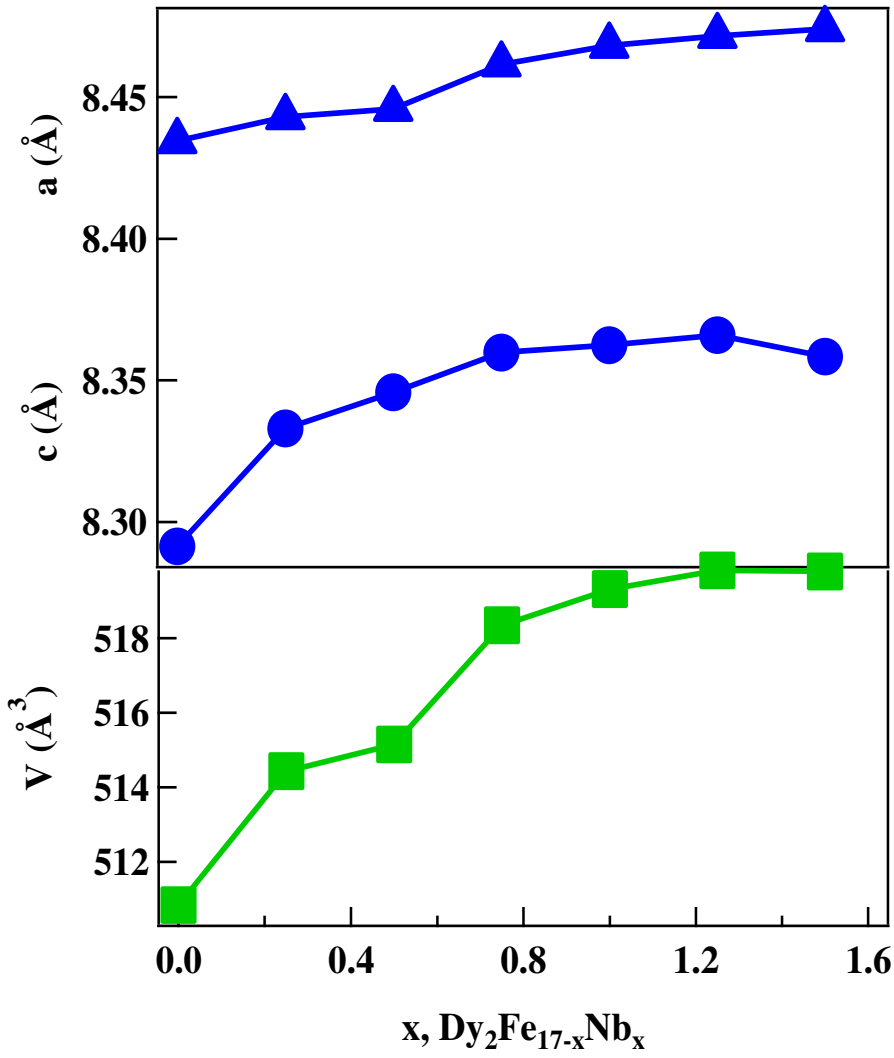

Figure 4.4b: Lattice parameters and unit cell volume of $Dy_2Fe_{17-x}Nb_x$ compounds.

The calculated lattice parameters and the unit-cell volume obtained from XRD patterns of the alloys are listed and shown in Table 3 and Fig. 4.4 respectively. A linear unit-cell volume expansion was observed (6.47 Å^3/Nb for $Er_2Fe_{17-x}Nb_x$ and 8.35 Å^3/Nb for $Dy_2Fe_{17-x}Nb_x$) at the lower concentration of the Nb. The linear expansion results because of larger radius of Nb (0.86 Å) replacing smaller Fe (0.63 Å) atom. However, at

higher concentration of the Nb, the formation of paramagnetic $NbFe_2$ phase appears which reduces the Nb concentration to the $R_2Fe_{17-x}Nb_x$. As a result, linearity in the volume expansion was not noticed at higher concentration of Nb. The trend of lattice parameters and unit-volume cell expansion is in agreement with the previous study on the $Ce_2Fe_{17-x}Ga_x$ [57], $Dy_2Fe_{17-x}Ga_x$ [38], and also with Rietveld analysis (see Table 4).

Table 3: Lattice parameters and unit cell volume of $R_2Fe_{17-x}Nb_x$ (or $Cr)_x$ compounds.

	$Dy_2Fe_{17-x}Nb_x$			**$Er_2Fe_{17-x}Nb_x$**			**$Dy_2Fe_{17-x}Cr_x$**			
X	a, (Å)	c, (Å)	V, (Å^3)	a, (Å)	c, (Å)	V, (Å^3)	X	a, (Å)	c, (Å)	V, (Å^3)
0.00	8.434	8.291	510.84	8.430	8.281	509.70	0.0	8.443	8.320	513.71
0.25	8.443	8.333	514.43	8.437	8.311	512.38	0.5	8.452	8.295	513.24
0.50	8.445	8.345	515.15	8.441	8.345	514.90	1.0	8.429	8.329	512.47
0.75	8.461	8.359	518.35	8.441	8.358	515.71	1.5	8.426	8.315	511.35
1.00	8.468	8.362	519.32	8.442	8.363	516.13	2.0	8.419	8.320	511.07
1.25	8.471	8.365	519.82	8.444	8.398	518.57	2.5	8.418	8.317	510.52
1.50	8.474	8.358	519.79	8.446	8.399	518.94	3.0	8.413	8.320	510.11

Table 4: Structural parameters from Rietveld refinement powder XRD data $Er_2Fe_{17-x}Nb_x$ using Rietveld Analysis.

Parameters	x = 0.00	x = 0.25	x = 0.50	x = 0.75	x = 1.00
a, (Å)	8.4289(75)	8.4344(15)	8.4385(5)	8.4417(57)	8.4428(55)
c, (Å)	8.2773(43)	8.2843(15)	8.3044(43)	8.3213(96)	8.3434(12)
V, (Å^3)	509.2938(4)	511.448(6)	513.753(2)	514.31(525)	515.1489

Magnetic properties of $R_2Fe_{17-x}Nb_x$ (R: Dy and Er)

The saturation magnetization of $R_2Fe_{17-x}Nb_x$ at 5 and 300 K is reported in the Table 5. Fig. 4.5a and 4.5b show that the saturation magnetization of $R_2Fe_{17-x}Nb_x$ is decreasing with increasing Nb concentration at 5 and 300 K. This result is in close agreement with the $Ce_2Fe_{17-x}Ga_x$ [57], $Dy_2Fe_{17-x}Ga_x$ [38], $R_2Fe_{17-x}Al_xC$ [58] result. The decrease in magnetization partly comes from decrease in magnetic moment of Fe atoms / or comes from the overexpansion of lattice parameters due to substitution of non magnetic Nb atoms. A great drop in M_s was observed beyond x = 1 because of the formation of RFe_3 and $NbFe_2$ phases at the expense of Fe from R_2Fe_{17} phase. This effect is more pronounced in $Er_2Fe_{17-x}Nb_x$ than $Dy_2Fe_{17-x}Nb_x$ compounds as shown in the Fig. 4.5a. It was observed from the XRD pattern that up to x = 1, RFe_3 and $NbFe_2$ phases were absent in the Er set of samples but RFe_3 phase was present in the Dy set of samples. It is obvious that, formation of RFe_3 phase dilute the more Fe magnetic moment more than the formation of $NbFe_2$ phase. It confirms that dilution of Fe magnetic moment in Er set of samples is faster than Dy set. This explains why the abrupt drop there is in M_s of Er set of samples but not in Dy set.

Table 5: Curie temperature and saturation magnetization of $R_2Fe_{17-x}Nb$ (or Cr)$_x$ alloys.

$Dy_2Fe_{17-x}Nb_x$				$Er_2Fe_{17-x}Nb_x$			$Dy_2Fe_{17-x}Cr_x$			
X	T_c (K)	M_s, 5K (emu/g)	M_s, 300 K (emu/g)	T_c (K)	M_s, 5K (emu/g)	M_s, 300 K (emu/g)	X	T_c (K)	M_s, 5K (emu/g)	M_s, 300K (emu/g)
0.00	382	69	58	324	90	71	0.0	382	69.0	58
0.25	417	66	56	367	73	67	0.5		52.1	51
0.50	424	63	54	392	70	65	1.0	442	46.0	49
0.75	445	60	41	399	59	58	1.5	426	33.4	41
1.00	460	41	34	410	46	54	2.0	424	27.8	36
1.25	443	39.5	30	405	40	38	2.5	408	24.6	32
1.50	432	38	28	402	36.5	34	3.0	374	14.4	19

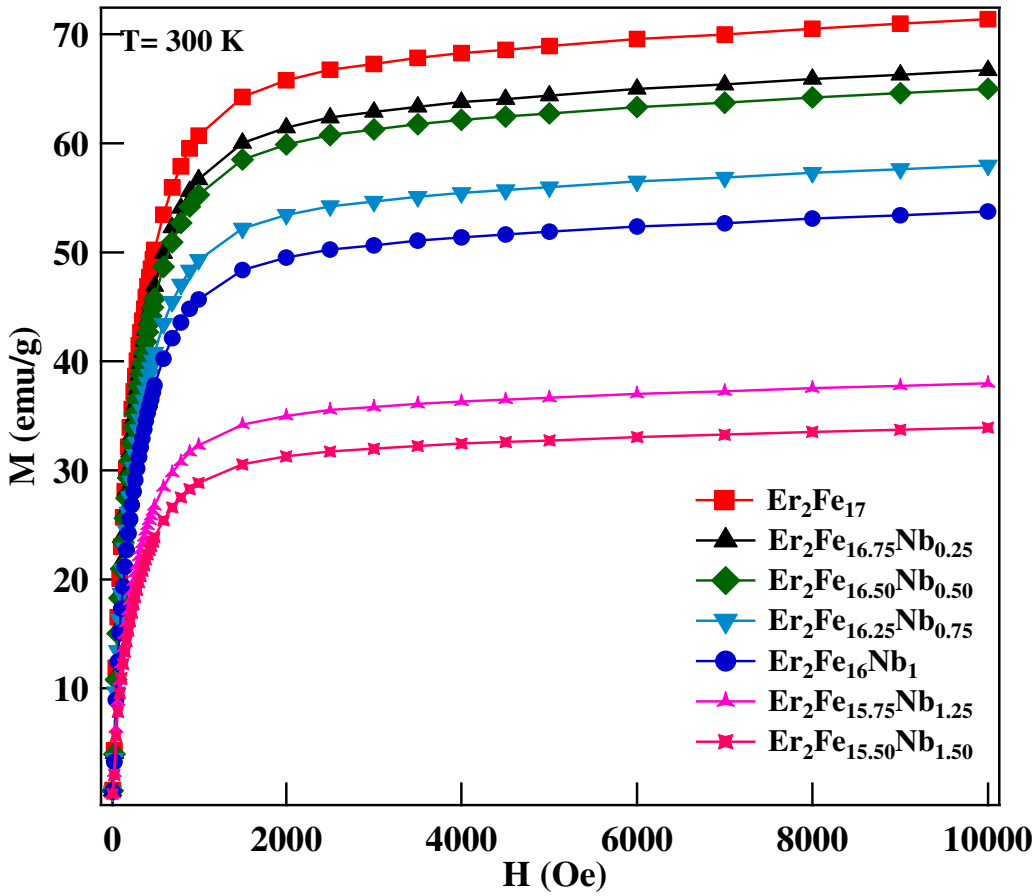

Figure 4.5a: Magnetization of $Er_2Fe_{17-x}Nb_x$ compounds.

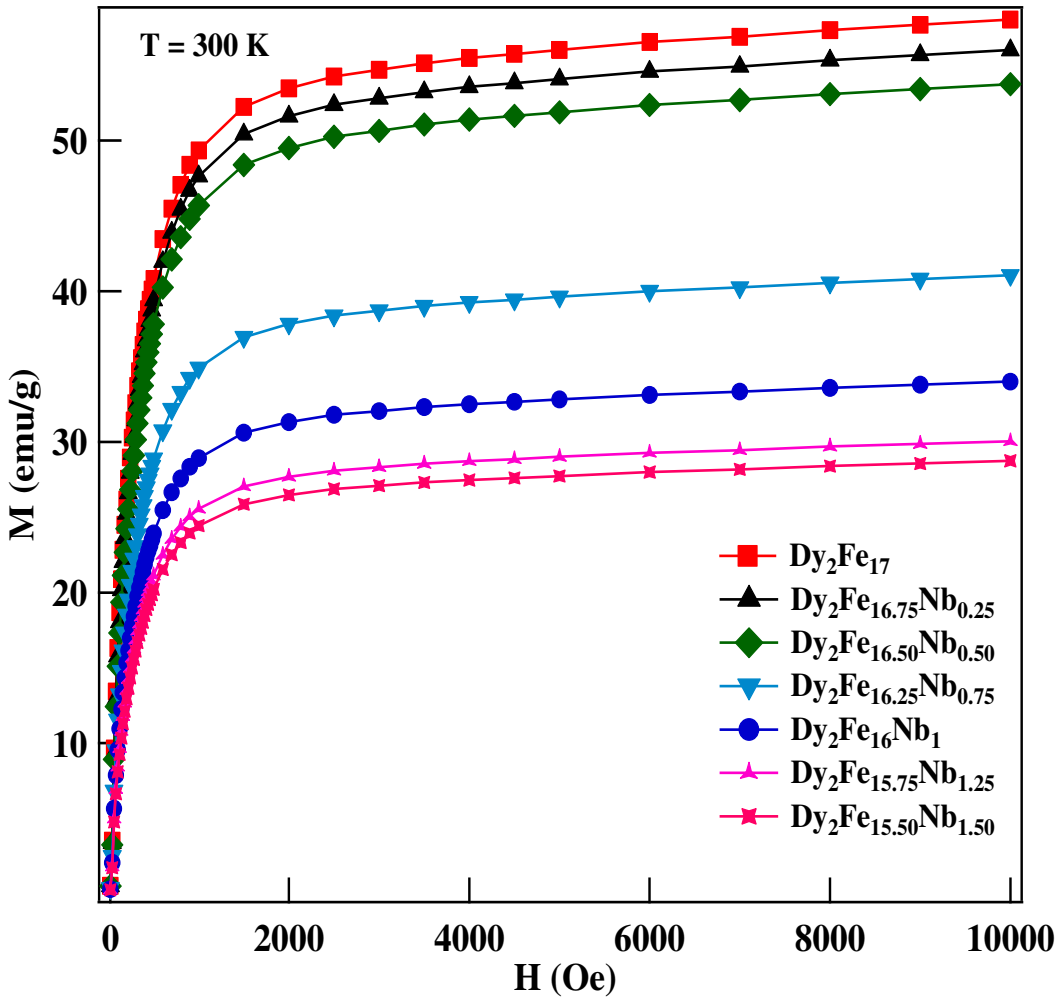

Figure 4.5b: Magnetization of $Dy_2Fe_{17-x}Nb_x$ compounds.

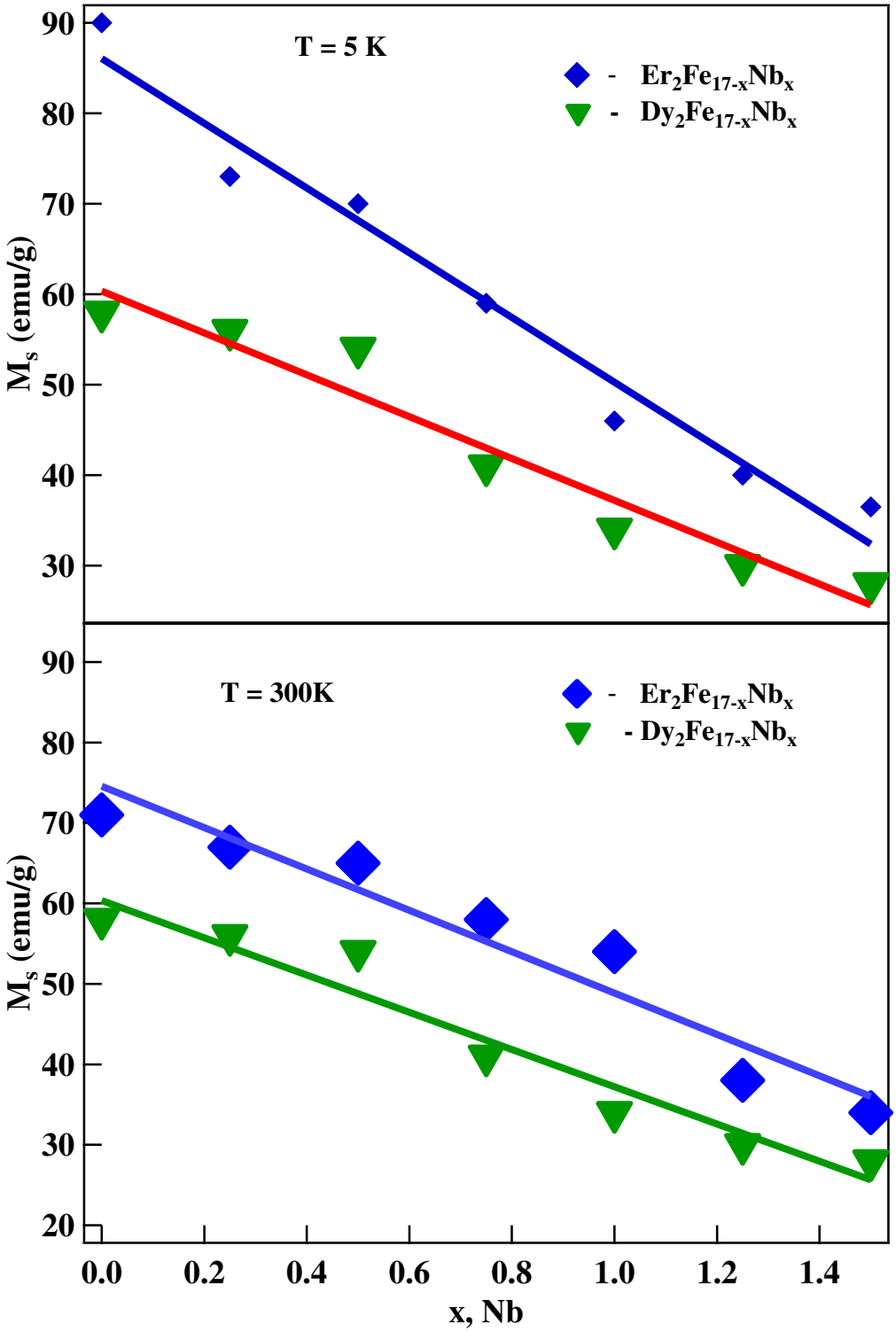

Figure 4.5c: Comparatives study of saturation magnetization of $Er_2Fe_{17-x}Nb_x$ and $Dy_2Fe_{17-x}Nb_x$ compounds.

The R_2Fe_{17} compound is the most iron-rich phase in the binary R-Fe alloy system and consequently has the highest magnetization. Within these R_2Fe_{17} compounds, the magnetization value increases and T_c value decreases as we move to higher atomic number of lanthanide series atom. This is because of the series contraction. As the lanthanide series contract, the concentration of electron in the unit cell increases which results in increase in magnetization while T_c decreases due to the decrease in the inter-atomic distance. Our result is consistent with above explanation. As we compared our results of $R_2Fe_{17-x}Nb_x$ (R: Dy and Er) samples, it was observed that Dy set of samples has smaller magnetization than Er set of samples. As per Belorizky et al. [59], the rapid decrease of the 4f-shell radius due to lanthanide contraction compared to the decrease in the atomic radius of R ions leads to a weaker hybridization of the 4f and 5d shells. This in turn leads to reduction of the 4d-3d exchange interactions. This effect is most prominent in the light rare earth atomic number. This effect dilutes for heavy rare earth atomic number and remains constant for 4d-3d exchange interactions over higher atomic rare earth atoms (see Fig. 20 of [60]). We assume that this is because the effect of faster decreases in lattice parameter of Er than Dy. According to Liu et al. [10], decreasing lattice parameter enhances the 3d-5d hybridization because the strength of the intersublattice exchange coupling would increase when passing through the lanthanide series. Concomitantly, the faster decrease in the lattice parameters increases the R-T interactions for higher atomic number of rare earth. Hence, we observed higher M_s of Er set of samples than for Dy set of samples. This result is further consistent with $R_2Fe_{17-x}Cr_x$ (R: Dy and Er) [61].

The T_c of the alloys is listed in the Table 5. The concentration dependence of T_c is shown in Fig. 4.6a and 4.6b. It was observed that T_c increased with Nb content 'x' in both (Dy and Er) set of samples up to x = 1. These results are consistent with others [61, 62]. The maximum in T_c ~ 460 K was observed for $Dy_2Fe_{16}Nb$ which is 80 K higher than that of Dy_2Fe_{17} alloy. Similarly the maximum T_c ~ 410 K was observed for $Er_2Fe_{16}Nb$ which is 90 K higher than that of Er_2Fe_{17} alloy.

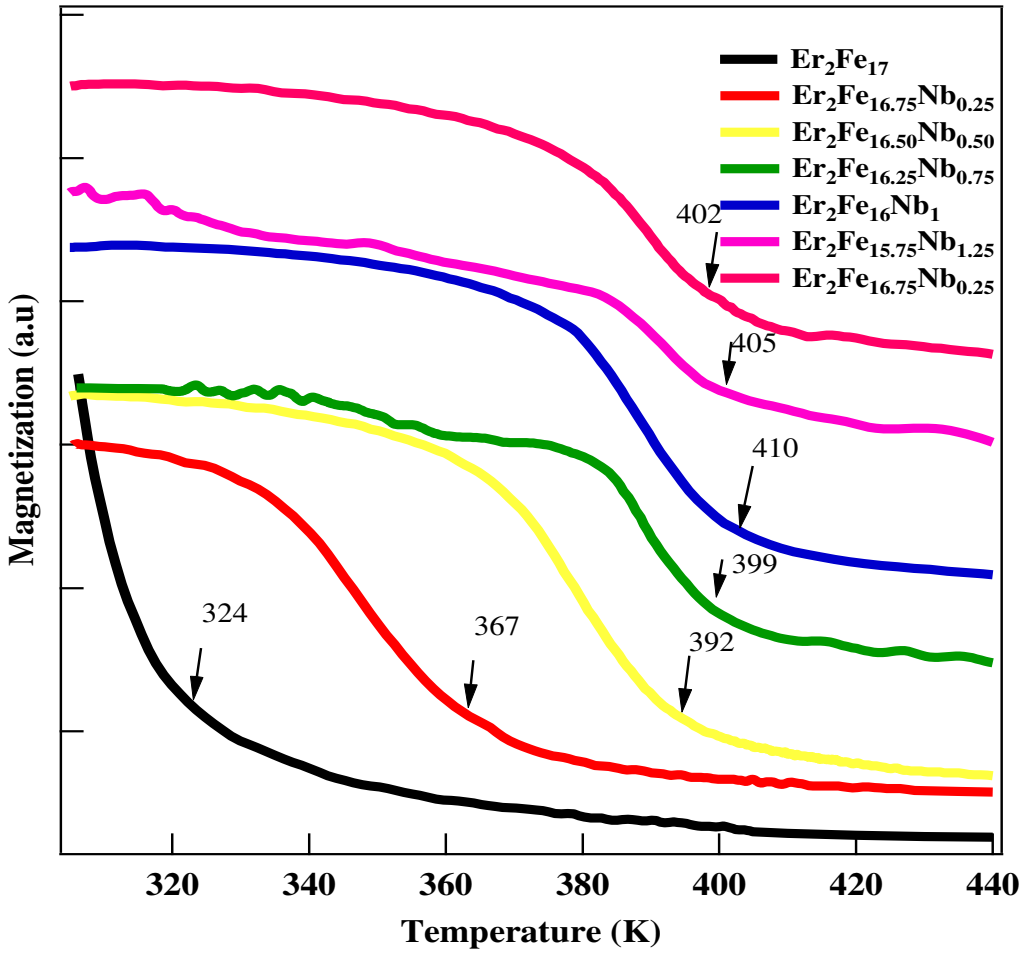

Figure 4.6a: Magnetization Vs Temperature plot for Curie temperature of $Er_2Fe_{17-x}Nb_x$ compounds.

It is known from the magnetic theory that there is an antiferromagnetic interaction between the Fe atoms at 4f sites, because the Fe-Fe bond length approaches 2.4 Å which is less than 2.45 Å needed for ferromagnetic ordering. The substitution of Nb atoms for Fe atoms on 4f sites increases the Fe-Fe distance. This in turn will increase the strength of exchange interaction which directly affects the T_c of the compounds. The observed T_c values for $R_2Fe_{17-x}Nb_x$ are superior to $R_2Fe_{17-x}M_x$ (M: Al and Cr) [63, 64], but at higher concentration ($x > 1$), T_c of the compounds decreased. This decrease in T_c is coming either from dilution effect of Fe or from overexpansion of the lattice parameter that leads to a weaker exchange interaction.

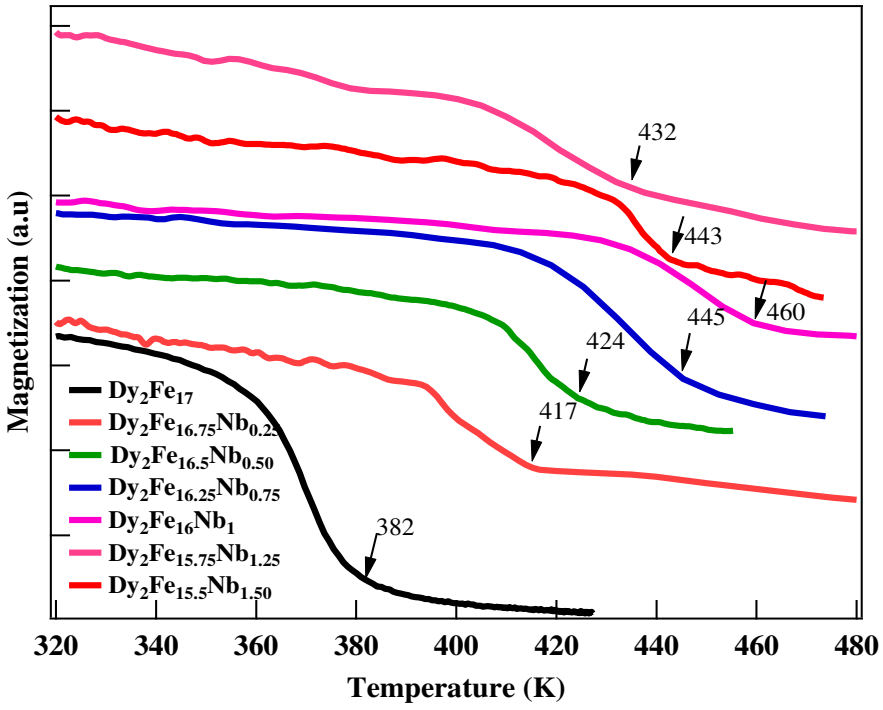

Figure 4.6b: Magnetization Vs Temperature plot for Curie temperature of $Dy_2Fe_{17-x}Nb_x$ compounds.

Mössbauer spectral analysis of $R_2Fe_{17-x}Nb_x$ (R: Dy and Er)

Mössbauer spectra of R_2Fe_{17} are very complex because of their complex crystal structures. There are four crystallographically distinct iron sites in R_2Fe_{17}. These sites for hexagonal R_2Fe_{17} crystal structure are denoted by Wyckoff notation 4*f*, 6*g*, 12*j*, and 12*k*. It indicates that at least four subspectra are needed correspond to four iron sites. But R_2Fe_{17} alloys have the easy direction of magnetization lying in the basal plane (along a or b axes in Dy_2Fe_{17} [65] and Er_2Fe_{17} [13]. This basal plane easy direction of magnetization further complicates the analysis of the spectra of R_2Fe_{17} because it comprises of four crystallographically inequvalent iron sites. The reason for inequivalent iron site is the vector character of the hyperfine field and tensor character of the electric field gradient [66]. Further magnetic splitting of *j* and *k* iron sites must be included to account for the existence of magnetically inequivalent sites. Since iron atom on the f site is along c-axis (easy axis magnetization direction) and g site is most likely along the c-axis, one sextet for each site was assigned. However, since iron atoms on *j* and *k* sites are along the basal plane, these sites are further splits into two subspectra [13].

Mossbauer studies of R_2Fe_{17} have been investigated by Gubbens, Buschow, G. J. Long and others [67-70]. In our present study, either 6 or 7 or 8 magnetic sextets are used to fit the Mössbauer spectra in the absence or presence of one impurity phase or two impurities phases, respectively. Mössbauer spectrum of $R_2Fe_{17-x}Nb_x$ alloys at RT is shown in the Figure 4.7. The Mössbauer spectral analysis was carried with magnetic sextets assigned to the 4*f*, 6*g*, 12*j*, and 12*k* sites in $R_2Fe_{17-x}Nb_x$. This spectrum nature is very similar to that of $Ce_2Fe_{17-x}Ga_x$ [57], and $Er_2Fe_{17-x}Si_x$ alloys [40]. Mössabuer spectra

of $R_2Fe_{17-x}Nb$ (or Cr)$_x$ alloys was measured at 300 K. Hyperfine parameters of $R_2Fe_{17-x}Nb_x$ alloys are given in Table 5 & 6.

Table 6: Mössbauer parameters of $Er_2Fe_{17-x}Nb_x$ compounds.

Hyperfine Field (B_{hf})	**x**	***4f***	**$Fe/ErFe_3$**	***6g***	***12j₁***	***12j₂***	***12k₁***	***12k₂***
Er_2Fe_{17}	0.00	157		194	88	131	111	34
$Er_2Fe_{16.75}Nb_{0.25}$	0.25	190		215	89	163	158	40
$Er_2Fe_{16.50}Nb_{0.50}$	0.50	190		217	93	164	162	37
$Er_2Fe_{16.25}Nb_{0.75}$	0.75	196		223	118	168	164	30
$Er_2Fe_{16}Nb$	1.00	232	329	262	156	196	198	24
$Er_2Fe_{15.75}Nb_{1.25}$	1.25	217	204	204	145	173	194	12
$Er_2Fe_{15.5}Nb_{1.50}$	1.50	217	198	200	145	169	193	12
Isomer Shift (δ)	**x**	***4f***	**$Fe/ErFe_3$**	***6g***	***12j₁***	***12j₂***	***12k₁***	***12k₂***
Er_2Fe_{17}	0.00	-0.07		-0.229	-0.082	-0.082	-0.076	-0.076
$Er_2Fe_{16.75}Nb_{0.25}$	0.25	-0.132		-0.067	-0.214	-0.214	-0.085	-0.085
$Er_2Fe_{16.50}Nb_{0.50}$	0.50	-0.145		-0.109	-0.197	-0.197	0.034	0.034
$Er_2Fe_{16.25}Nb_{0.75}$	0.75	-0.152		-0.087	-0.183	-0.183	0.030	0.030
$Er_2Fe_{16}Nb$	1.00	-0.164	-0.484	-0.008	-0.189	-0.189	-0.323	-0.323
$Er_2Fe_{15.75}Nb_{1.25}$	1.25	-0.098	-0.040	-0.152	-0.152	-0.152	-0.231	-0.231
$Er_2Fe_{15.5}Nb_{1.50}$	1.50	-0.122	-0.102	-0.164	-0.164	-0.164	-0.235	-0.235
Quadruple Splitting (ΔE_Q)	**x**	***4f***	**$Fe/ErFe_3$**	***6g***	***12j₁***	***12j₂***	***12k₁***	***12k₂***
Er_2Fe_{17}	0.00	0.257		0.5	0.096	0.072	0.042	-0.005
$Er_2Fe_{16.75}Nb_{0.25}$	0.25	-0.017		0.027	0.498	-0.044	0.348	0.072
$Er_2Fe_{16.50}Nb_{0.50}$	0.50	0.069		-0.022	0.495	0.068	0.443	-0.034
$Er_2Fe_{16.25}Nb_{0.75}$	0.75	0.089		-0.042	0.326	0.04	0.344	-0.262
$Er_2Fe_{16}Nb$	1.00	0.037	0.091	-0.091	0.034	-0.173	0.41	0.523
$Er_2Fe_{15.75}Nb_{1.25}$	1.25	0.358	-0.0801	0.132	0.104	-0.486	0.772	0.024
$Er_2Fe_{15.5}Nb_{1.50}$	1.50	0.28	0.0605	-0.022	0.103	-0.445	0.801	0.033

Generally, R_2Fe_{17} phase is fitted with six sextets (4*f*, 6*g*, 12j_1, 12j_2, 12k_1, 12k_2) for four in-equivalent iron sites. In our present study, some impurities phases were observed at higher concentration of Nb substitution. So, higher number of sextets (7 or 8) was assigned for Mössbauer spectral analysis. For examples, 8 sextets for $Er_2Fe_{15.75}Nb_{1.25}$ and 7 sextets for $Er_2Fe_{16}Nb_1$ sample, to account for additional phases in $NbFe_2$ and the similar

result was observed for $ErFe_3$ for $Er_2Fe_{15.75}Nb_{1.25}$ and α-Fe phase for $Er_2Fe_{16}Nb_1$. These additional phases were also detected in XRD of these samples.

Table 7: Mössbauer parameters of $Dy_2Fe_{17-x}Nb_x$ compounds.

Hyperfine Field (B_{hf})	**x**	***4f***	**$Fe/DyFe_3$**	***6g***	***12j₁***	***12j₂***	***12k₁***	***12k₂***
Dy_2Fe_{17}	0.00	253		206	226	182	190	198
$Dy_2Fe_{16.75}Nb_{0.25}$	0.25	266		214	234	169	193	194
$Dy_2Fe_{16.50}Nb_{0.50}$	0.50	277		232	228	180	198	200
$Dy_2Fe_{16.25}Nb_{0.75}$	0.75	270		231	233	179	200	200
$Dy_2Fe_{16}Nb$	1.00	271		232	229	168	201	200
$Dy_2Fe_{15.75}Nb_{1.25}$	1.25	268	193	215	218	184	214	181
$Dy_2Fe_{15.5}Nb_{1.50}$	1.50	251	188	214	216	176	199	200
Isomer Shift (δ)	**x**	***4f***	**$Fe/DyFe_3$**	***6g***	***12j₁***	***12j₂***	***12k₁***	***12k₂***
Dy_2Fe_{17}	0.00	0.043		-0.181	-0.105	-0.105	-0.106	-0.106
$Dy_2Fe_{16.75}Nb_{0.25}$	0.25	0.039		-0.155	-0.110	-0.110	-0.120	-0.120
$Dy_2Fe_{16.50}Nb_{0.50}$	0.50	-0.285		0.419	-0.328	-0.328	-0.399	-0.399
$Dy_2Fe_{16.25}Nb_{0.75}$	0.75	0.105		-0.152	-0.120	-0.120	-0.141	-0.141
$Dy_2Fe_{16}Nb$	1.00	0.060		-0.122	0.095	0.095	-0.150	-0.150
$Dy_2Fe_{15.75}Nb_{1.25}$	1.25	-0.138	0.043	-0.267	-0.228	-0.228	-0.500	-0.500
$Dy_2Fe_{15.5}Nb_{1.50}$	1.50	-0.131	0.002	-0.084	-0.081	-0.081	-0.447	-0.447
Quadruple Splitting (ΔE_Q)	**x**	***4f***	**$Fe/DyFe_3$**	***6g***	***12j₁***	***12j₂***	***12k₁***	***12k₂***
Dy_2Fe_{17}	0.00	0.024		0.045	-0.031	0.400	-0.273	0.424
$Dy_2Fe_{16.75}Nb_{0.25}$	0.25	0.015		0.015	-0.022	-0.060	0.021	0.408
$Dy_2Fe_{16.50}Nb_{0.50}$	0.50	0.011		-0.302	0.237	0.016	-0.109	0.226
$Dy_2Fe_{16.25}Nb_{0.75}$	0.75	-0.156		-0.237	0.240	-0.079	-0.061	-0.500
$Dy_2Fe_{16}Nb$	1.00	-0.068		-0.386	0.125	-0.082	0.232	-0.255
$Dy_2Fe_{15.75}Nb_{1.25}$	1.25	-0.077	-0.266	0.466	-0.195	-0.500	-0.228	-0.496
$Dy_2Fe_{15.5}Nb_{1.50}$	1.50	-0.122	0.028	0.234	0.392	0.500	-0.469	0.103

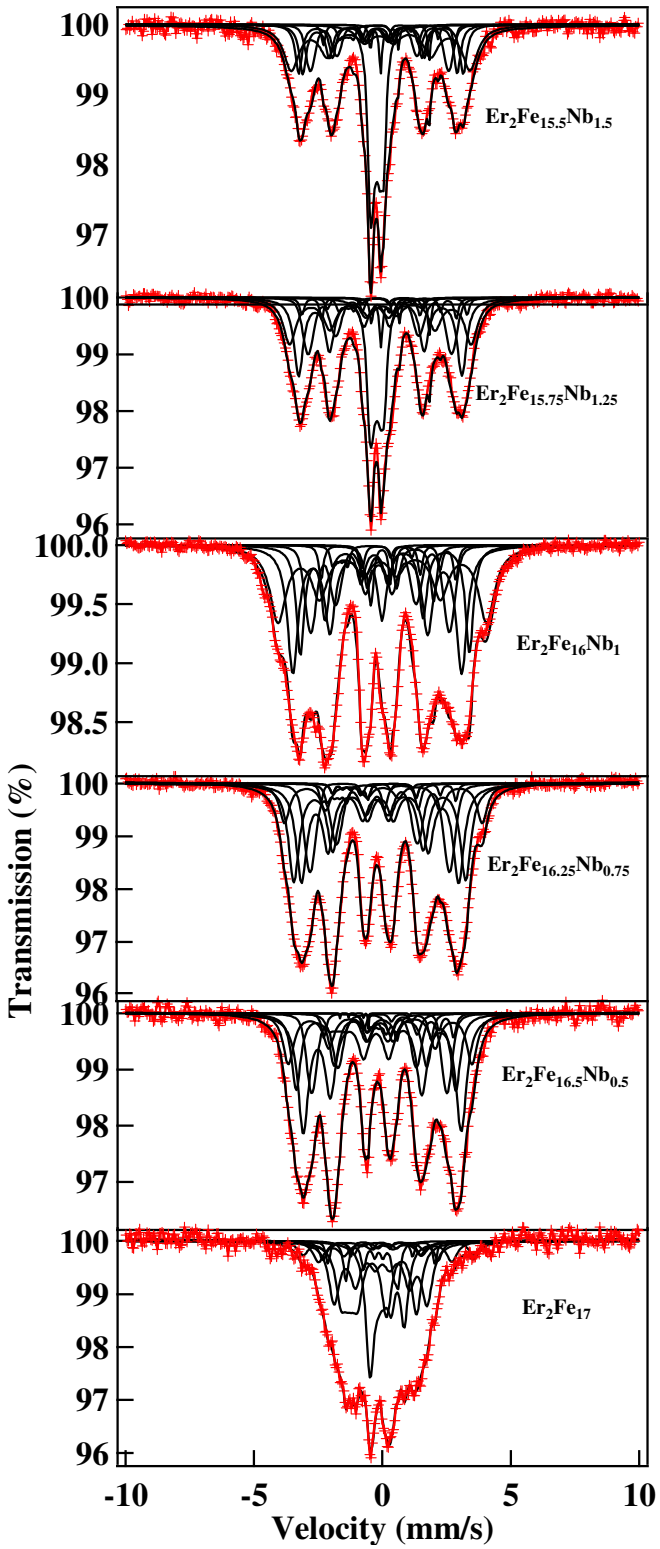

Figure 4.7a: Mössbauer spectra of $Er_2Fe_{17-x}Nb_x$ compounds at 300 K.

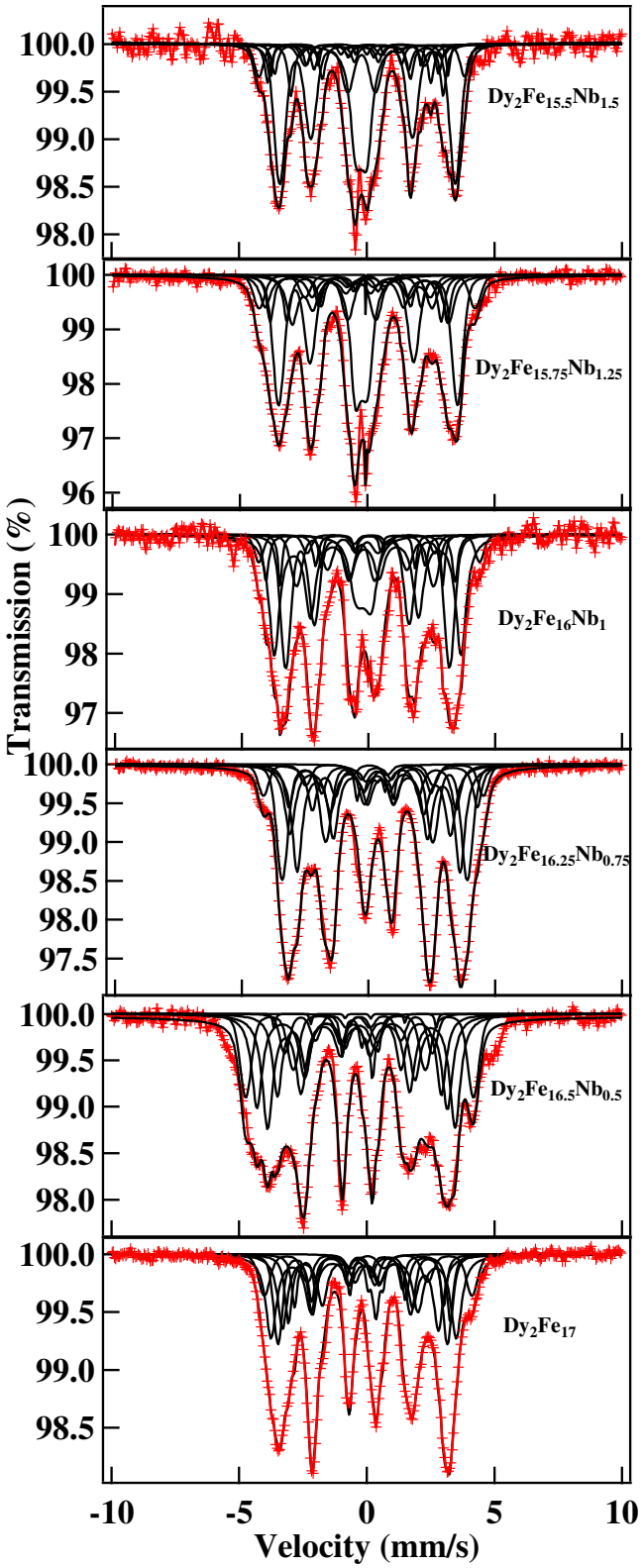

Figure 4.7b: Mössbauer spectra of $Dy_2Fe_{17-x}Nb_x$ compounds at 300 K.

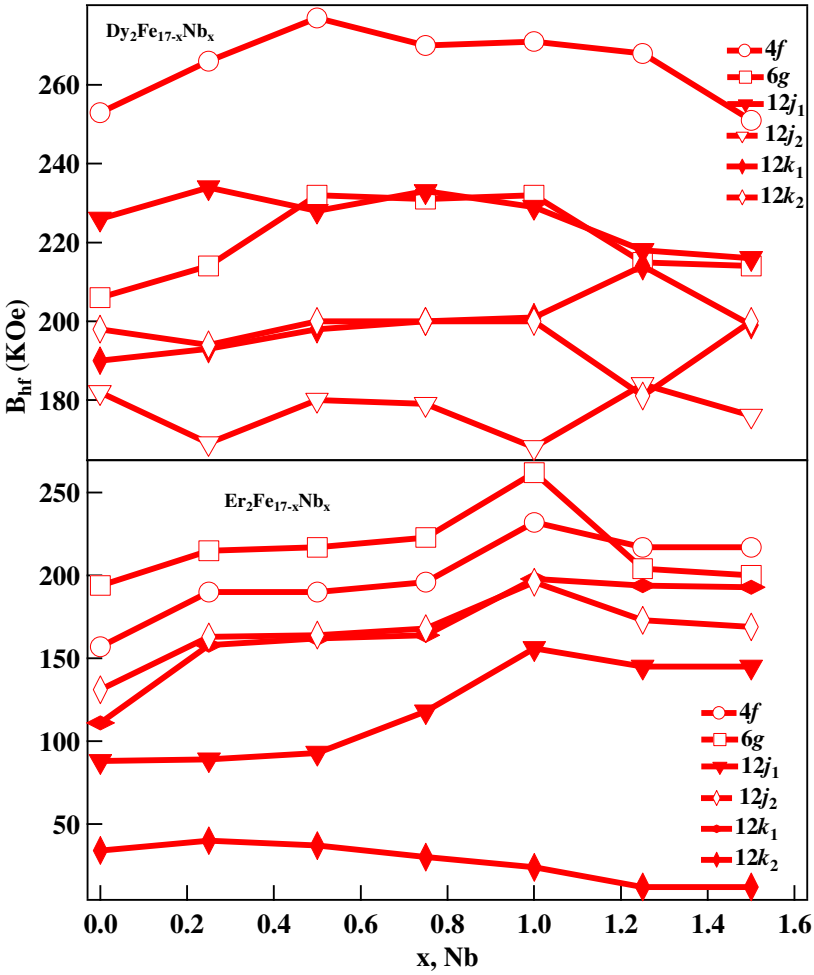

Figure 4.7c: Hyperfine field of $R_2Fe_{17-x}Nb_x$ compounds.

RT hyperfine field (B_{hf}) is shown in Fig. 4.7c. It was increased up to x = 1 and then decreased above x>1. This trend is identical with the trend of T_c in both set of samples (Er and Dy). This result is similar to that of $SmFe_{9-x}Co_xTi$ [71]. The enhancement of T_c and increased B_{hf} are related to the dumbbell Fe-Fe distances [72]. As discussed above, when Nb is substituted on Fe site, bigger Nb atoms caused expansion in the unit cell. This increases the strength of exchange interaction and hence increases T_c and B_{hf} up to x = 1. But beyond x = 1, magnetic moment of Fe dilutes faster and hence decreases T_c. It also leads to decrease in the hyperfine field. In Fig. 4.7a, $Er_2Fe_{15.5}Nb_{1.5}$

and $Er_2Fe_{15.75}Nb_{1.25}$ have quadruple doublet in the center of the spectra corresponding to $NbFe_2$ laves phase. This doublet was not observed lower concentration of the Nb up to x = 1. It is because the lower concentration of the Nb did not have impurities phases like $NbFe_2$ and RFe_3. It was also proven by XRD patterns. However, $Er_2Fe_{16}Nb_1$ sample had α-Fe impurity corresponding to a magnetic sextet with B_{hf} = 329 kOe is in close agreement with B_{hf} of α-Fe [73]. The observed hyperfine parameters of $NbFe_2$ and $ErFe_3$ phases also found match with published data [74, 75].

As like in the $Er_2Fe_{17-x}Nb_x$ samples, Mössbauer spectral analysis of $Dy_2Fe_{17-x}Nb_x$ samples were carried out with six sextets up to x = 0.75 and results are similar to $Er_2Fe_{17-x}Nb_x$ sample except higher value of B_{hf} than $Er_2Fe_{17-x}Nb_x$ samples. It further supports the superior T_c of Dy set of samples over Er set of samples. Laves $NbFe_2$ phase was observed in Mössbauer spectra and XRD of $Dy_2Fe_{16}Nb_1$ sample. The laves phase represented by doublet in the Mössbauer spectra has B_{hf} = 23 kOe and δ = -0.17 mm/s at RT. For x = 1.25 and x = 1.5 in $Dy_2Fe_{17-x}Nb_x$ samples, 2 additional sextets were added other than regular six sextets (4*f*, 6*g*, 12j_1, 12j_2, 12k_1, 12k_2). They are corresponds to $NbFe_2$ and $DyFe_3$ phases. The relative area intensity of $NbFe_2$ at higher concentration of Nb has increased though there is slight decrease in B_{hf} at higher concentration. This trend is similar to the trend of the $Er_2Fe_{17-x}Nb_x$ samples. The slight decrease in B_{hf}, may indicate that ferromagnetic $NbFe_2$ phase may be changing into paramagnetic $NbFe_2$ phase. To be clear, further investigation is to be done. The increased relative area intensity of $NbFe_2$ phase consistent with XRD inset of Dy set of samples. The hyperfine parameters of $NbFe_2$ and $DyFe_3$ phases found match with published data [74, 76].

Similarities and Differences between $Dy_2Fe_{17-x}Nb_x$ and $Er_2Fe_{17-x}Nb_x$ alloys

(a) Similarities:

(i) Pure R_2Fe_{17} phase was detected up to x = 0.75, Nb, in XRD of both set of samples.

(ii) One impurity phase (α-Fe for Er and $NbFe_2$ for Dy) was detected at x = 1 concentration of Nb in XRD of both set of samples.

(iii) Two impurities ($NbFe_2$ and RFe_3) were detected beyond x = 1, Nb, in XRD of each set of samples.

(iv) Magnetization of each set of samples were decreasing linearly up to x = 1, Nb.

(v) T_c and B_{hf} increased first and attained maximum at x = 1 and then decrease beyond x =1 in each set of samples.

(vi) Equal numbers of sextet were used to fit Mössbauer spectra for same concentration of Nb within two set of samples.

(vii) Paramagnetic $NbFe_2$ phase was observed in both set of samples (see Fig. 4.1 and 4.2).

(b) Differences:

(i) α-Fe detected in $Er_2Fe_{16}Nb_1$ whereas $NbFe_2$ detected in $Dy_2Fe_{16}Nb_1$ from XRD.

(ii) Larger decreased magnetization slope observed in $Er_2Fe_{17-x}Nb_x$ than $Dy_2Fe_{17-x}Nb_x$ between x = 1 to 1.25 concentration of Nb.

(iii) Larger T_c and B_{hf} obtained for $Dy_2Fe_{17-x}Nb_x$ than $Er_2Fe_{17-x}Nb_x$ set of samples.

(iv) Highest T_c = 460 K for $Dy_2Fe_{16}Nb_1$ and 410 K for $Er_2Fe_{16}Nb_1$ compound.

(v) The presence of doublet $NbFe_2$ phase was noticed (see in Fig. 4.2) in XRD & Mössbauer spectroscopy of $Dy_2Fe_{16}Nb_1$ which was absent in same concentration of $Er_2Fe_{16}Nb_1$ sample (see Fig. 4.2 (XRD) and 4.7 (Mössbauer)).

Structural analysis of $Dy_2Fe_{17-x}Cr_x$

Figure 4.8 shows the XRD patterns of $Dy_2Fe_{17-x}Cr_x$ alloys with various Cr concentrations. With the Cr substitution a gradual shift in the peaks to the right compared to that of pure Dy_2Fe_{17} is observed. The samples are in single phase up to x = 2.5 with Th_2Ni_{17} structure (space group, P63/mmc). However, additional phase of Dy_6Fe_{23} phase was observed at x = 3. This impurity shows that the maximum concentration for $Dy_2Fe_{17-x}Cr_x$ is x = 2.5. This maximum concentration (x = 2.5) is larger concentration than Nb (x = 0.75) concentration in $Dy_2Fe_{17-x}Nb_x$ alloys. As we know, Nb atom is bigger than Fe atom whereas the Cr atom is smaller than Fe atom. The observed difference in maximum concentration is coming from difference in ionic radii of Cr (0.60 Å) and Nb (0.86 Å) compared to that of Fe (0.63 Å). The lattice parameters 'a', 'c' and unit cell volume 'V' were calculated using equations (3) and (4). The trend of variation of the lattice parameters 'a' and 'c' of $Dy_2Fe_{17-x}Cr_x$ well agree with $Sm_2Fe_{17-x}Cr_x$ [77] and $Er_3Fe_{29-x}Cr_x$ [78]. The lattice parameter 'a' decreases as increasing the Cr concentration 'x' whereas the lattice parameter 'c' shows irregular trend (see Fig. 4.9) because of lattice deformation induced by Cr insertion. However, the linear decrease in unit cell volume (1.95 $Å^3$/Cr for $Dy_2Fe_{17-x}Cr_x$) of $Dy_2Fe_{17-x}Cr_x$ observed. This is resulting from

substitution of smaller Cr (0.60 Å) into bigger Fe (0.63 Å) atom. It further suggests that there is more influence of the lattice parameter 'a' than 'c' by Cr atom substitution.

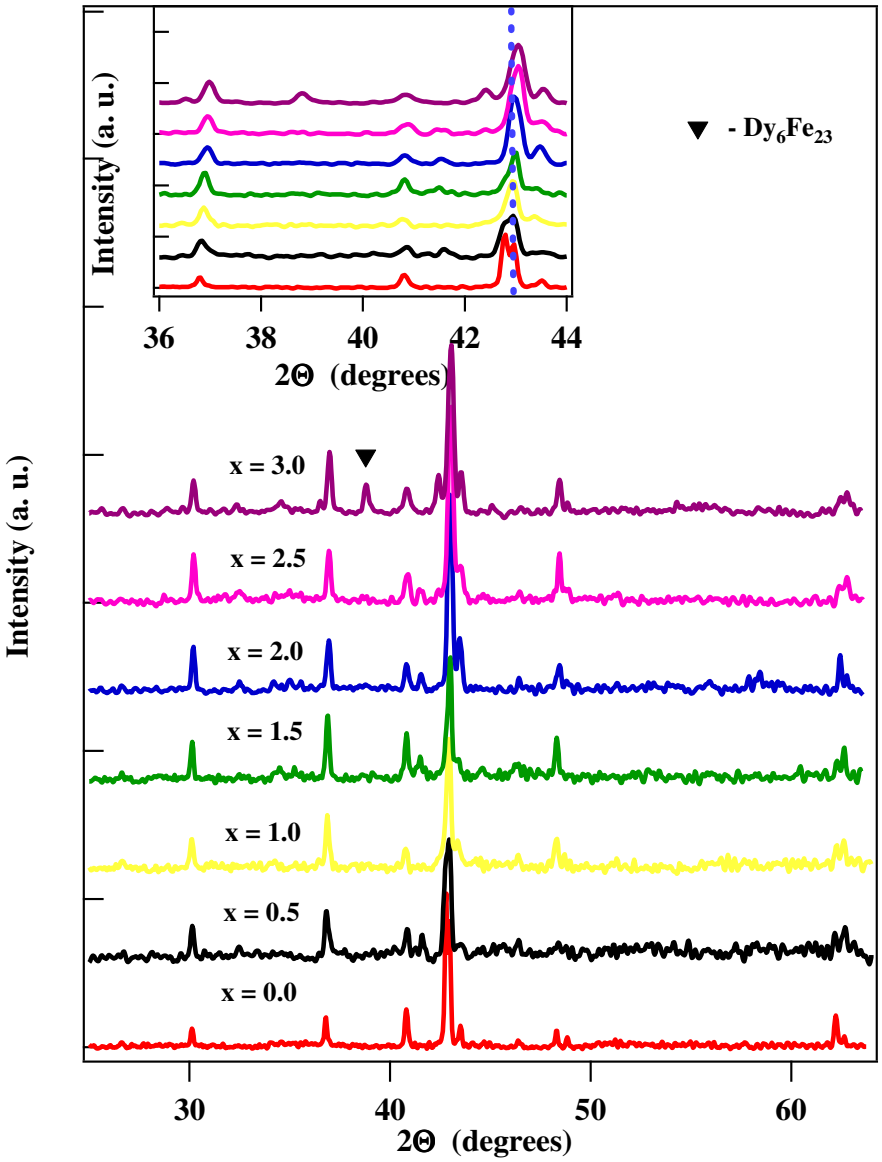

Figure 4.8: X-ray diffraction patterns of $Dy_2Fe_{17-x}Cr_x$ compounds.

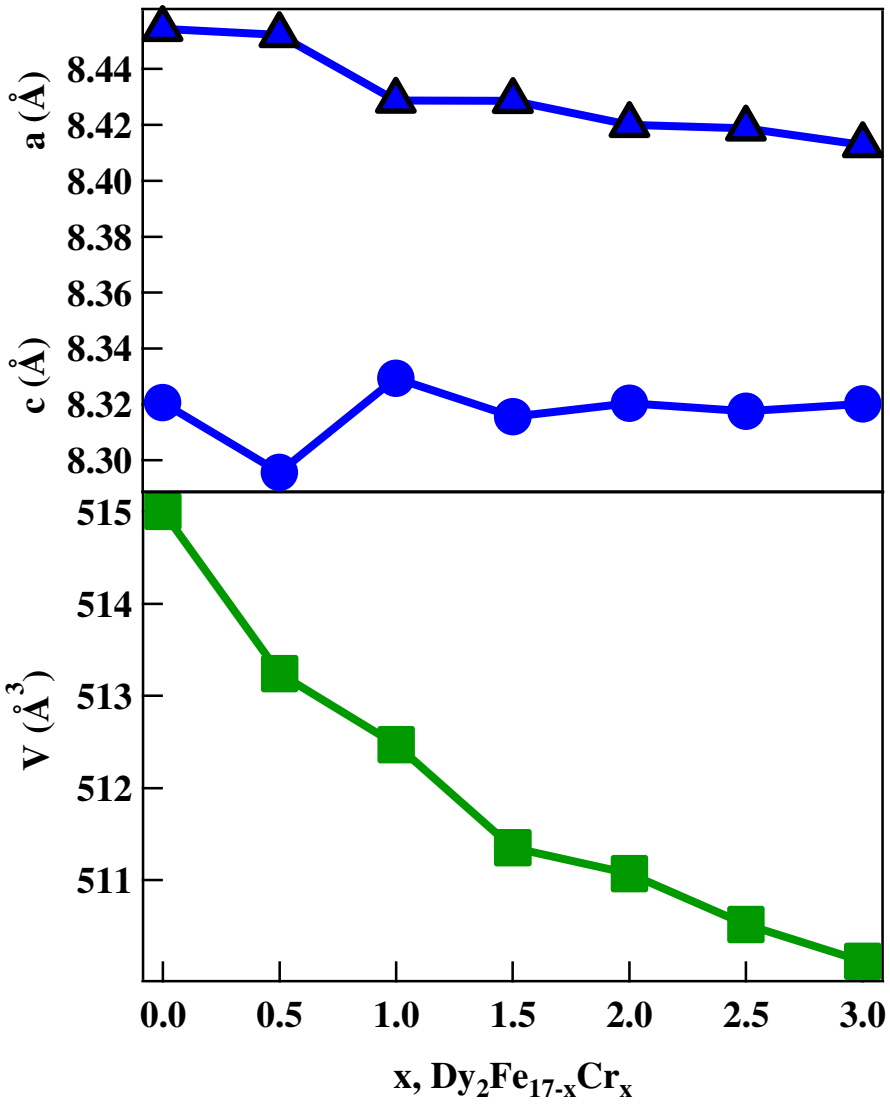

Figure 4.9: Lattice Parameters and unit cell volume of $Dy_2Fe_{17-x}Cr_x$ compounds.

Magnetic properties of $Dy_2Fe_{17-x}Cr_x$

The saturation magnetization of $Dy_2Fe_{17-x}Cr_x$ at 5 and 300 K is reported in the Table 5. Fig. 4.10a shows typical magnetization curve of $Dy_2Fe_{17-x}Cr_x$ at 300 K. Fig. 4.10b shows that the saturation magnetization of $Dy_2Fe_{17-x}Cr_x$ is decreasing linearly as increasing Cr concentration at 5 and 300 K. This result is close in agreement with the $Y_2Fe_{17-x}Cr_x$ [62], $Er_2Fe_{17-x}Al_x$ [79], $Er_3Fe_{29-x}Cr_x$ [78], $R_2Fe_{17-x}Al_xC$ [58]. The decrease in

magnetization again partly comes from decrease of magnetic moment of Fe atoms due to substitution of weak magnetic Cr atoms for Fe.

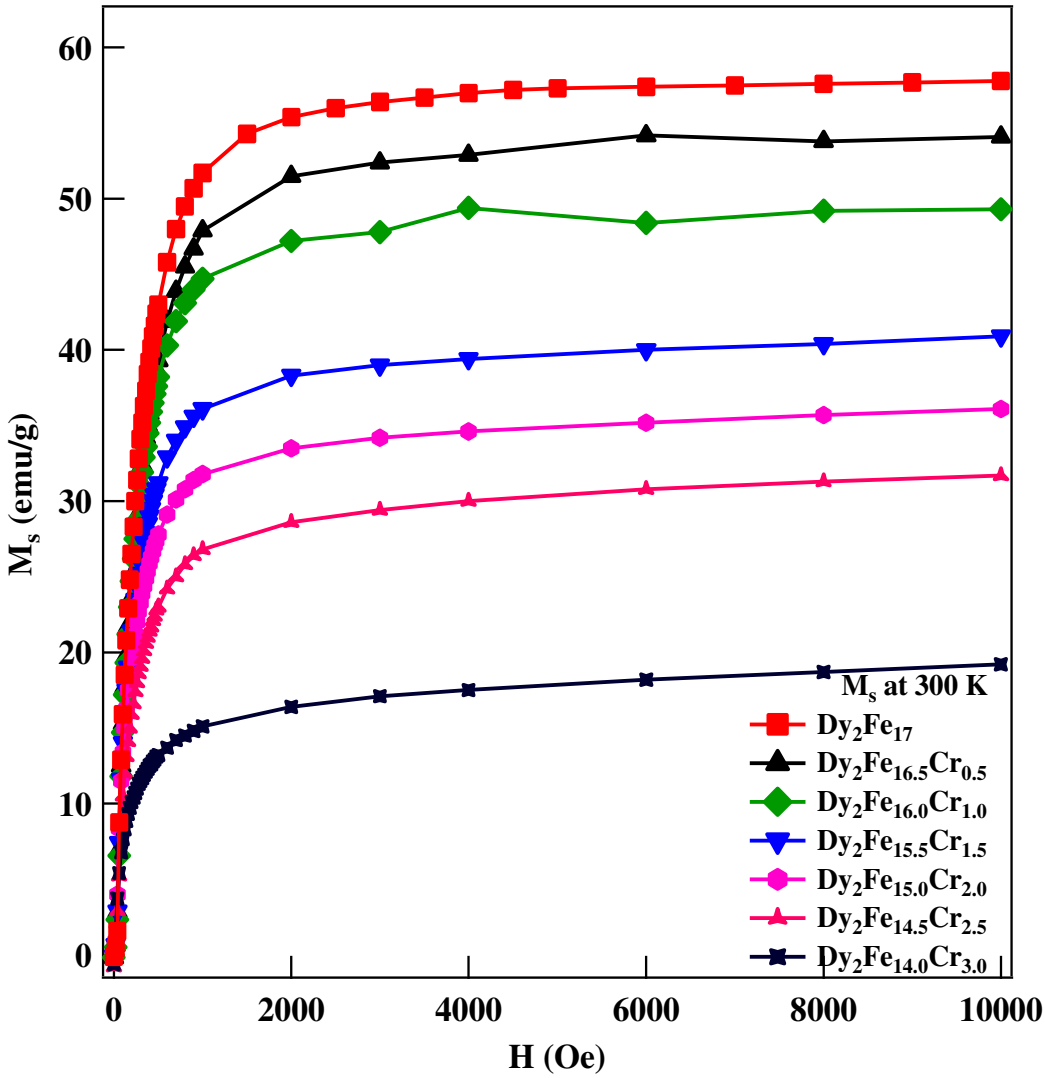

Figure 4.10a: Magnetization of $Dy_2Fe_{17-x}Cr_x$ compounds.

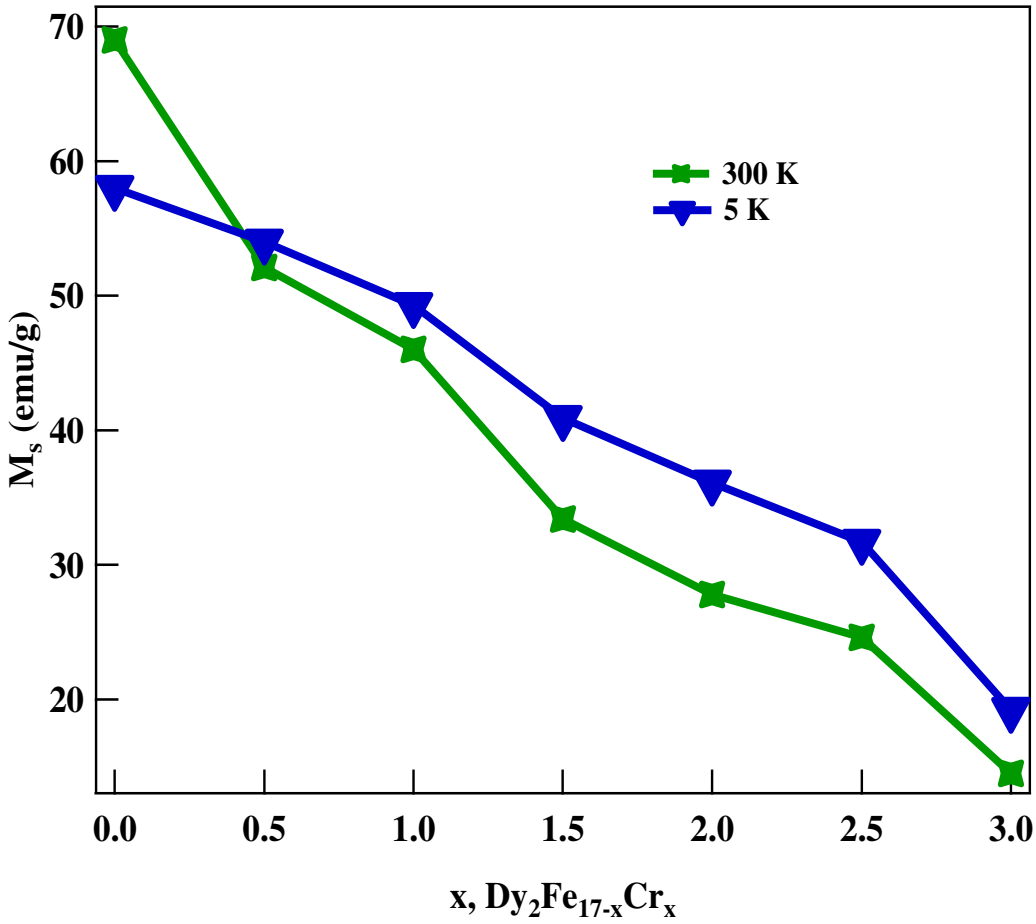

Figure 4.10b: Saturation magnetization of $Dy_2Fe_{17-x}Cr_x$ alloys at 5 K and 300K.

The great drop in saturation magnetization value observed after x = 2.5 due to the formation of extra Dy_6Fe_{23} phase. A similar result was observed in the $Dy_2Fe_{17-x}Nb_x$, $Er_2Fe_{17-x}Nb_x$ set of samples due to formation of extra phases RFe_3 and $NbFe_2$. Again, the abrupt drop M_s after x = 2.5 (Cr concentration) here is also coming from loss of Fe amount from R_2Fe_{17} phase. Furthermore, from Fig. 4.10b, it is observed that 5 K magnetization data is dropping down faster than 300 K data though RT M_s data is higher than 5 K data. It is known that heavy rare earth element (Dy) couple antiparallel with Fe moment leads to ferrimagnetism. Thus net magnetization of heavy rare earth compounds

is lesser than light rare earth compounds. As Bao-gen Shen et al. [38], the rate of cancellation of net moments is higher at low temperature comparative to RT and hence 5 K magnetization data is dropping faster than 300 K.

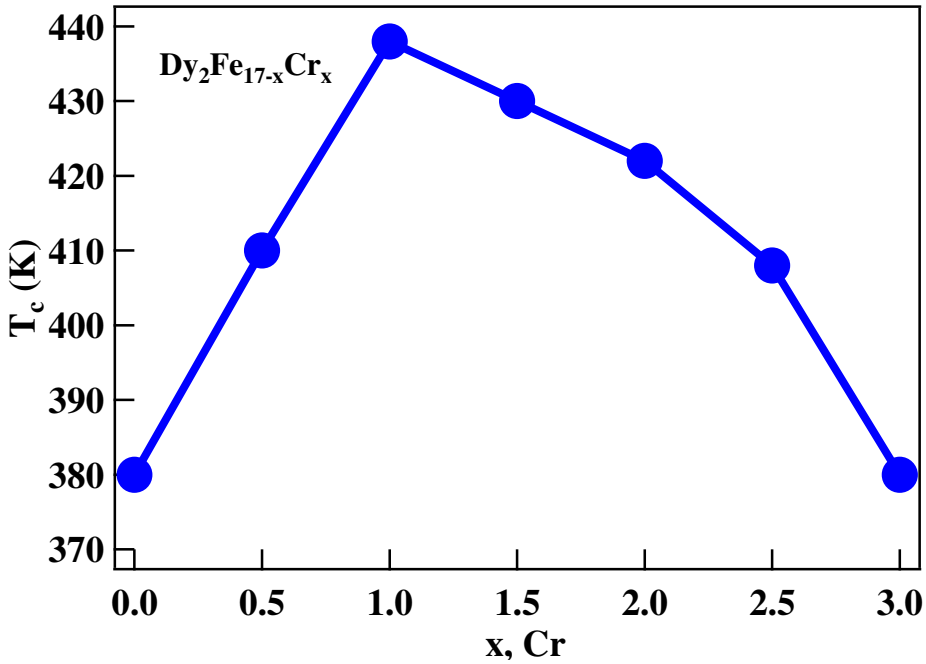

Figure 4.11: Curie temperature of $Dy_2Fe_{17-x}Cr_x$ alloys as function of Cr contents.

The T_c of the alloys is listed in the Table 5. The concentration dependence of T_c is shown in Fig. 4. 11, it was observed that T_c is increasing with Cr content x in $Dy_2Fe_{17-x}Cr_x$ up to x = 1. A similar behavior has also found for $R_2Fe_{17-x}Nb_x$ (R: Dy and Er), $Nd_2Fe_{17-x}Cr_x$ [80], $Y_2Fe_{17-x}Cr_x$ [62], $Sm_2Fe_{17-x}Mn_x$ [81]. The maximum in T_c ~ 442 K was observed for $Dy_2Fe_{16}Cr$ which is 60 K higher than that of Dy_2Fe_{17} alloy. According to the high resolution-neutron study of the $Y_2Fe_{15}Cr_2$ compound at 77 K, it was observed that 4f site had highest occupancy (0.5) compared to other sites 12*j* (0.12) and 6*g* (0.10) [62]. It

signifies that substitution of Cr atoms for Fe atoms on 4*f* sites may increase the total strength of exchange interaction decreasing the strength of antiferromagnetic interaction at 4*f* sites. This improvement of exchange interaction leads to increase T_c of the compounds up to x = 1. But T_c decreases at higher concentration (x > 1) Cr substitution on Fe site. It is because of the magnetic moment dilution and probably, due to low Cr-Cr and Cr-Fe exchange coupling [77]. Though, the decrease in magnetization and variation in T_c argument of $Dy_2Fe_{17-x}Cr_x$ is similar to that of $Dy_2Fe_{17-x}Nb_x$, the magnetization value and T_c of Nb substituted alloy has superiority over Cr substitution. This is because of expansion of unit cell by Nb substitution rather than contraction of unit cell by Cr substitution.

Mössbauer analysis of $Dy_2Fe_{17-x}Cr_x$

A Mössbauer spectrum of $Dy_2Fe_{17-x}Cr_x$ alloys at RT is shown in the Fig. 4.12a. This spectrum nature is very similar to that of [77]. Hyperfine parameters of $Dy_2Fe_{17-x}Cr_x$ alloys are given in Table 8. Six sextets (4*f*, 6*g*, 12j_1, 12j_2, 12k_1, 12k_2) for four in-equivalent iron sites used to study Mössbauer analysis of $Dy_2Fe_{17-x}Cr_x$ except x = 3. At x = 3, Dy_6Fe_{23} phase was detected in XRD other than Dy_2Fe_{17} phase. It can be observed from Fig. 4.12a that the resolution of the spectra decreases as increasing Cr concentration in $Dy_2Fe_{17-x}Cr_x$ samples. Decreased resolution in the spectra is coming from the Cr substitution. It brings disorder in the alloys. Furthermore, it has been observed that outer peaks are disappearing and inner peaks are merging at higher concentration which is consistent with decrease of the hyperfine field intensity. Consequently, it results in spectral broadening [77].

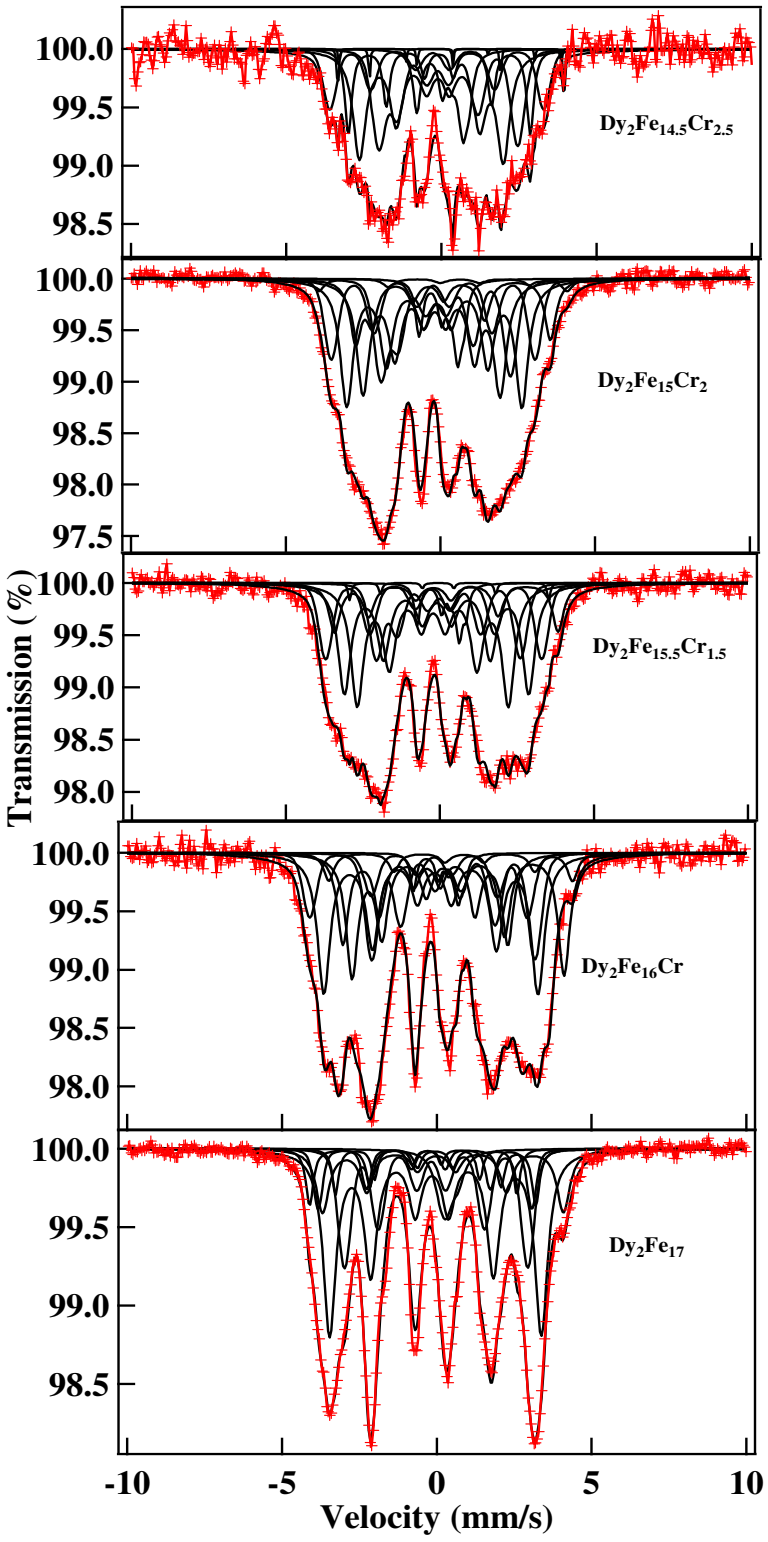

Figure 4.12a: Mössbauer spectra of $Dy_2Fe_{17-x}Cr_x$ compounds at 300 K.

Table 8: Mössbauer parameters of $Dy_2Fe_{17-x}Cr_x$ compounds.

Hyperfine Field (B_{hf})	**x**	***4f***	***6g***	***12j₁***	***12j₂***	***12k₁***	***12k₂***
Dy_2Fe_{17}	0.0	221	239	200	158	160	205
$Dy_2Fe_{16}Cr_1$	1.0	223	238	199	156	158	203
$Dy_2Fe_{15.5}Cr_{1.5}$	1.5	233	196	200	151	151	205
$Dy_2Fe_{15}Cr_2$	2.0	239	183	198	139	143	205
$Dy_2Fe_{14.5}Cr_{2.5}$	2.5	236	183	227	140	144	213
Isomer Shift (δ)		***4f***	***6g***	***12j₁***	***12j₂***	***12k₁***	***12k₂***
Dy_2Fe_{17}	0.0	0.009	-0.194	-0.092	-0.092	-0.205	-0.205
$Dy_2Fe_{16}Cr_1$	1.0	-0.007	-0.203	-0.090	-0.090	-0.239	-0.239
$Dy_2Fe_{15.5}Cr_{1.5}$	1.5	0.525	-0.148	-0.034	-0.034	-0.306	-0.306
$Dy_2Fe_{15}Cr_2$	2.0	0.389	-0.143	0.062	0.062	-0.303	-0.303
$Dy_2Fe_{14.5}Cr_{2.5}$	2.5	0.577	-0.066	0.029	0.029	-0.193	-0.193
Quadruple Splitting (ΔE_Q)		***4f***	***6g***	***12j₁***	***12j₂***	***12k₁***	***12k₂***
Dy_2Fe_{17}	0.0	0.353	-0.099	0.334	0.415	-0.091	-0.277
$Dy_2Fe_{16}Cr_1$	1.0	0.314	-0.123	0.297	0.317	0.073	-0.305
$Dy_2Fe_{15.5}Cr_{1.5}$	1.5	0.800	-0.164	0.432	0.162	-0.053	-0.491
$Dy_2Fe_{15}Cr_2$	2.0	-0.754	-0.109	0.425	0.197	-0.033	0.163
$Dy_2Fe_{14.5}Cr_{2.5}$	2.5	-0.800	0.014	0.555	0.393	-0.247	0.153

RT B_{hf} decreased with increasing Cr concentration & abrupt drop in 6*f* site B_{hf} was observed. This result is similar to that of $Er_2Fe_{17-x}Si_x$ [40]. This decrease results from the decreased magnetic exchange interaction resulting from Cr atoms substitution. It is also in agreement with the magnetization data (see Table 8). As Hao et al. [62], Cr atom substitutes more Fe from 4*f* site and hence big drop in B_{hf} was observed at 4*f* site (see Fig. 4.12b).

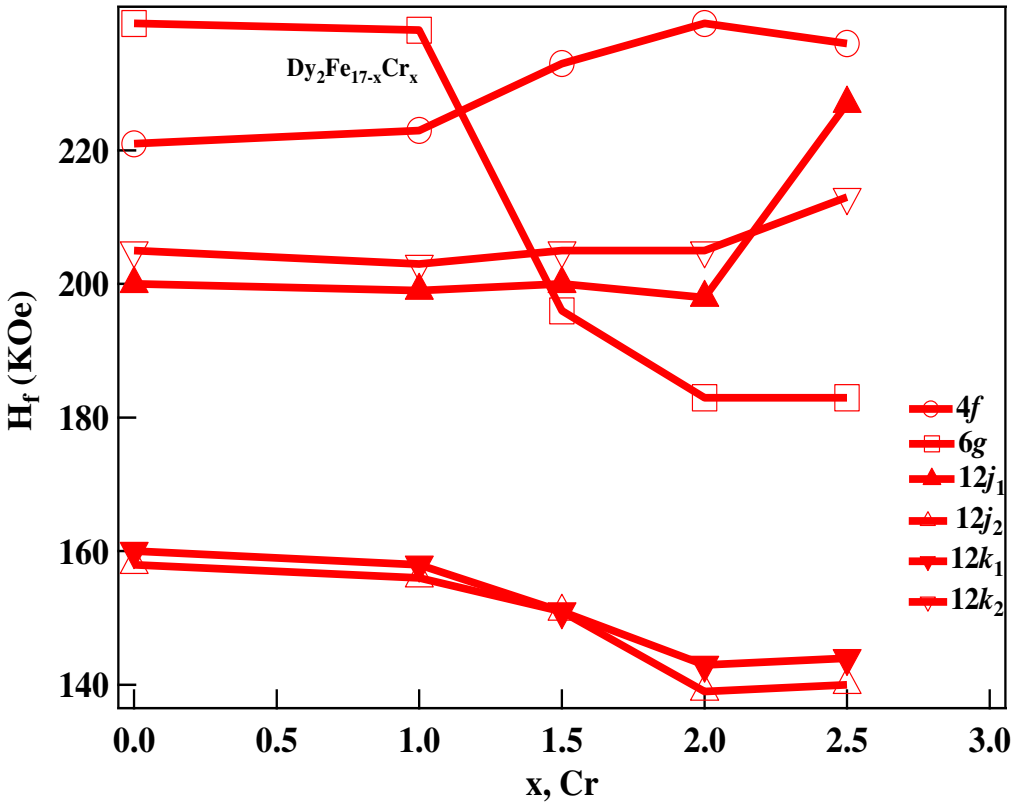

Figure 4.12b: Hyperfine field of $Dy_2Fe_{17-x}Cr_x$ compounds.

5. Part b. Results and Discussions

Structural analysis of $R_2Fe_{16}Nb_1$ (R: Dy, Er and Gd)

Figure 5.1 shows the XRD patterns of the $R_2Fe_{16}Nb$ alloy with a function of BM time. The starting material has Th_2Ni_{17}-type structure (space group, P63/mmc) with a small amount of Fe or $NbFe_2$ phase. XRD had not detected any other oxide impurities peak other than starting material peaks. As the BM time increase, the peak intensity of 2:17 phase and $NbFe_2$ phase were diminishing whereas the nanocrystalline peak intensity of α-Fe was sharpening as shown in the Fig. 5.1. From Fig. 5.1a, 5.1b, and 5.1c, we observed that reflection intensity from α-Fe is higher for heavier rare earths (Dy and Er) than light rare earth alloy (Gd). This indicates that less α-Fe contains in the mixture of alloyed $Gd_2Fe_{16}Nb$ powder compared to $Dy_2Fe_{16}Nb$ & $Er_2Fe_{16}Nb$ powders. The diminishing peak intensity of 2:17 phase indicates that the crystalline phase is transferring into the amorphous phase [49]. The diffraction peaks are broadening gradually with milling time, it could either come from reduction of crystallize size or from microscosmic stress arising from defects [82].

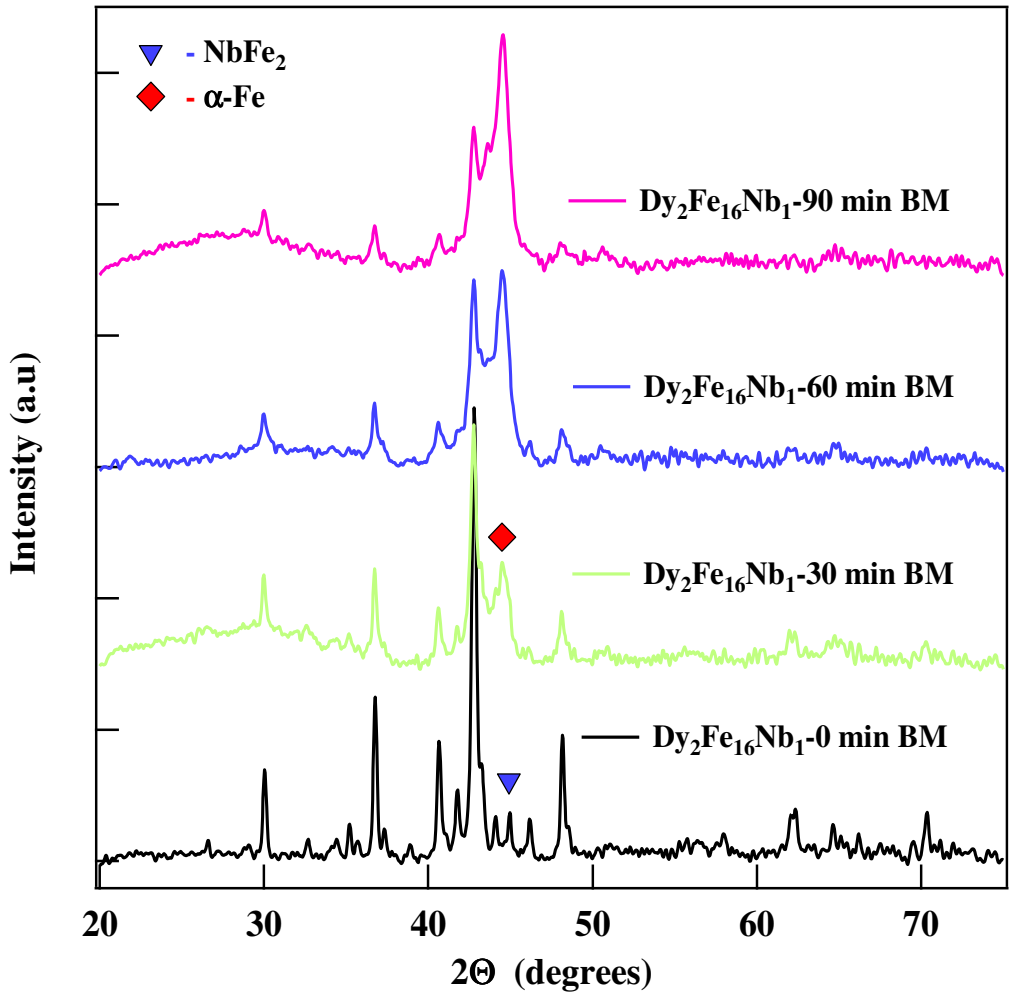

Figure 5.1a: X-ray Diffraction pattern of ball milled $Dy_2Fe_{16}Nb_1$ alloy.

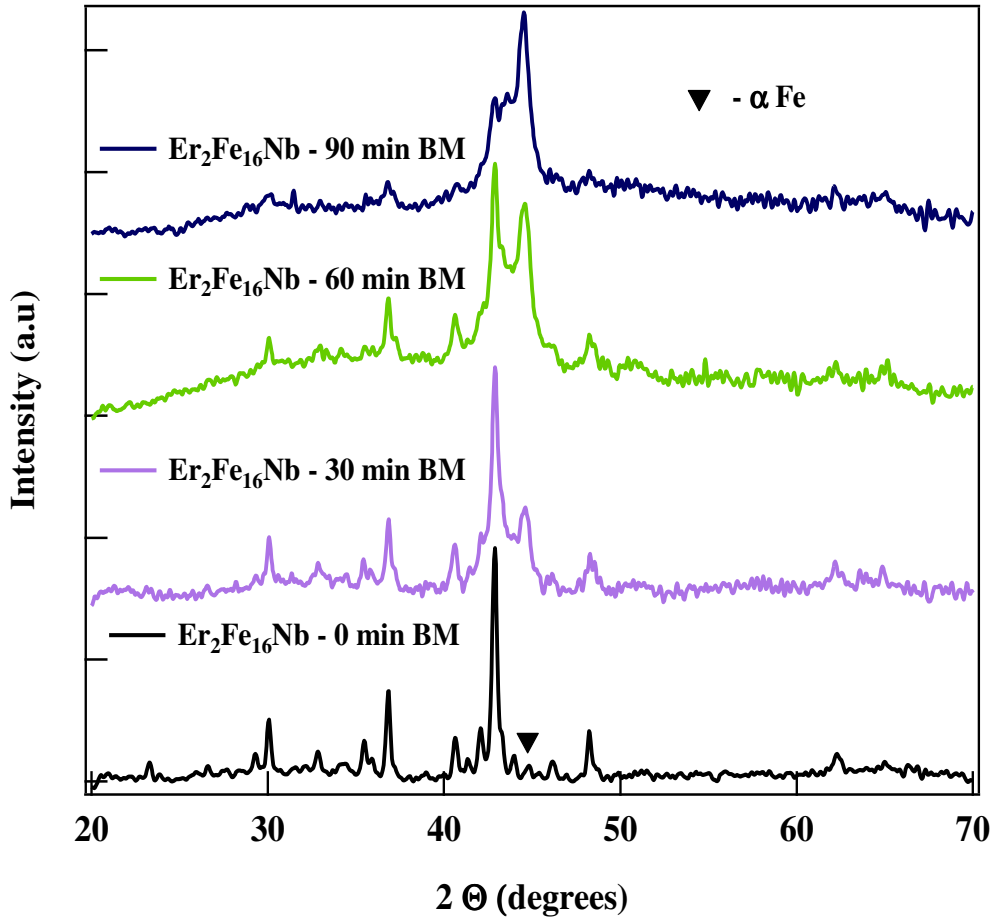

Figure 5.1b: X-ray Diffraction pattern of ball milled $Er_2Fe_{16}Nb_1$ alloy.

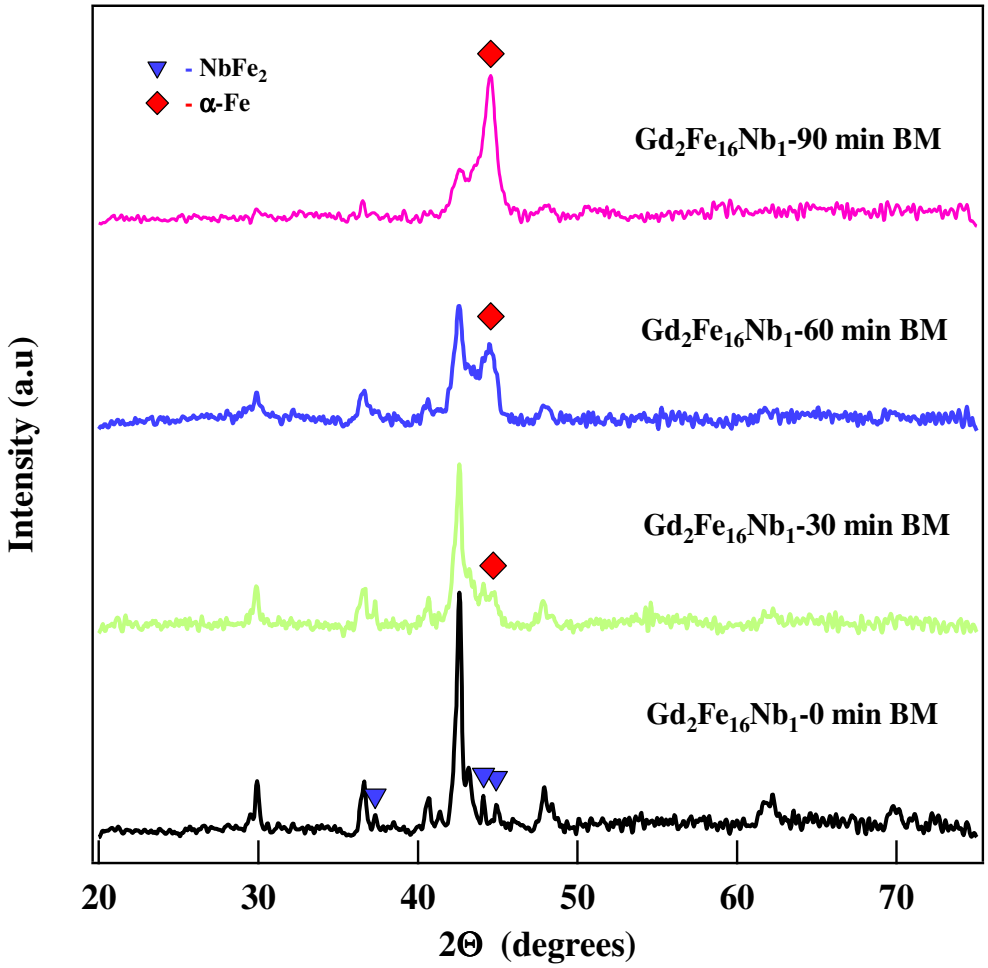

Figure 5.1c: X-ray Diffraction pattern of ball milled $Gd_2Fe_{16}Nb_1$ alloy.

Fig. 5.2 shows the structural parameters viz. crystal lattice *a* and *c*, as a function of *x*. The lattice constants are calculated using equations (3) and (4).The calculated lattice constants obtained from XRD patterns of the alloys are listed in the Table IX. In Fig. 5.2a and 5.2c, a linear expansion of unit cell volume observed as a function of BM time. This result contradicts with that of Sm_2Fe_{17} [29]. But the observed result consistent with diminish peak of $NbFe_2$ phase as the function of BM in XRD patterns. As the nature of ball milling, it produces different kinds of defects and do microstructural refinement in the alloys. In our understanding, the presence of defects and refinement enhances the

diffusivity of Nb (of $NbFe_2$ phase) into 2:17 phase. This diffusion causes the linear increase in the volume of the unit cell. On the other hand, it was observed from XRD that the peak intensity of α-Fe was sharpening. This sharpening in α-Fe peak is contributing from isolated α-Fe from $NbFe_2$ phase. But in case of $Er_2Fe_{16}Nb$ sample, neither the expansion of c-axis nor the expansion of unit cell volume was observed which contradicts $R_2Fe_{16}Nb$ (R: Dy and Gd) results. In our perspective, this difference is observed because of $NbFe_2$ phase. This α-Fe which was present in Dy and Gd samples but it was absent in Er set of samples. As discussed above, ball milling creates defect and do refinement which bring enhancement in the diffusivity of separated Nb (from $NbFe_2$) in to 2:17 phase and hence expansion in the unit cell volume is observed.

Table 9: Lattice parameters and unit cell volume of $R_2Fe_{16}Nb_1$ compounds.

	$Dy_2Fe_{16}Nb$			**$Er_2Fe_{16}Nb$**			**$Gd_2Fe_{16}Nb$**		
X	a, (Å)	c, (Å)	V, (Å^3)	a, (Å)	c, (Å)	V, (Å^3)	a, (Å)	c, (Å)	V, (Å^3)
0	8.46138	8.37182	519.063	8.44219	8.39138	517.91	8.49055	8.45539	527.86
30	8.46488	8.38072	520.045	8.43921	8.36519	515.94	8.47434	8.50623	529.01
60	8.46727	8.39929	521.492	8.43841	8.37365	516.36	8.48164	8.50314	529.63
90	8.46609	8.41583	522.373	8.44296	8.37750	517.15	8.51989	8.36760	526.00

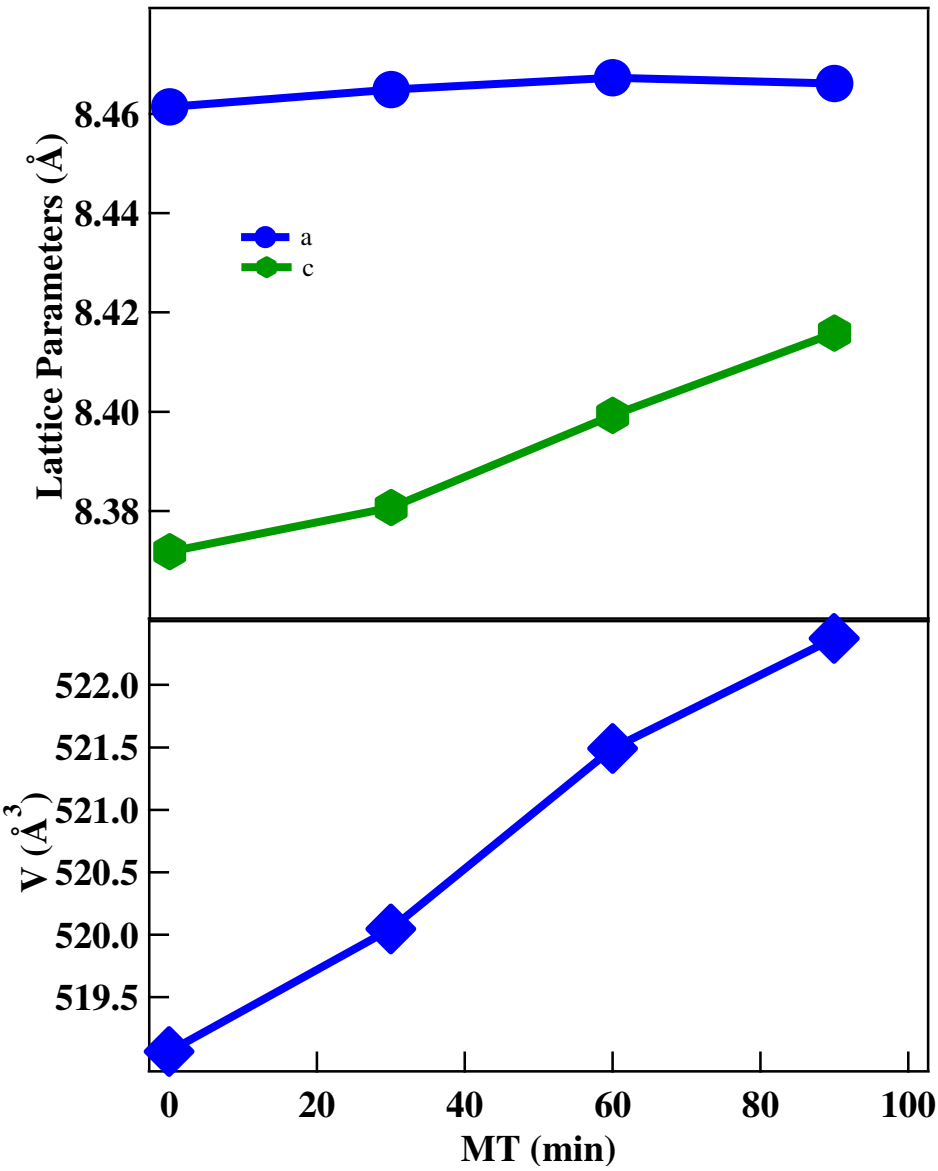

Figure 5.2a: Lattice parameters and unit cell volume of ball milled $Dy_2Fe_{16}Nb_1$ alloy.

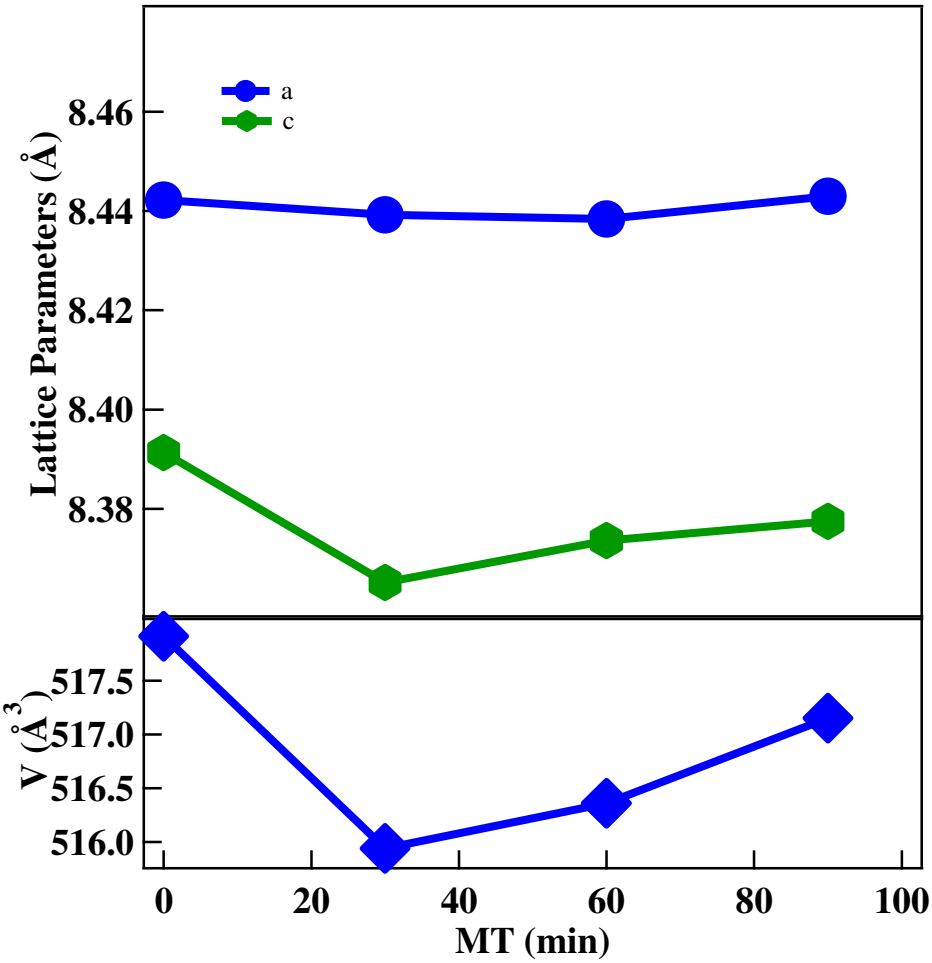

Figure 5.2b: Lattice parameters and unit cell volume of ball milled $Er_2Fe_{16}Nb_1$ alloy.

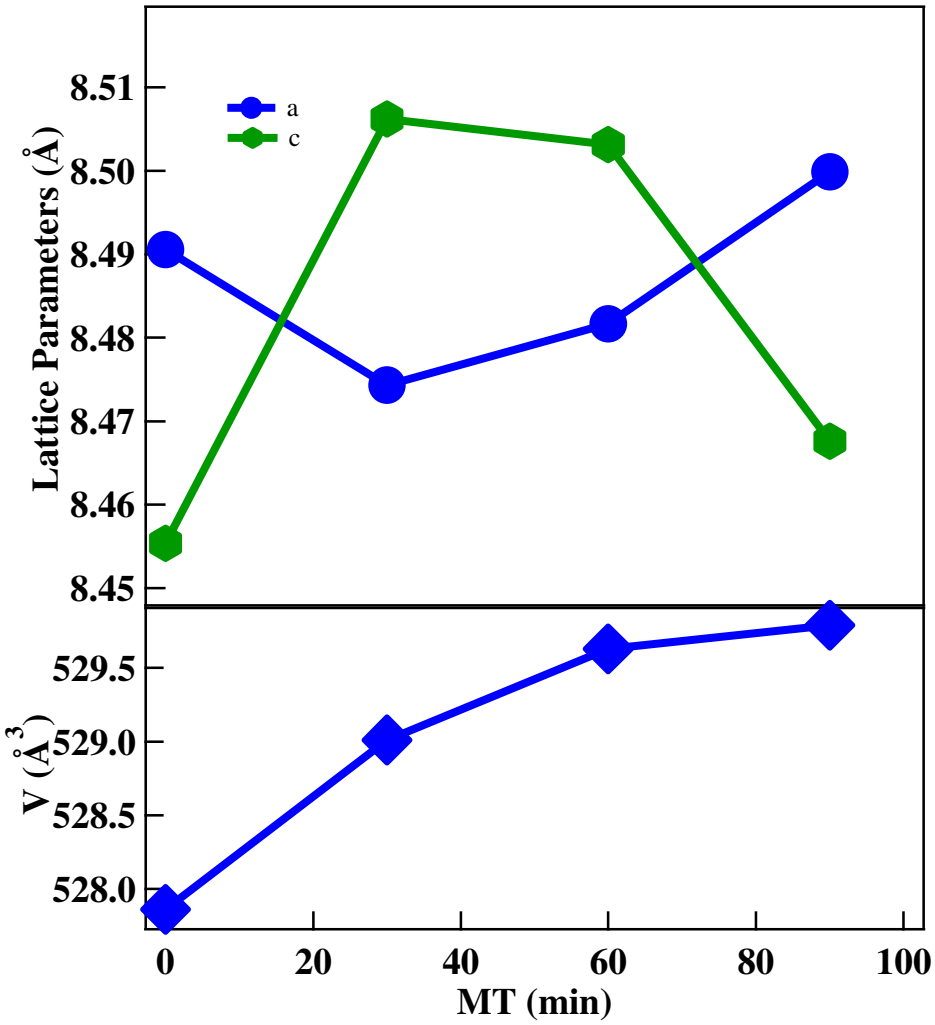

Figure 5.2c: Lattice parameters and unit cell volume of ball milled $Gd_2Fe_{16}Nb_1$ alloy.

Magnetic properties analysis of $R_2Fe_{17-x}Nb_x$ (R: Dy, Er and Gd)

The magnetic parameters of set of $R_2Fe_{16}Nb$ at 80 and 300 K are listed in the Table 10. Fig. 5.3 is comparative 2nd quadrant of the hysteresis loop of 0 min and 30 min BM. It shows that there is increment in the coercivity as well as remanence. This is because of exchange spring behavior between nanocrystalline $R_2Fe_{16}Nb$ and nanocrystalline α-Fe during 30 min BM [71].

Table10: Magnetic Properties of $R_2Fe_{16}Nb_1$ compounds.

	$Dy_2Fe_{16}Nb_1$					$Er_2Fe_{16}Nb_1$					$Gd_2Fe_{16}Nb_1$				
		80 K		300 K			80 K		300 K			80 K		300 K	
MT (min)	T_c K	M_s (emu/g)	H_c (Oe)	M_s (emu/g)	H_c (Oe)	T_c K	M_s (emu/g)	H_c (Oe)	M_s (emu/g)	H_c (Oe)	T_c K	M_s (emu/g)	H_c (Oe)	M_s (emu/g)	H_c (Oe)
0	442	56	205	205	94	410	53	126	50	44	510	88	170	62	200
30	515	72	917	917	193	485	72	194	66	120	520	90	180	66	228
60	497	82	369	369	168	482	105	178	67	112	530	116	168	81	195
90	493	110	244	244	157	480	82	157	80	129	550	145	166	81	174

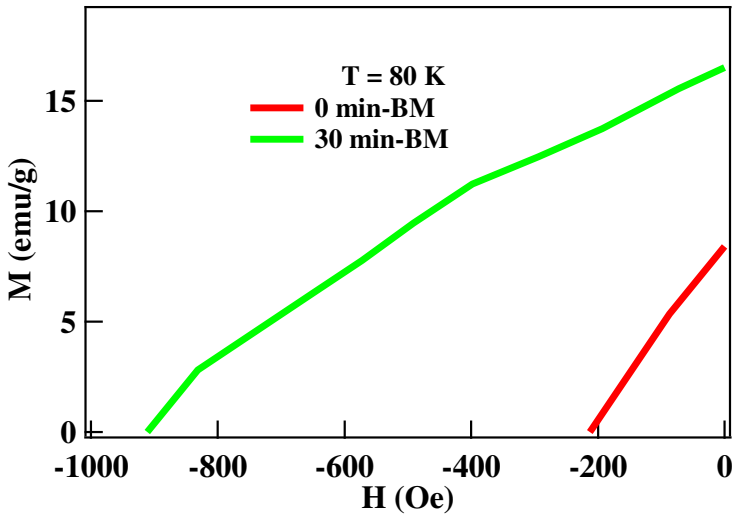

Figure 5.3a: 2nd quadrant of magnetization Vs field of ball milled $Dy_2Fe_{16}Nb_1$ alloy.

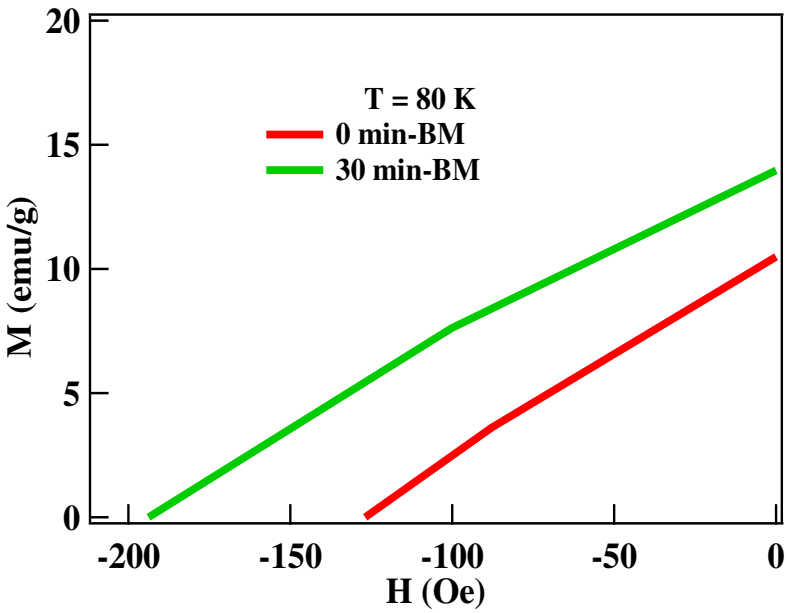

Figure 5.3b: 2nd quadrant of magnetization Vs applied field of ball milled $Er_2Fe_{16}Nb_1$ alloy.

Figure 5.4 shows coercivity data for $R_2Fe_{16}Nb$ alloy as function of BM time. The jump in the coercivity during 30 min BM is partly (i) emerging from exchange spring behavior between the two crystalline phases namely $R_2Fe_{16}Nb$ and α-Fe, and (ii) nanometer dimension grain refinement caused by the continued impact of grinding balls on samples [29, 49, 51].

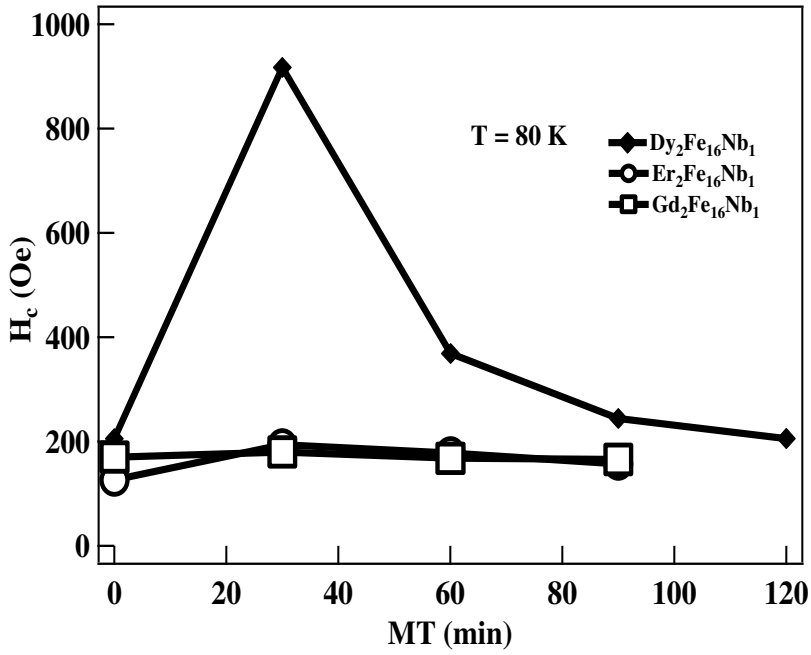

Figure 5.4: Comparative plot of coercivity of $R_2Fe_{16}Nb_1$ alloy (R: Dy, Er & Gd).

Generally, HEBM process has two opposite nature. First, the particles break into fine particles because of internal strain caused by applied pressure. Second, the finely divided particles tend to agglomerate in order to minimize their surface energy. The improvement in the magnetic properties we expected that it was coming from the refinement of alloys upon ball milling. Further study need to understand this interesting phenomenon. But the coercivity of the BM samples decrease for longer hours of milling time (MT), this is because of (i) slow phase transformation of crystalline 2:17 phase into its amorphous phase (ii) agglomeration of the nanoparticles after long hours of ball milling and (iii) increment of α-Fe content [83].

Increment in the remanence (see Table X) of milled powder compared to not mill powder consistent with [3]. The exchange spring phenomena by HEBM is more

pronounced in the $Dy_2Fe_{16}Nb$ compared to $R_2Fe_{16}Nb$ (R: Er and Gd) samples. The M_s data at 300 K) are plotted in the Fig. 5.5.

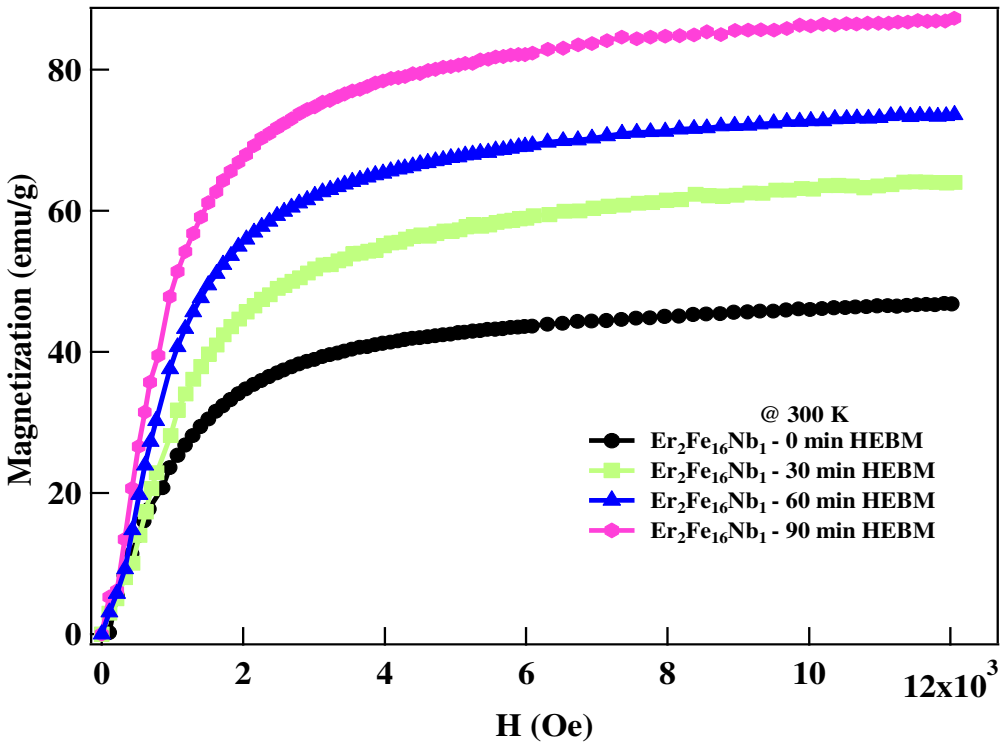

Figure 5.5a: Magnetization curve of $Er_2Fe_{16}Nb_1$ alloy at 300 K.

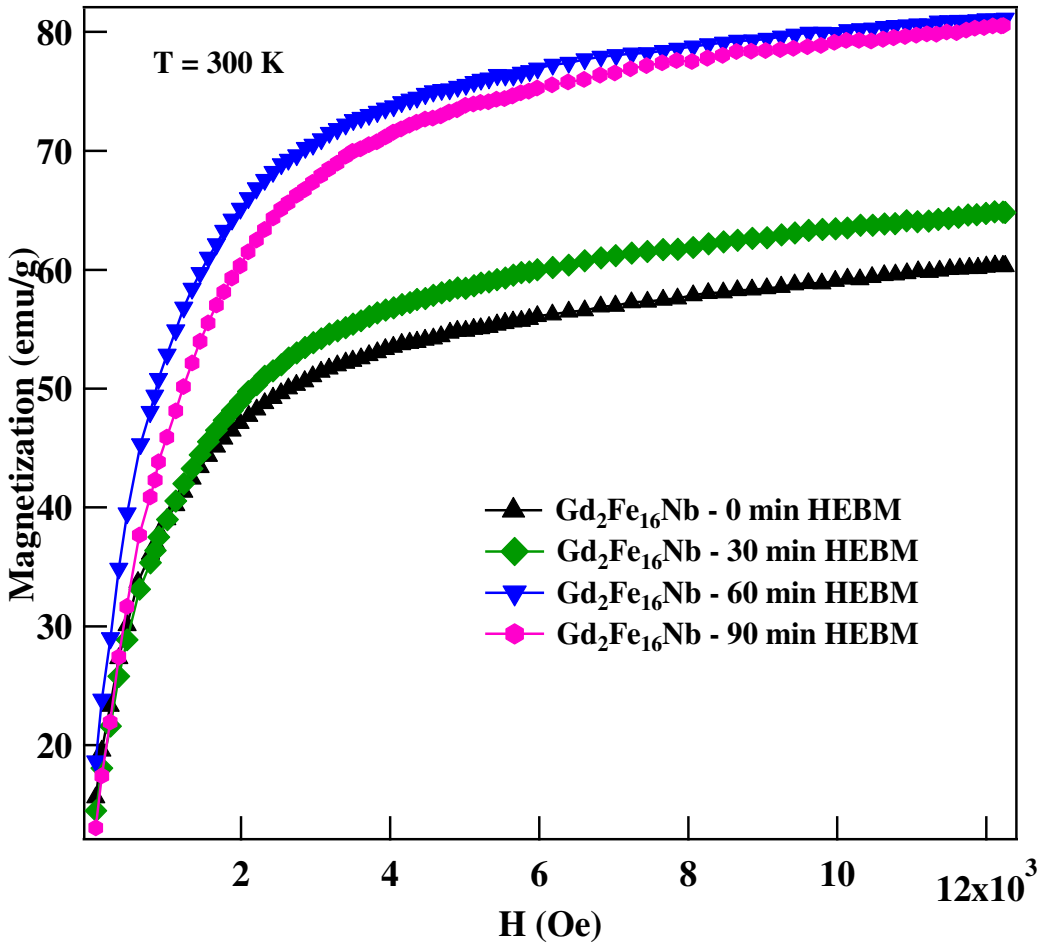

Figure 5.5b: Magnetization curve of $Gd_2Fe_{16}Nb_1$ alloy at 300 K.

The plots show that the M_s increases as the BM time increase. This result is consistent with sharpening peak of nanocrystalline α-Fe as the BM time increases. The increase in M_s is partly coming from lattice expansion and partly coming from increase in α-Fe amount during BM. The trend of lattice parameters expansion and increase in the M_s in Dy and Gd samples are in agreement with the Zhou et. al [84] whereas the increment in magnetization of Er samples is solely coming from addition of α-Fe amount in alloy.

The T_c of milled alloys is listed in the Table 10. The milled alloys have high T_c which is contributing partly from insertion of Nb atoms into 2:17 phase or from disorder induced by HEBM. The maximum in T_c ~ 515 K was observed for 30 min BM $Dy_2Fe_{16}Nb$ which is ~ 150 K higher value than the Dy_2Fe_{17} alloy [61]. Similarly, T_c = 485 K for 30 min BM $Er_2Fe_{16}Nb$ and T_c = 550 K for 90 min BM $Gd_2Fe_{16}Nb$. Again, introduction of Nb (from $NbFe_2$) in dumbbell Fe-Fe site cause increment in the Fe-Fe distances which improve the strength of exchange interaction, eventually brings improvement in the T_c. The defects induced by HEBM process also bring improvement in the T_c of the milled alloy. Hence, disordering improve T_c and improvement in magnetic exchange coupling either by introduction of Nb or by subtle change of the electronic environment around them. But at higher BM time, the introduction of Nb atom in 2:17 phase compensate with dilution of magnetic moment of Fe in 2:17 phase. Hence, it does not cause much variation in the T_c (see in the Fig. 5.6). The observed T_c ~ 550 K is superior to any series (R_2Fe_{17} intermetallic) of rare-earth transition metal-rich intermetallic compounds [34]. As in first part of thesis, the T_c of Dy samples corresponding to BM hours are superior than Er set of samples.

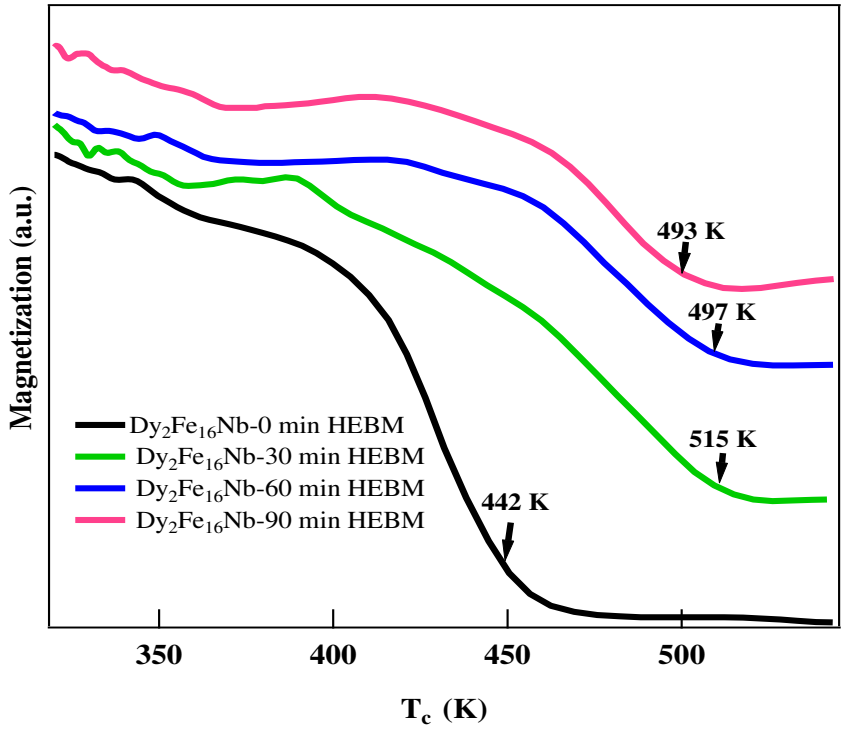

Figure 5.6a: Magnetization Vs temperature curve for T_c of $Dy_2Fe_{16}Nb_1$ alloy.

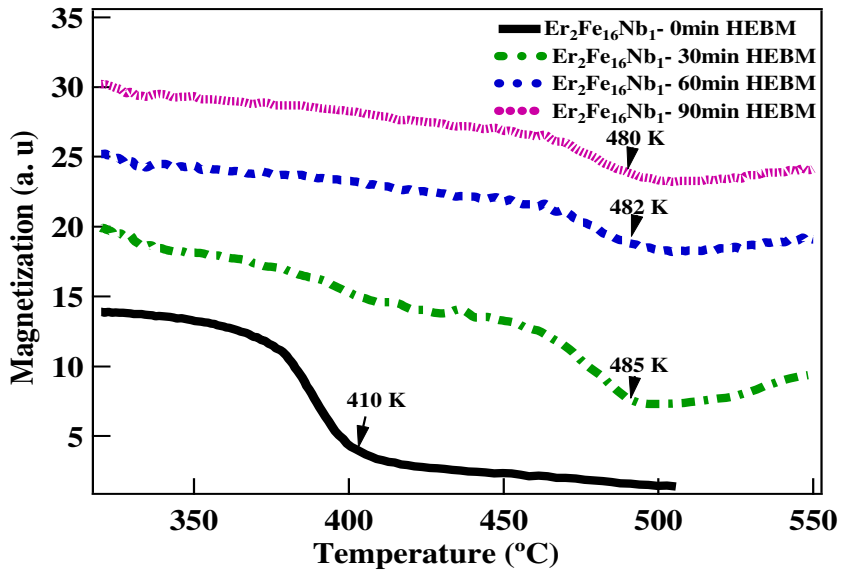

Figure 5.6b: Magnetization Vs temperature curve for T_c of $Er_2Fe_{16}Nb_1$ alloy.

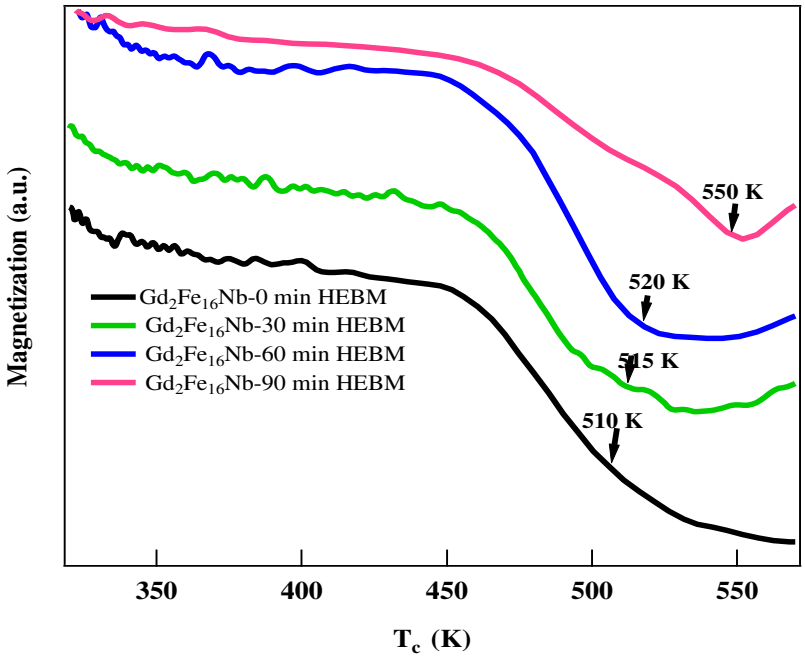

Figure 5.6c: Magnetization Vs temperature curve for T_c of $Gd_2Fe_{16}Nb_1$ alloy.

Mössbauer Spectra analysis of $R_2Fe_{16}Nb_1$

Mössabuer spectra of $R_2Fe_{16}Nb$ alloys ball milled at different time have measured at 300 K. Hyperfine parameters of as milled $R_2Fe_{16}Nb$ alloys are given in Table 11, 12, X13. Generally, for four in-equivalent iron sites of R_2Fe_{17} phase fit with six sextets 4*f*, 6*g*, 12j_1, 12j_2, 12k_1, 12k_2 for heavy rare earth and 6*c*, 9d_1, 9d_2, 18h_1, 18$h_2$18f_1, 18f_2 for light rare earth intermetallic. But in our present studies, additional phases were observed in the starting sample. So, higher numbers of sextets (7 or 8 or 9) were assigned for Mössbauer spectral analysis.

Table11: Mössbauer parameters of ball milled $Dy_2Fe_{16}Nb_1$ compounds.

Hyperfine Field (B_{hf})	**MT**	**4*f***	**Fe**	**6*g***	**12j_1**	**12j_2**	**12k_1**	**12k_2**
$Dy_2Fe_{16}Nb_1$ – 0 min	0	268		214	218	177	198	179
$Dy_2Fe_{16}Nb_1$ – 30 min	30	269	311	221	224	174	201	193
$Dy_2Fe_{16}Nb_1$ – 60 min	60	273	320	227	231	177	201	185
$Dy_2Fe_{16}Nb_1$ – 90 min	90	292	330	239	245	176	206	184
Isomer Shift (δ)		**4*f***	**Fe**	**6*g***	**12j_1**	**12j_2**	**12k_1**	**12k_2**
$Dy_2Fe_{16}Nb_1$ – 0 min	0	-0.029		-0.029	0.031	0.247	0.328	-0.232
$Dy_2Fe_{16}Nb_1$ – 30 min	30	-0.021	0.043	-0.178	0.006	0.174	0.344	-0.218
$Dy_2Fe_{16}Nb_1$ – 60 min	60	-0.051	-0.020	-0.220	0.076	0.148	0.419	-0.210
$Dy_2Fe_{16}Nb_1$ – 90 min	90	0.200	0.214	0.111	0.347	0.303	0.500	0.172
Quadruple Splitting (ΔE_Q)		**4*f***	**Fe**	**6*g***	**12j_1**	**12j_2**	**12k_1**	**12k_2**
$Dy_2Fe_{16}Nb_1$ – 0 min	0	0.158		-0.053	0.198	0.500	-0.154	-0.011
$Dy_2Fe_{16}Nb_1$ – 30 min	30	0.061	0.015	-0.145	0.268	0.370	-0.127	0.038
$Dy_2Fe_{16}Nb_1$ – 60 min	60	0.021	-0.155	-0.092	0.194	0.392	-0.021	0.005
$Dy_2Fe_{16}Nb_1$ – 90 min	90	-0.040	-0.078	-0.045	0.246	0.474	0.377	-0.500
$Dy_2Fe_{16}Nb_1$ – 90 min	90	0.118	0.100	0.142	0.169	0.051	0.093	0.118

Table 12: Mössbauer parameters of $Gd_2Fe_{16}Nb_1$ compounds.

Hyperfine Field (B_{hf})	**MT**	**Fe**	**6c**	**9d_1**	**9d_2**	**18f_1**	**18f_2**	**18h_1**	**18h_2**
$Gd_2Fe_{16}Nb_1$ – 0 min	0	-	280	243	222	234	208	231	235
$Gd_2Fe_{16}Nb_1$ – 30 min	30	329	300	265	224	241	187	203	248
$Gd_2Fe_{16}Nb_1$ – 60 min	60	330	300	265	227	243	184	204	248
$Gd_2Fe_{16}Nb_1$ – 90 min	90	332	300	270	225	244	184	213	252
Isomer Shift (δ)			**6c**	**9d_1**	**9d_2**	**18f_1**	**18f_2**	**18h_1**	**18h_2**
$Gd_2Fe_{16}Nb_1$ – 0 min	0	-	-0.355	-0.307	-0.307	-0.10	-0.10	-0.500	-0.500
$Gd_2Fe_{16}Nb_1$ – 30 min	30	0.02	-0.006	-0.014	-0.014	0.030	0.030	-0.373	-0.373
$Gd_2Fe_{16}Nb_1$ – 60 min	60	0.00	-0.024	-0.027	-0.027	0.015	0.015	-0.385	-0.385
$Dy_2Fe_{16}Nb_1$ – 90 min	90	0.01	-0.053	0.031	0.031	0.101	0.101	-0.325	-0.325
Quadruple Splitting (ΔE_Q)			**6c**	**9d_1**	**9d_2**	**18f_1**	**18f_2**	**18h_1**	**18h_2**
$Gd_2Fe_{16}Nb_1$ – 0 min	0	-	0.168	0.343	0.362	-0.04	0.08	-0.500	0.011
$Gd_2Fe_{16}Nb_1$ – 30 min	30	0.14	0.023	0.193	0.411	0.183	0.295	-0.500	-0.189
$Gd_2Fe_{16}Nb_1$ – 60 min	60	0.05	0.021	0.120	0.290	0.077	0.175	-0.500	-0.323
$Gd_2Fe_{16}Nb_1$ – 90 min	90	0.00	0.092	0.077	0.422	0.152	0.228	-0.500	-0.264

Table 13: Mössbauer parameters of $Er_2Fe_{16}Nb_1$ compounds.

Hyperfine Field (B_{hf})	**MT**	***4f***	**Fe**	***6g***	***12j₁***	***12j₂***	***12k₁***	***12k₂***
$Er_2Fe_{16}Nb_1$ – 0 min	0	241	313	266	161	197	196	32
$Er_2Fe_{16}Nb_1$ – 30 min	30	231	315	267	158	194	196	15
$Er_2Fe_{16}Nb_1$ – 60 min	60	234	314	270	148	187	181	14
$Er_2Fe_{16}Nb_1$ – 90 min	90	238	309	270	134	182	185	13
Isomer Shift (δ)		***4f***	**Fe**	***6g***	***12j₁***	***12j₂***	***12k₁***	***12k₂***
$Er_2Fe_{16}Nb_1$ – 0 min	0	-0.064	-0.474	0.021	-0.176	-0.176	-0.080	-0.08
$Er_2Fe_{16}Nb_1$ – 30 min	30	-0.124	-0.386	0.055	-0.197	-0.197	0.017	0.017
$Er_2Fe_{16}Nb_1$ – 60 min	60	-0.155	-0.500	-0.130	-0.303	-0.303	0.017	0.017
$Er_2Fe_{16}Nb_1$ – 90 min	90	-0.056	-0.427	-0.056	-0.322	-0.322	0.006	0.006
Quadruple Splitting (ΔE_Q)		***4f***	**Fe**	***6g***	***12j₁***	***12j₂***	***12k₁***	***12k₂***
$Er_2Fe_{16}Nb_1$ – 0 min	0	0.101	0.745	-0.436	0.107	-0.181	0.380	0.144
$Er_2Fe_{16}Nb_1$ – 30 min	30	0.026	0.890	-0.151	0.139	0.059	0.281	0.356
$Er_2Fe_{16}Nb_1$ – 60 min	60	-0.180	0.526	-0.253	0.281	0.104	0.166	0.322
$Er_2Fe_{16}Nb_1$ – 90 min	90	-0.163	0.579	0.085	0.161	0.247	0.304	0.284

Figure 5.6 shows Mössbauer spectra of $R_2Fe_{16}Nb_1$ (R: Dy, Gd and Er). The nature of Mössbauer spectra of all set of samples with respect to MT is same. The similar nature of Mössbauer spectra observed for mechanically milling $Zn_{30}Fe_{35}Ni_{35}$ alloys [85].

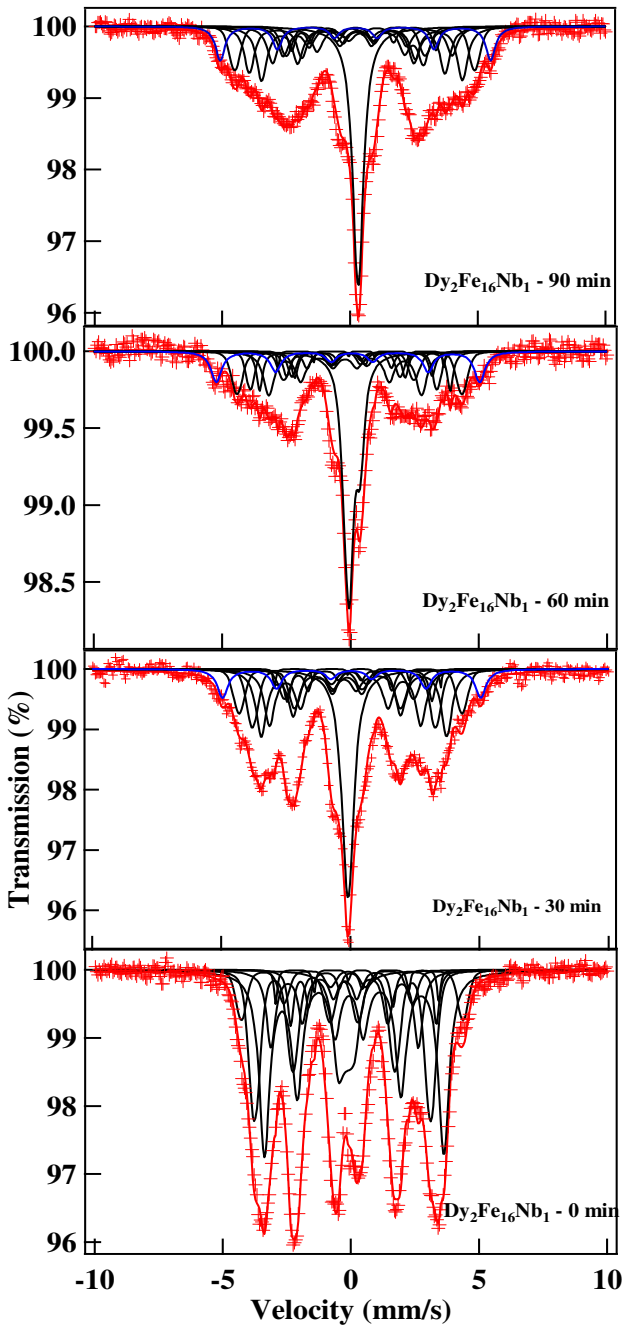

Figure 5.7a: RT Mössbauer spectra as a function of MT of $Dy_2Fe_{16}Nb_1$ alloy.

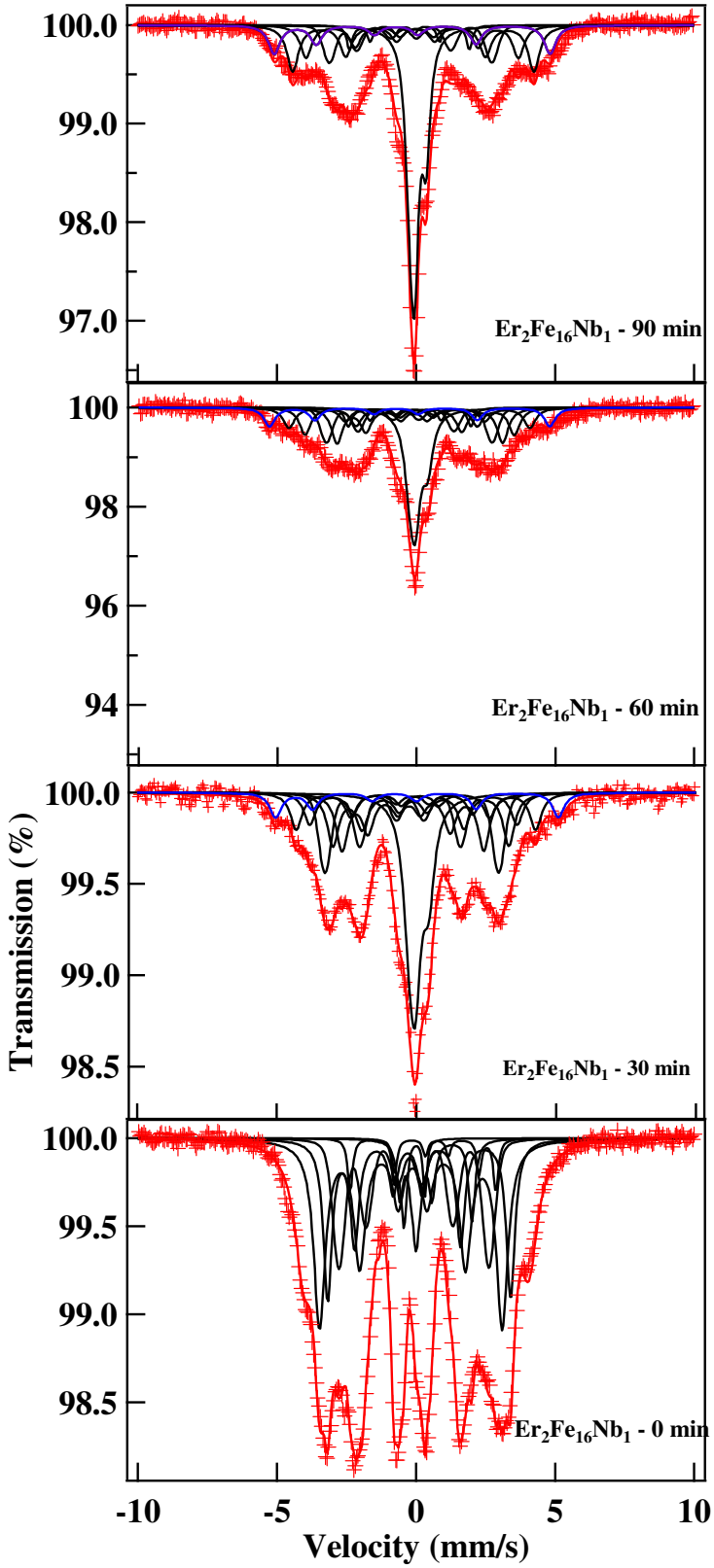

Figure 5.7b: RT Mössbauer spectra as a function of MT of $Er_2Fe_{16}Nb_1$ alloy.

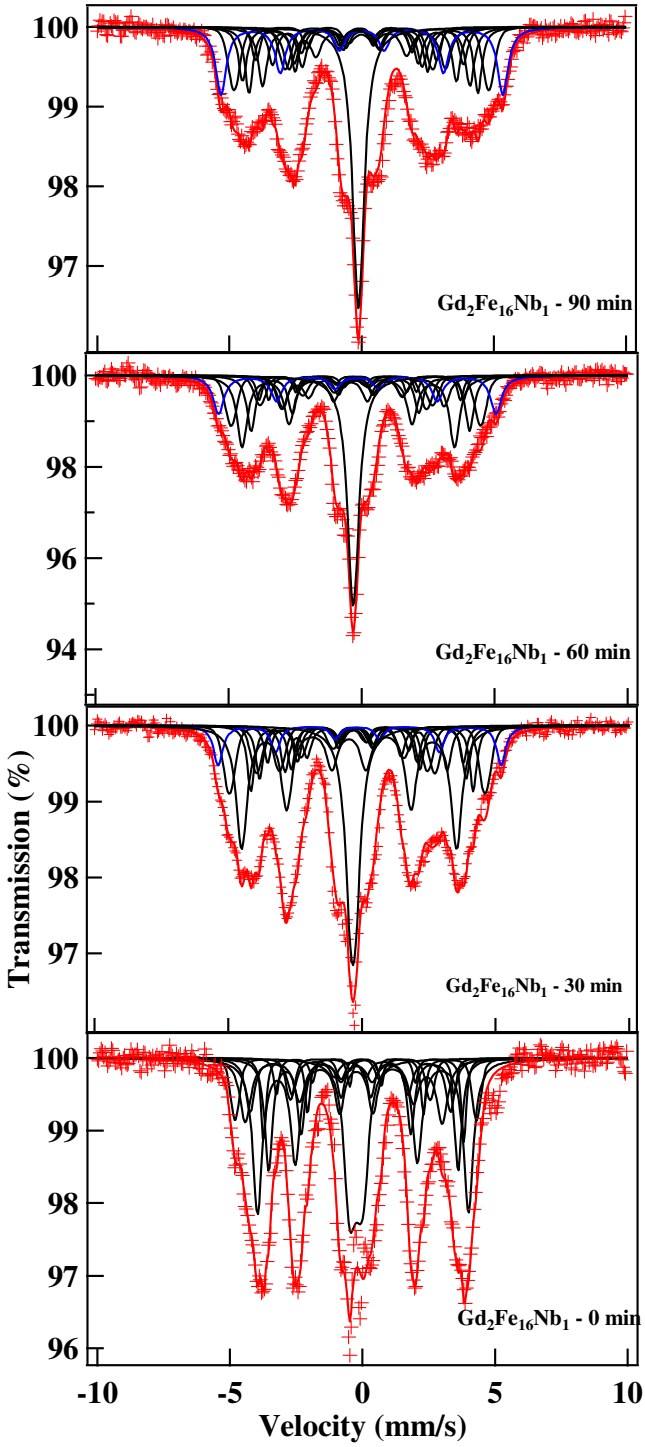

Figure 5.7c: RT Mössbauer spectra as a function of MT of $Gd_2Fe_{16}Nb_1$ alloy.

RT B_{hf} of ball milled $Dy_2Fe_{16}Nb_1$ and $Gd_2Fe_{16}Nb_1$ slightly increased as function of ball MT which consistent with the gradual increased M_s. Observing the increased T_c value of BM samples (ball milled $Dy_2Fe_{16}Nb_1$ and $Er_2Fe_{16}Nb_1$), it was expected that the trend of B_{hf} of BM $Er_2Fe_{16}Nb_1$ supposed to be as in the $Dy_2Fe_{16}Nb_1$. But B_{hf} of ball milled $Er_2Fe_{16}Nb_1$ remains almost constant. In other words, there is no clear trend of increased or decreased B_{hf} values. In our knowledge, this discrepancy is coming from the starting powder compositions. The starting powder of $Dy_2Fe_{16}Nb_1$ and $Gd_2Fe_{16}Nb_1$ had ~ 5% and 14% $NbFe_2$ phase respectively. This additional $NbFe_2$ phase in the Mössbauer plot (Fig. 5.7a and & 5.7b) is representing (in the middle of spectra) by doublet with hyperfine field $B_{hf} \approx 21$ kOe and isomer shift $\delta \approx -0.21$ mm/s. It was found match with Smith et al. [25]. This additional phase was disappeared in BM $Dy_2Fe_{16}Nb_1$ and $Gd_2Fe_{16}Nb_1$ samples. It was detected in the Mössbauer plot by singlet having zero or nearly zero B_{hf}. It confirmed that there is dissociation of $NbFe_2$ phase upon ball milling $Dy_2Fe_{16}Nb_1$ and $Gd_2Fe_{16}Nb_1$ alloys. XRD pattern also did not show diffraction peak other than Fe and 2:17 phase peak upon long hours HEBM. It means dissociation $NbFe_2$ phase was confirmed by XRD & Mössbauer studies. This observation supports Nb atoms from $NbFe_2$ phase were going into 2:17 phase which causes the lattice parameter expansion. This result is consistent with calculated parameters from XRD data. As Djega-Mriadassou et al. [72], lattice parameter expansion is linearly dependent with hyperfine field, B_{hf}. This is the reason why hyperfine field, B_{hf}, increased for BM $Dy_2Fe_{16}Nb_1$ and $Gd_2Fe_{16}Nb_1$. But this kind of B_{hf} trend was not observed in $Er_2Fe_{16}Nb_1$ sample. It may be because of the following reason. $NbFe_2$ phase had not detected from XRD in the $Er_2Fe_{16}Nb_1$ and further this phase confirmed by Mössbauer studies. In another word, the

starting powder Mössbauer spectra's of $Er_2Fe_{16}Nb_1$ is completely different (no doublet or $NbFe_2$ in the middle of spectra) than the starting powder of $Dy_2Fe_{16}Nb_1$and $Gd_2Fe_{16}Nb_1$ (have doublet in the middle). Hence, it is obvious to have no clear trend of lattice parameters as function of milling time (MT). Consequently, no clear trend even in the hyperfine field, B_{hf} of ball milled $Er_2Fe_{16}Nb_1$ (see Fig. 5.8) is observed.

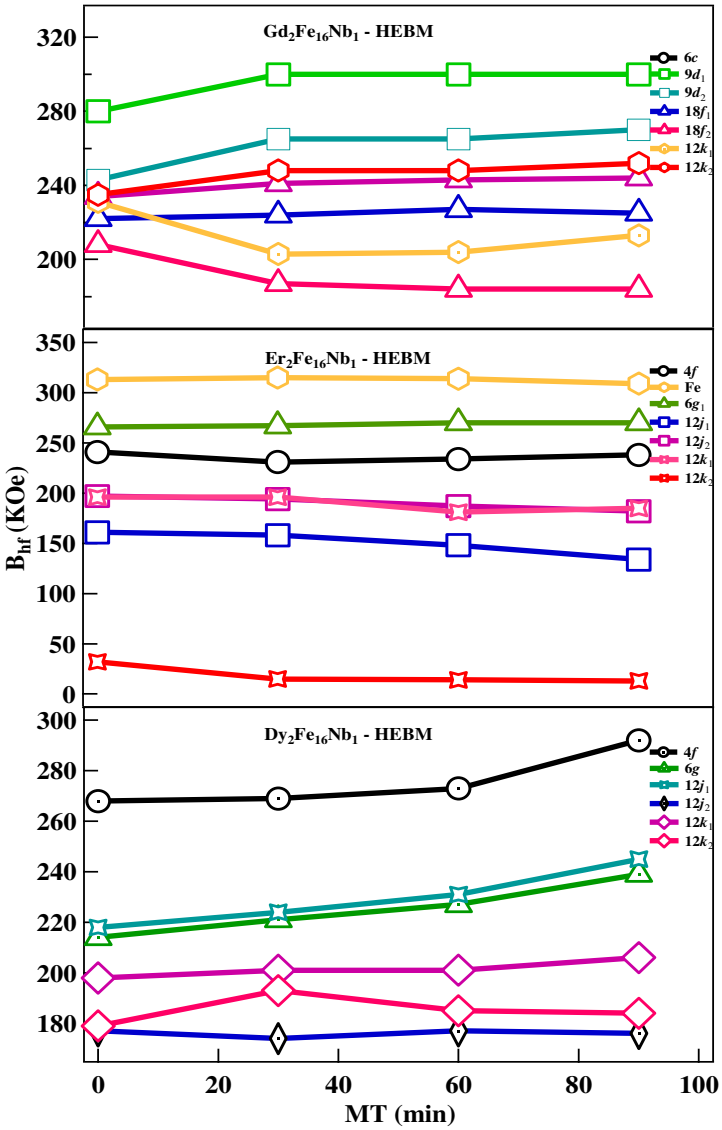

Figure 5.8: Hyperfine field of milled $R_2Fe_{16}Nb_1$ alloy as a function of BM time.

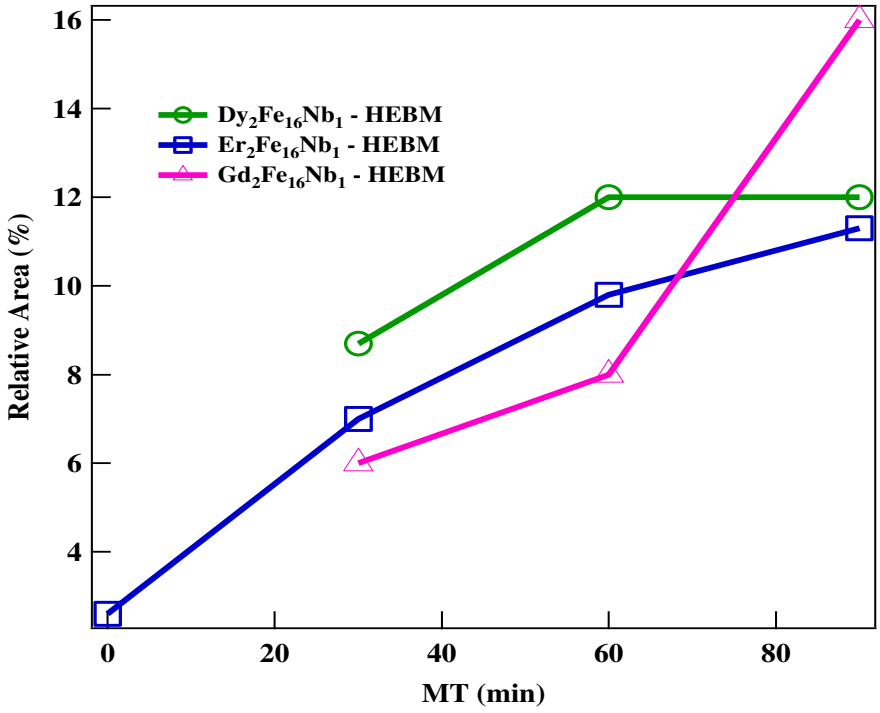

Figure 5.9: Relative area of α-Fe as function of MT for $R_2Fe_{16}Nb_1$.

Though starting powder of $Dy_2Fe_{16}Nb_1$ and $Gd_2Fe_{16}Nb_1$ did not have any α-Fe peak, the α-Fe peak was observed for each BM sample upon ball milling because of the dissociation of $NbFe_2$ phase as discussed above. This α-Fe peak was detected from XRD pattern and it was observed that the intensity of of the Fe peak was increasing as function of MT. This observation was further supported by Mössbauer studies. Introducing extra Fe sextet (other than regular six sextets for Fe) in the Mössbauer fitting only gave perfect fit. This extra Fe sextets can be identified as widest subspectra in the Mössbauer spectra. Furthermore, increased relative area intensity shown in the Fig. 5.9 agree with the XRD pattern of nanocrystalline Fe peak (see Fig. 5.1a, 5.1b, 5.1c).

The isomer shift of same site is constraint during the Mössbauer analysis. For examples, isomer shift of $12k_1$ and $12k_2$ have same value. In each set of samples, there was not observed any distinct trend of isomer shift except in $12k$ site. The isomer shift of $12k$ site (in each set of samples) is increasing it indicates that s-electron charge density of alloys are decreasing in that sites during ball milling. The increase in the isomer shift results from lattice expansion (see Table 9)

6. Conclusions

In this thesis, $R_2Fe_{17-x}Nb_x$ (R = Dy, Er and Gd; TM = Cr and Nb) and $Gd_2Fe_{16}Nb_1$ and $R_2Fe_{16}Nb_1$ compounds were successfully prepared by arc melting. In addition $R_2Fe_{16}Nb_1$ compounds were subjected to high energy ball milling. Detailed structural and magnetic properties of as prepared compounds were performed using XRD, SQUID, VSM, Mössbauer spectroscopy.

It has been observed that critical Nb concentration is x = 0.75 and x = 2.5 for pure phase of $R_2Fe_{17-x}Nb_x$ (R: Dy and Er) and $R_2Fe_{17-x}Cr_x$ compounds respectively. At higher concentration of Nb, additional phases like α-Fe, $NbFe_2$, RFe_3 (in $R_2Fe_{17-x}Nb_x$) or Dy_6Fe_{23} (in $R_2Fe_{17-x}Cr_x$) were detected from XRD and have been confirmed by Mössbauer spectral analysis. From Rietveld refinement, it was observed in $Er_2Fe_{17-x}Nb_x$ compounds that most Nb is occupying 12*k* site and least at 12*j* site of Fe. Substitution of Nb into Fe cause expansion of unit cell volume of $R_2Fe_{17-x}Nb_x$ compounds while substitution of Cr into Fe cause decrease in unit cell volume. Interestingly, highest T_c of each compound were observed for x = 1 for Nb or Cr substitution in the compounds. Non-magnetic Nb or weak magnetic Cr substitution on Fe brought monotonically decrease in saturation magnetization as function of dopants.
Hyperfine field parameter increased with Nb doping due to local electronic variation. Isomer shift shows drastic decrease with Nb doping due to increased s electron density at Fe nuclei.

For HEBM study, the ball milled compounds showed that conversion of crystalline 2:17 phase into amorphous of 2:17 with increased peak intensity of α-Fe. The $NbFe_2$ phase present in 2:17 phase disappeared during ball milling, indicating

dissociation of $NbFe_2$ into Nb and Fe. The absence of $NbFe_2$ phase in ball milled samples show slow diffusion of Nb into 2:17 phase resulted in lattice expansion and brought in magnetization and T_c enhancement. Furthermore, increase in M_r and H_c reminds of presence of exchange coupling in the ball milled compounds. Consequently, it results exchange spring behavior of 2:17 phase and α-Fe nanocrystalline phase. Variation in the coercivity was consistent with nature of HEBM process. The increased coercivity and T_c at 30 min HEBM comprised from disorder in the alloys. The highest T_c observed in $R_2Fe_{16}Nb$ (R: Dy, Er, Gd) alloy was 550°C for $Gd_2Fe_{16}Nb_1$ – 90 min-HEBM. However, better T_c improvement were observed in $R_2Fe_{16}Nb_1$ (R: Dy and Er) due to ball milling mechanism. These are the highest T_c achieved in R_2Fe_{17} series without dopants. As Mössbauer study, hyperfine field of $R_2Fe_{16}Nb_1$ (R: Dy and Gd) observed to increase as we ball mill whereas no distinct trend for $Er_2Fe_{16}Nb_1$ ball milled compounds. Either BM alloy or TM metal substituted alloy both observed with high T_c is promising candidate for alloy which can operate at high temperature environment.

References

[1] K. J. Strant, Proceedings of the IEEE, 78 (1990) 923.

[2] Jack Lifton, The Battle over the Rare earth metals, J. Energy Security, 12 Jan Issue 2010.

[3] O Gutfleisch, J. Phys. D: Appl. Phys. 33 (2000) R157.

[4] E. A. Nesbitt and J. H. Wernick, Rare-earth Intermetallics (Academic, New York) (1973).

[5] P. C. Dent, J. Appl. Phys. 111 (2012) 07A721-1.

[6] T. Mishima, Iron age. 130 (1932) 346.

[7] R. A. McCurrie, Ferromagnetic Materials, edited by E. P. Wohlfarth (North-Holland, Amsterdam), 3 (1982) 107.

[8] H. Luo, B. K. Rai, S. R. Mishra, V. V. Nguyen, J. P. Liu, J. Mang. Magn. Mater. 324 (2012) 2602.

[9] B. D. Culity and C. D. Graham, Introduction to Magnetic Mater., 2nd edition, IEEE press, Wiley publication, 2009.

[10] J. P. Liu, F. R. de Boer, P. F. de Chatel, R. Coehoorn, K. H. J. Buschow, J. Magn. Magn. Mater. 132 (1994) 159.

[11] C. W. Kimball, A. E. Dwight, R. S. Preston, S. P. Taneja, AIP Conf. Proc. 18 (1974) 1242.

[12] Buchow K. H. J. (1977) Intermetallics between rare earth and 3d elements. Rep. Prog. Phys. 40 (1997) 1179.

[13] P.C. M. Gubbins and J. J. V. Loef, J. De Physique, Colloque C6, supplement au 12, Tome 35, December 1974, C6-617.

[14] J. P. Gavigan and D. Givord, J. Magn. & Magn. Mater. 84 (1990) 288.

[15] I. A. Campbell, J. Phys. F 2 (1972) L47.

[16] IEEE Trans. Magn. **27** (1991) 3588.

[17] J. S. Jiang, J. E. Pearson, Z. Y. Liu, B. Kabius, S. Trasobares, D. J. Miller, S. D. Bader, D. R. Lee, D. Haskel, G. Srajer, J. P. Liu, Appl. Phys. Lett. 85 (2004) 5293.

[18] J. S. Benjamin. Matall. Trans., 1 (1970) 2943.

[19] C. C. Koch, O. B. Cavin, C. G. Mc Kamey and J. O. Scarbrough. Appl. Phys. Lett. 43 (1983) 1017.

[20] H. J. Fecht. Synthesis and properties of nanocrystalline metals and alloys prepared by mechanically attrition. NanoStructure Materials, 1 (1992) 125.

[21] J. Eckert, L. Schultz, E. Hellstern and K. Urban. Glass-forming range in mechanically alloyed Ni-Zr and the influence of the milling intensity. J. Appl. Phys. 64 (1988) 3224.

[22] M. L. Trudeau, R. Schulz, D. Dusault, and A. Van Neste. Phys. Rev. Lett. 64 (1990) 99.

[23] E. Gaffet. Phase transition induced by ball milling germanium. Mater. Sci. and Eng. A, p. 161 (1990).

[24] J. S. C. Jang and C. C. Koch. Amorphization and disordering of the Ni_3Al ordered intermatallic by mechanicall milling. J. Mater. Res. 5 (1990) 498.

[25] M. Oehring and R. Bormann. J. Phys. France, 51 (1990) C4-169.

[26] A. N. Patel and S. Diamond. Mater. Sci. Eng. 98 (1988) 329.

[27] G. B. Schaffer. A nanocrystalline mixture of intermetallic compounds by mechanical alloying. Scripta Metall. 27 (1992) 1.

[28] E. Gaffet and J. P. Gaspard. J. Phys. France, 51 (1990) C4-205.

[29] C. Suryanarayana / Progress in Materials Science, 46 (2001) 1.

[30] P. A. I. Smith and P. G. McCormick, Scripta Metallurgia, 26 (1992) 485.

[31] M. Faisal, C. Jiang, J. Supercond Nov Magn. 24 (2011) 779.

[32] A. E. Ermakov, E. E. Yurchikov, and V. A. Barinov. Fiz. Metal. Metalloved, 52 (1981) 1184.

[33] A. E. Ermakov, V. A. Barinov, and E. E. Yurchikov. Fiz. Metal. Metalloved, 54 (1982) 935.

[34] K. J. Strnat, Handbook on Ferromagnetic Materials, vol 4, eds. E. P. Wohlfarth and K. H. J. Buschow (North-Holland, Amsterdam, 1988) chap. 2.

[35] S. R. Mishra, Gary J. Long, O. A. Pringle, D. P. Middleton, Z. Hu , W. B. Yelon, F. Grandjean, K. H. J. Buschow, J. Appl. Phys. 79 (1996) 3145.

[36] Zhi-gang Sun, Hong-wei Zhang, Jing-yun Wang, and Bao-gen Shen, J. Appl. Phys. **86** (1999) 5152.

[37] G. J. Long, G. K. Marasinghe, S. Mishra, O. A. Pringle, Z. Hu, W. B. Yelon, D. P. Middleton, K. H. J. Buschow, and F. Grandjean, J. Appl. Phys. 76 (1994) 5383.

[38] Bao-gen Shen, Zhao-hua Cheng, Hua-yang Gong, Bing Liang, Qi-wei Yan, Wen-shan Zhan, Solid State Communications, 95 (1995) 813.

[39] Z. Zhang, Q. Yan, Solid State Communications, 94 (1995) 931.

[40] E.E. Alp, A.M. Umarji, S.K. Malik, G.K. Shenoy, M.Q. Huang, E.B. Boltich, W.E. Wallace, J. Mag. and Mag. Mater, 68 (1987) 305.

[41] Yanming Hao, Xuemin Zhang, Bowen Wang, Yizhe Yuang, and Fang Wang, J. Appl. Phys. 108 (2010) 023915.

[42] A.V. Andreev and S. Dani , Acta Physica Polinica A, 113 (2008) 239.

[43] $Sm_2Fe_{17}N_3$, J. M. D. Coey and H. Sun, J. Mag. Magn., Mater, 87 (1991) L251.

[44] $Er_2Fe_{17}N_x$, P.C. M. Gubbens, A. A. Moolenaar, G. J. Boender, A. M. van der Kraan, T. H. Jacobs, and K. H. J. Buschow, J. Mag. Magn. Mater, 7 (1991) 69.

[45] $Er_2Fe_{17}C_x$, J. P. Liu, F. R. de Boer, and P. F. de Chatel, Phys. Rev. B, 50 (1994) 3005.

[46] O. Mau, PhD Thesis, Formation and stability of Sm_2Fe_{17} carbides, McGill University, Canada, 1997.

[47] I. Betancourt and H.A. Davies, J. Magn. Magn. Mater. 261 (2003) 328.

[48] P.C. M. Gubbens, A. A. Moolenaar, G. J. Boender, A. M. van der Kraan, T. H. Jacobs, and K. H. J. Buschow, J. Mag. Magn. Mater. 7 (1991) 69.

[49] X. C. Kou, R. Grössinger, T. H. Jacobs and K. H. J. Buschow, Physica B, 168 (1991) 181.

[50] F. M. Yang, N. Tang, J. L. Wang, X. P. Zhong, R. W. Zhao, and W. G. Lin, J. Appl. Phys. 75 (1994) 4241.

[51] I. Betancourt, H.A. Davies, J. Magn. Magn. Mater. 261 (2003) 328.

[52] J. A. Chelvane, M. Palit, S. Pandian, M. M. Raja, and V. Chandrasekaran, Hyperfine Interact. 187 (2008) 87.

[53] M. Palit, J. A. Chelvane, H. Basumatary, S. Pandian, and V. Chandrasekaran, Scripta Materialia, 60 (2009) 56.

[54] Erol Girt, PhD thesis, University of McGill University, Montreal, Canada (1998).

[55] J. L. Wang, S J Campbell, J. M. Cadogan, O. Tegus and A. V. J. Edge, J. Phys.: Condens. Matter. 17 (2005) 3689-3700.

[56] S. A. Sinan, Z. M. Yousef and F. A. Alhweg, Sixth Arab Conference on the Peaceful uses of Atomic energy, Cairo, Egypt, 14-18 Dec, 2002.

[57] G. J. Long, S. R. Mishra, O. A. Pringle, Z. Hu, W. B. Yelon, F. Grandjean, D. P. Middleton, K. H. J. Buschow, J. Magn. Magn. Mater. 176 (1997) 217.

[58] W. C. Chang, S. H. Tsai, L. J. Chao, Z. B. Hu, H. Luo, W. B. Yelon, J. Magn. & Magn. Mater. 172 (1997) 277.

[59] E. Belorizky, M. E. Fremy, J. P. Givord and H. S. Li, J. Appl. Phys. 61 (1987) 3971.

[60] Gschneidner K. A., Eyring L. Handbook on the Physics and Chemistry of Rare Earths, 24 (1997) 384.

[61] H. Y. Ming, Y. D. Wei, Z. P. Lin et. al. Acta. Phys. Sincia, 6 (1997) 440.

[62] Y. M. Hao, P. L. Zhang, X. D. Shun, Q. W. Yan, Ridwan, Mujamilah, Gunawan and Marsonkohadi,J. Phys. : Condens. Matter. 8 (1996) 1321.

[63] P. A. M. Catellanos, J. C. S. Jarque, and J. A. Rivera, Physica B, 362 (2005) 95.

[64] H. Y. Ming, Y. D. Wei, Z. P. Lin et. al. Acta. Phys. Sincia, 6 (1997) 440.

[65] P. C. M. Gubbens, PhD thesis¸University of Leiden, (1977).

[66] L. Liao, PhD thesis, Cobalt Site in Iron Rare-earth based compounds, 1992, McGill University Montréal, Canada.

[67] P.C. M. Gubbens, K. H. J. Buschow, J. Appl. Phys. 44 (1973) 3739.

[68] O. Isnard, D. Hautot, G. J. Long, F. Grandjean, J. Appl. Phys. 88 (2000) 2750.

[69] K. H. J. Buschow, J. S. V. Wieringen, Phys. Status Solidi 42 (1970) 231.

[70] L. M. Levinson, E. Rosenberg, A. Shaulov, K. Strnat, J. Appl. Phys. 41 (1970) 910.

[71] L. Bessais, C. Djéga-Mariadassou, H. Lassri, and N. Mliki, J. Appl. Phys. 106 (2009) 103904.

[72] C. Djega-Mariadassou, L. Bessais, Journal of Magnetism and Magnetic Materials 210 (2000) 81.

[73] A. Grabias, D. Oleszak and M. Pekala, Rev. Adv. Mater. Sci. 18 (2008) 379.

[74] A. W. Smith and R. D. Rawlings, Phys. Stat. Sol. (a) 22 (1974) 491.

[75] A. M. V. D. Kraan, P.C. M. Gubbens, and K. H. J. Buschow, Phys. Stat. sol. (a) 31 (1975) 495.

[76] J. J. Bara, A. T. Pedziwiatr, and W. Zarek, J. Magn. & Magn. Mater. 27 (1982) 168.

[77] I. Nehdi, L. Bessais, C. Djega-Mariadassou, M. Abdellaoui, H. Zarrouk, J. Alloys and Comp. 351 (2003) 24.

[78] H. Z. Luo, Y. X. Li, L. Jia, F. B. Meng, J. P. Qu, J. Shen, N. X. Chen, G. H. Wu, F. M. Yang, J. Alloys and Comp. 397 (2005) 31.

[79] Zhao-hua Cheng, Bao-gen Shen, Qi-wei Yan, and Hui-qun Guo, Phys. Rev. B 57 (1998) 14299.

[80] Er. Girt, Z. Altounian, J. Appl. Phys. 8 (1997) 5118.

[81] Z. Sun, H. Zhang, S. Zhang, J. Wang, B. Shen, J. Phys. D: Appl. Phys. 33, 485 (2000).

[82] Y. H. Wang, Basics of X-ray diffraction, Atomic Energy publishing House, Beijing, 1993.

[83] X. Rui , J.E. Shield, Z. Sun, L. Yue, Y. Xu, D.J. Sellmyer, Z. Liu, and D.J. Miller, J. Magn.Magn. Mater. 305 (2006) 76.

[84] G. F. Zhou, H. Bakker, Scripta Mater. 34 (1996) 29.

[85] A. Grabias, D. Oleszak and M. Pekala, Rev. Adv. Mater. Sci. 18 (2008) 379.

List of Publications

● Physical and Magnetic properties of highly aluminum doped strontium ferrite nanoparticles prepared by auto-combustion route, H. Lou, B. K Rai, S. R. Mishra, V. Vuong, J. P. Liu, J. Magn. & Magn. Mater. 23 (2012) 2602.

● Reusable hybride $CoFe_2O_4$-ZnO hollow nanospheres as photocatalysts, A. Wilson, S. R. Mishra, B. K. Rai, R. Gupta and K. Ghosh, MRS F 11-1406-z05-68.

● Facile Mechanochemical synthesis and Magnetic properties of pervoskite $YCr_xFe_{1-x}O_3$ ($0 \leq x \leq 1$), V. Malagareddy, B. K. Rai, S. K. Karna, S. R. Mishra, R. Rong, J. P. Liu, E.S. Gunapala MRS F 2011- 1397-p13-01.

• Synthesis and Properties of Near Infrared-Absorbing Magnetic-Plasmonic Nanopins, S. Bhana, B. K. Rai, S. R. Mishra, Y. Wang and X. Huang, Nanoscale, 2012, Advaced Article.

● Engineering Silver nanoparticles in PVP-PEG blend, T. Dahal, Z. Glenn, B. K. Rai, S. R. Mishra, J. Nanoscience and Nanotech. in Press (2012).

● Magnetic Properties of Bulk SmCo5/FeNi/FeCo composite magnet prepared by Electroless Coating Technique, M. Lamichhane, B. K. Rai, S. R. Mishra¸ V. Vuong, J. P. Liu., O. J. Comp. Mater. in Press (2012).

● Magnetically hard-soft composites $SmCo_5$-FeNi prepared via high energy ball milling, B. K. Rai, S. R. Mishra, submitted on J. Alloys & Comp. (2012).

● Synthesis and characterization of High Coercivity Rare-Earth ion Doped $Sr_{0.9}RE_{0.1}$ $Al_2Fe_{10}O_{19}$), B. K. Rai, S. R. Mishra, N. V. Vuong. J.P. Liu, submitted on J. Alloys & Comp. (2012).

• Effect of high energy ball milling on magnetic properties of $Dy_2Fe_{16}Nb$ alloy, B. K. Rai, S. R. Mishra, to be submitted on J. Magn. & Magn. Mater. (2012).

• Structural, magnetic and Mossbauer studies of $Er_2Fe_{17-x}Nb_x$ alloys, B. K. Rai, S. R. Mishra, to be submitted on J. Magn. & Magn. Mater. (2012).